Multi-scale Modelling of Gastric Electrophysiology

by Alberto Corrias

Supervised by Dr Martin L Buist

Co-supervised by A/P Soong Tuck Wah

A thesis submitted in partial fulfilment of the requirements for the degree of Doctor of Philosophy in Bioengineering within the Graduate Programme in Bioengineering, National University of Singapore.

July, 2008

Abstract

We have developed a multi-scale computational modelling framework for the study of gastric electrophysiology in health and disease. Electrical excitability is a fundamental ability that cells within the gastric musculature have developed in order to perform their basic physiological functions of contracting and relaxing in a coordinated pattern. Intrinsic electrical and mechanical activity in the gastric musculature is thought to arise from the interplay among smooth muscle (SM) cells, interstitial cells of Cajal (ICC) and the enteric nervous system (ENS). ICC are responsible for the omnipresent electrical activity intrinsic to the stomach musculature (slow waves) whereas the ENS constitutes an additional extrinsic level of control. Abnormalities in slow wave parameters such as frequency and amplitude are of clinical interest as they are thought to underlie a variety of gastric motility disorders and conditions, some of which are still of unknown etiology.

First, we have developed two novel biophysically based models of ICC and SM cell electrophysiology where realistic descriptions of ion channel biophysics combine to reproduce the experimentally observed slow wave activity. Second, we have integrated the two cell models into a three dimensional human stomach geometry where the spatially varying characteristics of the tissue were incorporated into the model for the study of propagation of the slow waves. Third, we simulated the electrical field generated by the stomach within a human torso with the aim of simulating the electrogastrogram (EGG). Finally, we

performed a preliminary exploration of the capabilities of the modelling framework by investigating the effects of a genetic mutation of the gene SCN5A, encoding a gastrointestinal (GI) Na^+ channel, on the electrophysiology of the stomach.

By integrating models from ion channels to cells to tissues, organs and through to the whole torso we bring together a vast quantity of experimental data and are able to package it succinctly. This allows us to manipulate and explore the system in ways that would be difficult, if not impossible, experimentally.

Acknowledgements

I would like to express my gratitude to my supervisor, Dr Martin Buist, for having been an extremely competent, patient and readily available guide throughout this project. I would also like to mention the innumerable situations where, even if not strictly required by his academic duties, Dr Buist shared with me invaluable tips as well as words of encouragement that made my research experience enriching and fulfilling.

My deepest gratitude also goes to Dr David Nickerson for the incredible amount of knowledge that he has been willing to patiently share with me. The day he joined the Computational Bioengineering Laboratory proved to be a crucial cornerstone for this project and my career in general.

I would like to thank my co-supervisor, A/P Soong Tuck Wah, and the entire staff of the Ion Channel & Transporter Laboratory for their patience and support. I would also like to express my gratitude to the Graduate Programme in Bioengineering and the National University of Singapore for the generous funding.

Last but not least, I would like to acknowledge the contribution of my classmates and labmates: Chee Tiong (and his family), David, Vinayak, Darren, Robin, Lei Yang, Anju, Ashray, Viveka, William, Yong Cheng, Wen Wan and May Ee, thanks for your help and friendship.

To my parents Silvana and Michele

Ai miei genitori Silvana e Michele

Contents

List of Figures

List of Tables

Chapter 1

Introduction

The stomach is a hollow muscular organ located below the oesophagus in the gastrointestinal (GI) tract. It serves as a short-term storage reservoir where the initial mechanical and chemical breakdown of ingested food occurs. According to the Marvin M. Schuster Motility Center at Johns Hopkins, GI motility disorders affect 35 million people in the USA alone - nearly three times as many as coronary heart disease, and, next to the common cold, are the second most common cause of absenteeism from the workplace (Marvin Schuster Center, 2008). The National Institute of Diabetes and Digestive and Kidney Diseases (NIDDK) reported a staggering yearly economic burden of US$107 billion caused by digestive disorders in the USA, more than all circulatory problems combined (NIDDK, 2006). These figures appear to be in stark contrast with our relatively poor knowledge of the physiological mechanisms underlying GI function in health and disease and the consequent scarcity of diagnostic tools and treatment options. For example, the basic pacemaker function in the GI tract was conclusively attributed to the Interstitial Cells of Cajal (ICC) only

in the second half of the last decade (Sanders, 1996), whereas the function of the sino-atrial node as a pacemaking region in the heart has been known for several decades (Birchfield *et al.*, 1957). As a consequence, our knowledge of the pathophysiology of the heart and the GI tract are dramatically different and in parallel, computational modelling of the GI tract, the focus of this research, lags behind its cardiac counterpart.

Over the past few decades numerous experiments have uncovered the high level of biological complexity that underlies the pathophysiology of many maladies that affect the GI tract. Mathematical models can succinctly describe the results from large numbers of experiments and thus provide an invaluable tool to aid in developing our understanding of physiological and pathophysiological processes. The modelling framework developed in this thesis, summarised in Section 1.1, is primarily aimed at providing a realistic mathematical description of gastric electrophysiology at different scales of investigation.

1.1 Thesis Overview

The underlying hypothesis of this thesis is that mathematical descriptions of the cellular and sub-cellular events underlying stomach electrophysiology can be combined to reproduce gastric electrical activity in health and disease with a view to enhancing fundamental understanding and improving diagnostic efficacy. In view of this, the thesis focuses on the development of a realistic computational model of gastric electrophysiology and aims to perform a preliminary exploration of its capabilities as a tool for investigating clinical conditions.

After providing a general overview of the relevant aspects of gastric anatomy and physiology, the mathematical techniques used to model electrophysiological systems are discussed in this chapter. A critical literature review of previous modelling work in this area is presented in Chapter 2. Chapters 3 and

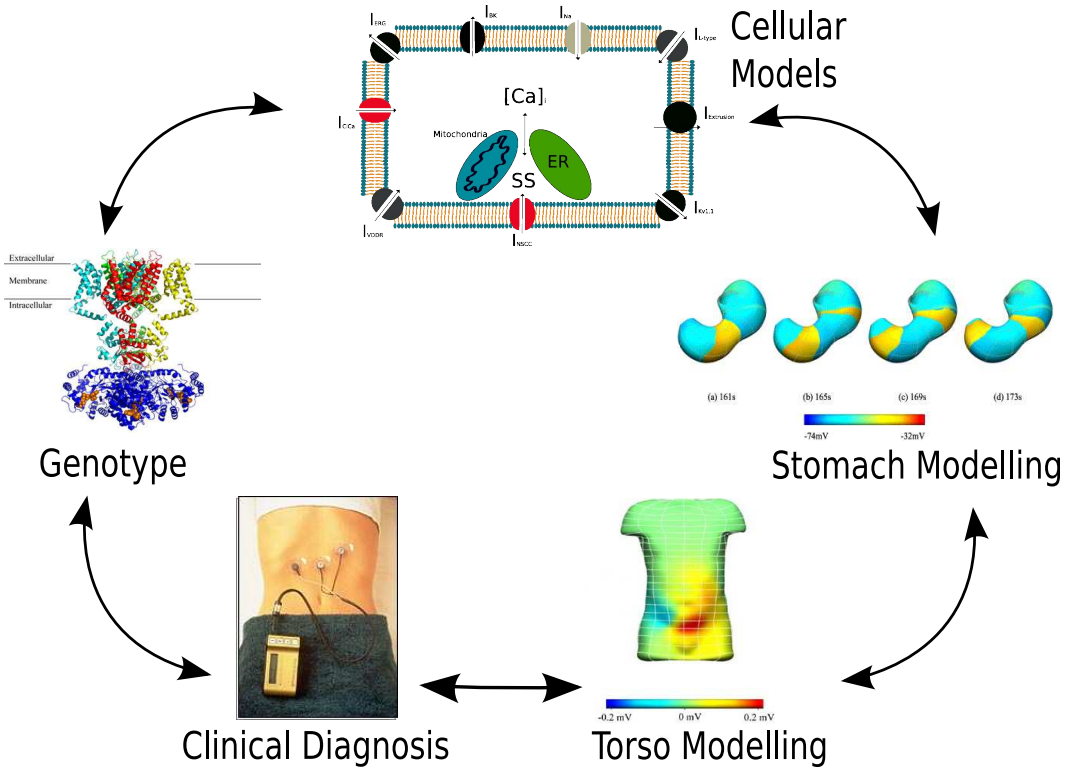

Figure 1.1: Links from genotype to phenotype in gastric physiology. Here the different levels of modelling developed in this thesis are shown, from the ion channel level to the human torso.

4 present two novel cellular models of a gastric smooth muscle (SM) cell and of an ICC that have been developed. These models are based on published experimental data concerning the biophysics of the ion channels as studied in isolation during patch clamp experiments. We have validated both cellular models against experimental recordings under normal and pharmacologically

altered conditions. Chapters 5 and 6 contain the results of multidimensional simulations where the cellular models of Chapters 3 and 4 are included in a continuum modelling framework that is used to describe the electrophysiology of gastric tissue. The incorporation of cellular details into large scale tissue descriptions allowed novel insights into gastric pathophysiology to be obtained (Sections 5.6 and 6.6). A preliminary exploration of the capabilities of the modelling framework developed in this thesis will be discussed in Chapter 8 where the effects of a genetic mutation affecting the SCN5A-encoded Na^+ channel will be analysed. Figure 1.1 shows a schematic view of the conceptual link between genotype and clinical phenotype that this thesis aims at addressing.

1.2 Anatomy of the Stomach

The total length of an adult stomach varies from 15 to 25 cm. Its volume depends on the amount of food it contains and can vary from 50 ml to 4 L. The convex surface on the lateral side of the organ is referred to as greater curvature, while the convex surface on the medial side is known as lesser curvature (Marieb, 2004).

Anatomically, the stomach is divided into four parts: the cardiac region (or cardia), fundus, corpus and antrum (Figure 1.2). The cardiac region takes its name from its close proximity to the heart and is located around the oesophageal sphincter. The fundus is a dome-shaped part located just below the diaphragm. The corpus (or body) constitutes the largest part of the stomach and connects the fundus to the the funnel-shaped antrum. Because of its large

dimensions, the corpus is often subdivided into orad corpus (the proximal region), mid-corpus and caudad corpus (the distal region). The antrum is then connected to the small intestine through the pyloric sphincter.

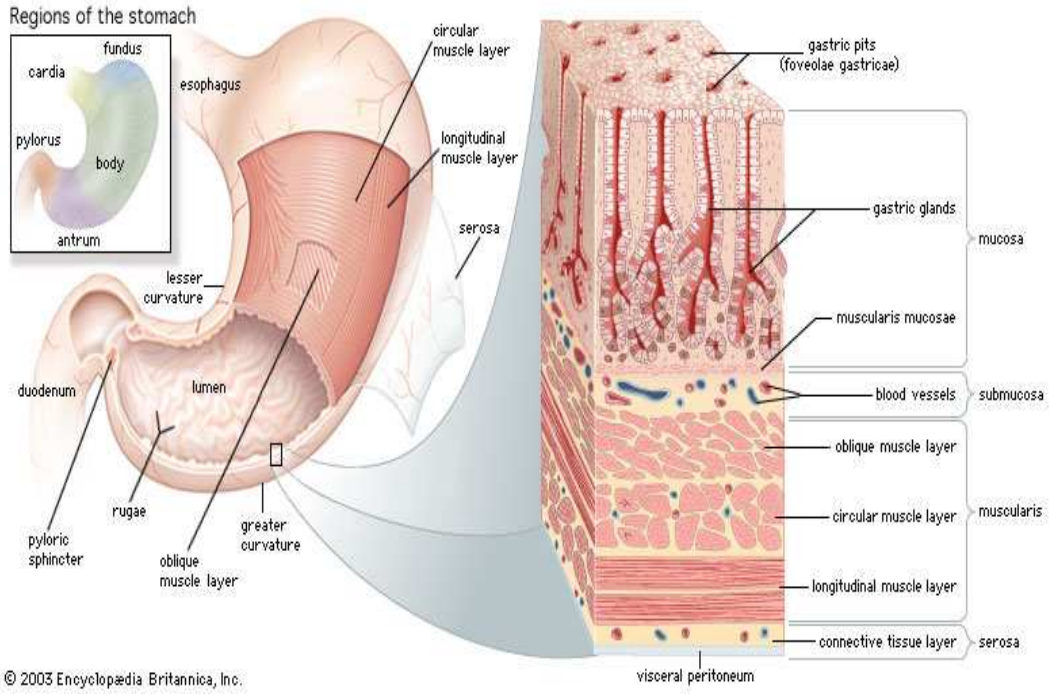

Figure 1.2: A schematic diagram of the anatomy of the stomach and the microstructure of a section of the stomach wall (adapted from Encyclopedia Britannica (2003)).

The stomach wall is divided into four layers named the mucosa, submucosa, *muscularis externa* and serosa (Figure 1.2). The mucosa is the innermost layer and its surface is coated with an epithelial layer composed entirely of goblet cells. The smoothness of this surface is interrupted by the presence of many gastric pits, which are connected with the underlying gastric glands, where the gastric acids necessary for the initiation of the digestive process are synthesised by at least four types of secretory cells: mucous neck cells (found in

the upper region of the gland), parietal cells (which release hydrochloric acid), chief cells (which secrete pepsinogen) and enteroendocrine cells (which secrete a variety of hormones including serotonin, somatostatin and gastrin). The richly vascularised submucosa serves the purpose of delivering nutrients to, and clearing wastes from, the surrounding layers. The *muscularis externa* harbours several smooth muscle layers and is responsible for gastric motility. Section 1.3 is dedicated to providing details of the microstructure of the *muscularis externa*, one of the focuses of this thesis. The outermost layer, the serosa, is a vascularised connective tissue that wraps the entire stomach (Marieb, 2004).

1.3 Microstructure of *Muscularis Externa* and Gastric Motility

The term gastric motility refers to the organised activity of the gastric musculature in the *muscularis externa* that accomplishes the physiological functions of mixing, breaking down and the orderly emptying of the ingested food from the stomach into the small intestine. Abnormalities in gastric motility are the cause of several known clinical conditions such as gastroparesis and functional dyspepsia (Streutker *et al.*, 2007) and are associated with common clinical symptoms such as delayed gastric emptying, early satiety, nausea and vomiting.

Electrical excitability is a fundamental ability that cells within the gastric musculature have developed in order to perform their basic physiological functions of contracting and relaxing in a synchronised pattern. Intrinsic electrical

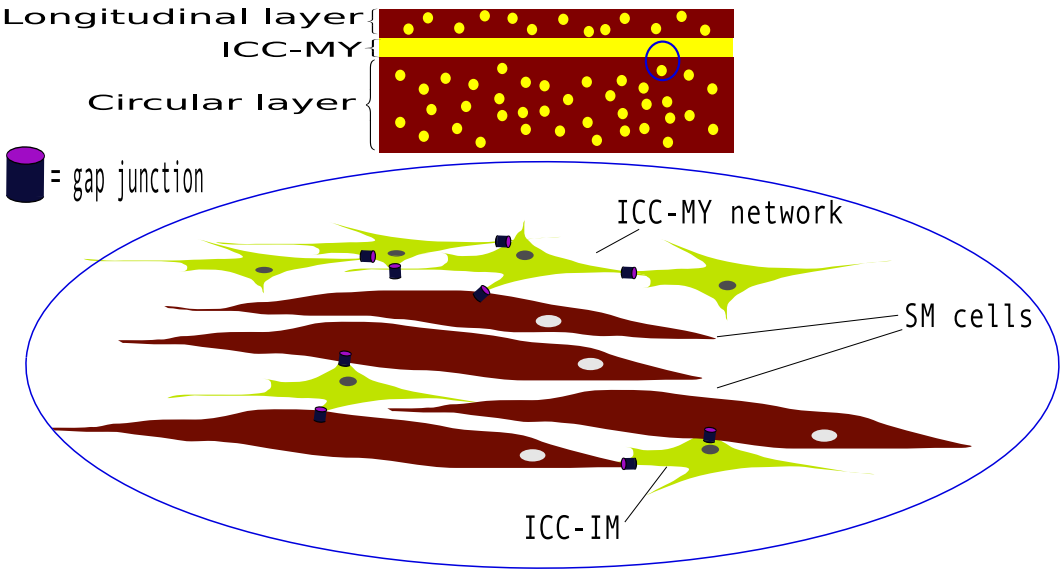

Figure 1.3: A schematic diagram of the microstructure of *muscularis externa*: the ICC-MY layer is located in between the circular muscle layer and the longitudinal muscle layer. ICC-IM are interspersed among the SM cells. Gap junctions provide electrical connections between ICC-MY and between ICC-IM and SM cells.

and mechanical activity in the gastric musculature is thought to arise from the interplay between SM cells, ICC and the enteric nervous system. Within the *muscularis externa*, SM cells are organised in layers of different thicknesses, each containing muscle fibres with different orientations. The circular layer, whose fibres are oriented circumferentially, is the thickest and is considered the major player in the development of the peristaltic waves that push the ingested food in the anal direction along the GI tract. The longitudinal layer has fibres oriented in the longitudinal direction and is considered responsible for variations in length of the stomach, useful for churning the ingested food and gastric acids. Finally, the oblique layer is sparsely present in the gastric wall and is believed to have a minor role in gastric motility (Marieb, 2004).

ICC are cells of mesenchymal origin and were first described by Santiago Ramon y Cajal in 1893 (Cajal, 1893), although their role as a pacemaker cell was elucidated much later (Langton *et al.*, 1989a). ICC are now believed to be responsible for the omnipresent electrical activity intrinsic to the stomach musculature (slow waves). Gastric electrical activity is spread from one ICC to another and from ICC to SM cells via gap junctions (Daniel, 2004). The existence of direct connections between SM cells in the stomach has been object of controversy (Seki *et al.*, 1998) and no specific functional role for such connection has been proposed. SM cells within the stomach wall are capable of generating a contractile response to the electrical activity generated by the ICC. Nevertheless, during normal slow wave activity, little, if any, contractile response is recorded in the SM layers. Only when an additional external stimulus reaches the musculature, superimposed on the slow waves, is a contractile response triggered. The nature of the external stimulus might be either electrochemical (from ENS, transduced by ligand gated ion channels), mechanical (transduced by mechanosensitive ion channels) or a combination of the two.

ICC have been classified primarily according to their anatomical location (Sanders *et al.*, 2006a). In between the circular and longitudinal muscle layers, a dense network of ICC (ICC-MY) lie in the plane of the myenteric plexus. ICC-MY are believed to actively generate and propagate slow waves throughout the stomach musculature. ICC interspersed within the circular muscle layer are referred to as ICC-IM and are believed to mediate regulatory signals coming from the ENS as well as contributing to the propagation of slow waves (Ward & Sanders, 2006). Finally, ICC lying in the septa between SM bun-

dles are referred to as ICC-SEP and have also been implicated in conducting electrical stimuli to the surrounding muscle layers (Lee *et al.*, 2007b).

1.4 Electrophysiological Models

An introductory overview of the mathematics used to model electrically active cells and tissues is given in this section. Methods for modelling single cell electrophysiology will be followed by an overview of the models at the tissue and organ levels.

1.4.1 Single Cell Electrophysiology Models

The Hodgkin and Huxley model

All current models of cellular electrophysiology share their roots in the seminal work that Hodgkin and Huxley published in 1952 (Hodgkin & Huxley, 1952). The Nobel prize winners were the first to assimilate the cell membrane with an equivalent circuit made up of a capacitor connected in parallel with several variable resistances representing the transmembrane ionic currents that were believed to occur in the axon of a giant squid neuron. Figure 1.4 shows a schematic view of their equivalent circuit where three ionic currents are modelled, one Na^+ current, one K^+ current and one leak current. In addition, an externally applied current can be added in order to take into account a stimulus coming from a neighbouring cell or another external source. The governing

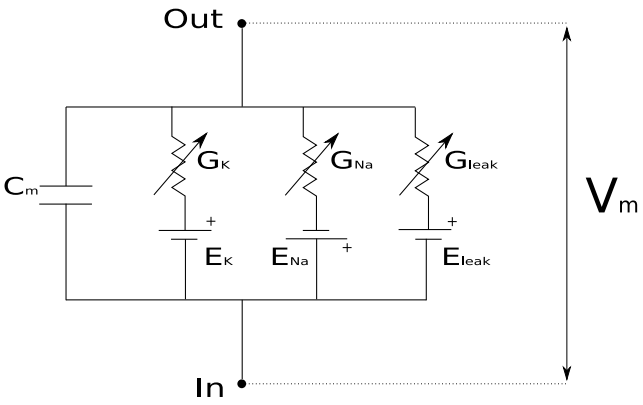

Figure 1.4: A schematic diagram of the Hodgkin and Huxley model.

equation of such an electrical system is given by

$$C_m \frac{dV_m}{dt} = -I_{ion} + I_{stim} \tag{1.1}$$

where V_m (in mV) represents the transmembrane potential, C_m is the total cell capacitance, I_{ion} represents the sum of the ionic fluxes through the cell membrane and I_{stim} represents any externally applied stimulus. Each ionic current is modelled according to the biophysical properties of the ion channel through which it flows. For a given ion X, the maximal ionic current is given by

$$I_{X_{max}} = G_X(V_m - E_X) \tag{1.2}$$

where G_X is the maximal conductance that primarily depends on two aspects; firstly, the physical properties of the transmembrane pore formed by the transmembrane domain of the ion channel and its permeability to ion X, and secondly, the density of ion channels of type X expressed in the cell membrane.

E_x is the Nernst potential for ion X and is given by

$$E_X = \frac{RT}{z_X F} log \frac{[X]_e}{[X]_i} \tag{1.3}$$

where R is the universal gas constant, T is absolute temperature, z_X is the valence of ion X, F is Faraday's constant and $[X]_e$ and $[X]_i$ are the extra- and intra-cellular concentrations of ion X respectively. The (V_m-E_X) term represents the electrochemical driving force that governs the movement of ion X. The presence of voltage dependent behaviour in many ion channels is taken into account with specific dimensionless gating variables. When all the gates in the cell are open, the gating variable equals 1.0, whereas it equals 0.0 when all the gates are closed. The kinetics of a given gate in an ion channel can be represented by a gating variable, m, whose value is determined by

$$\frac{dm}{dt} = \frac{m_\infty - m}{\tau_m} \tag{1.4}$$

where m_∞ is the steady state value and τ_m is the time constant. Both m_∞ and τ_m usually depend on the transmembrane potential, V_m. Each ionic current can then be described by

$$I_X = I_{X_{max}} \Pi(m_i) \tag{1.5}$$

where $\Pi(m_i)$ is the product of all the gating variables. The total ionic current is therefore given by the product of two components, one variable channel conductance and an electrochemical driving force. In order to have a non-zero current, two conditions must therefore be fulfilled: there must be a non-zero conductivity and a non-zero driving force. In the Hodgkin and Huxley model,

Equation 1.1 becomes

$$C_m \frac{dV_m}{dt} = -(I_{Na} + I_K + I_{leak}) + I_{stim} \tag{1.6}$$

where the ionic currents are modelled according to Equations 1.2 and 1.5 as

$$I_{Na} = G_{Na} m^3 h (V_m - E_{Na}) \tag{1.7}$$

$$I_K = G_K n^4 (V_m - E_K) \tag{1.8}$$

$$I_{leak} = G_{leak} (V_m - E_{leak}) \tag{1.9}$$

where m, h and n are gating variables, G_{Na}, G_K and G_{leak} are the maximal conductances for the Na^+, K^+ and leak currents respectively and E_{Na}, E_K are the Nernst potentials for the Na^+ and K^+ ions. E_{leak} was experimentally determined as the Nernst potential of all the non-Na^+ or K^+ currents. The results of the numerical integration of Equation 1.6 by means of the forward Euler method are shown in Figure 1.5, which displays the behaviour of the action potential as a function of time in a giant squid neuron.

Cellular models of cardiac electrophysiology

The Hodgkin and Huxley approach has been widely applied to modelling several electrically excitable tissues. Cardiac electrophysiology has been an area of particular interest. Over the past few decades, several models of increasing complexity have appeared in literature in this field. Thanks to these efforts, genetic disorders resulting in ion channelopathies have been directly linked

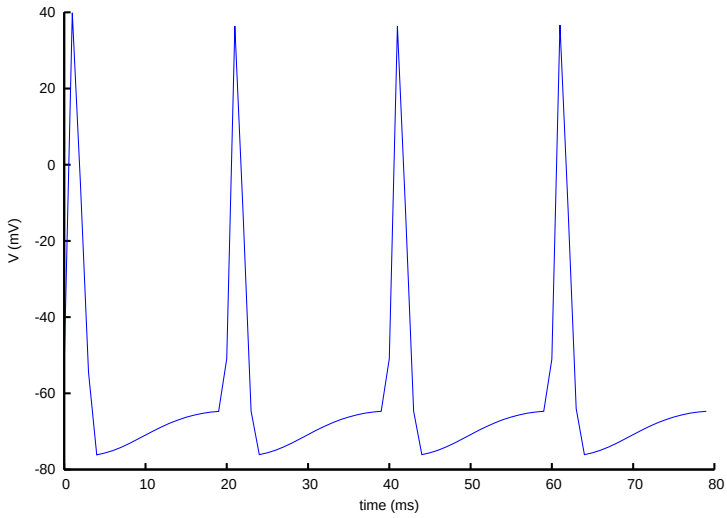

Figure 1.5: A train of action potentials generated from the Hodgkin & Huxley (1952) model.

to cardiac conditions and consequent abnormalities in the electrocardiogram (Splawski *et al.*, 2004). Moreover, our understanding of such multifactorial conditions as cardiac arrhythmia has increased dramatically thanks to these investigations (Clancy & Rudy, 1999).

A typical modern cardiac single-cell model reflects our increased knowledge of ion channel physiology. More than a dozen ion channel types (compared to the three types described by Hodgkin and Huxley) and many of the intracellular mechanisms believed to be responsible for regulating membrane ion channels are normally included. An example of this is shown in Figure 1.6 where a schematic diagram of the ten Tusscher model of a human ventricular myocyte is shown together with the predicted action potentials obtained by integrating this model (ten Tusscher *et al.*, 2004).

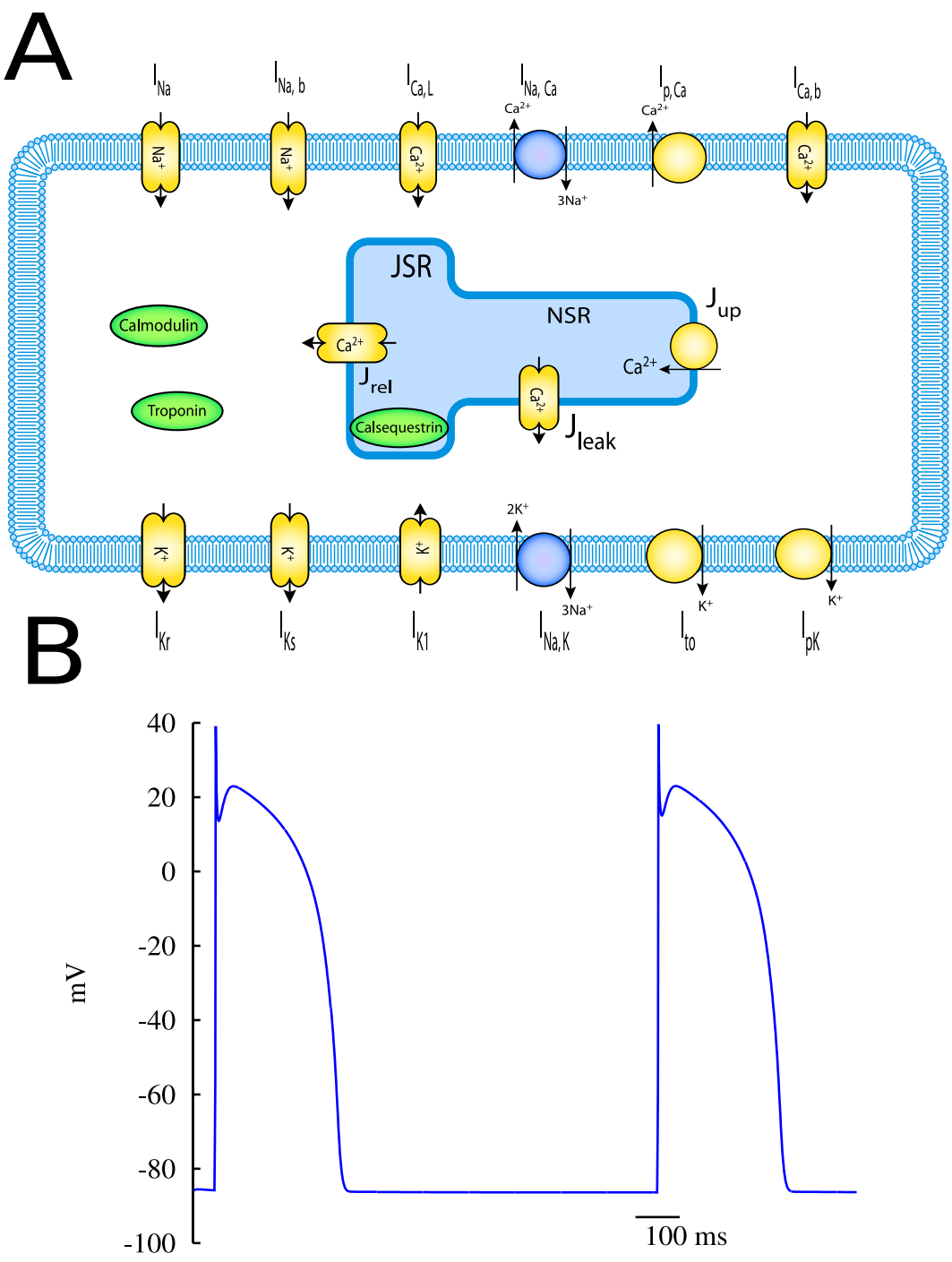

Figure 1.6: A. A schematic diagram of the ten Tusscher model (diagram adapted from the CellML repository (2008)). B. Predicted action potentials of human ventricular myocytes.

1.4.2 One-Dimensional Cable Models

One-dimensional simulations have previously been used to model the electrophysiology of long cells such as neurons (Hodgkin & Huxley, 1952). The development of the full theoretical framework is beyond the scope of this thesis and can readily be found elsewhere (Malmivuo & Plonsey, 1994).

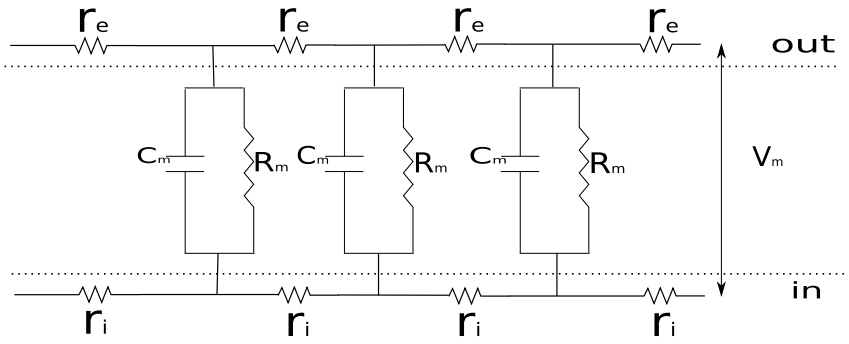

Figure 1.7: Equivalent circuit of a passive cable. Each membrane element, here simplified by a parallel connection between a capacitor and a resistance, is separated by an extracellular resistivity r_e and by an intracellular resistivity r_i.

In brief, the description is based on the equivalent circuit shown in Figure 1.7 where the simplified case of a passive cable is illustrated. Many equivalent circuits of the cell membrane are connected in parallel to each other. Intercalated between each membrane element are intracellular (r_i) and extracellular (r_e) resistivities. In a cable of uniform cross section A and length l, resistivity can be calculated from the bulk resistance (R) measured between the extremities of the cable by

$$r = R * \frac{A}{l} \tag{1.10}$$

Conductivity is then simply given by

$$\sigma = \frac{1}{r} \tag{1.11}$$

The current flowing through each membrane circuit is given by

$$I_m = A_m(C_m \frac{dV_m}{dt} + \frac{V_m}{R_m}) \tag{1.12}$$

where A_m is the surface-to-volume ratio of the cell. The same quantity can also be expressed by considering current flowing along the cable and combining the Ohm's and Kirchhoff's current laws

$$I_m = \frac{1}{r_e + r_i} \frac{d^2V_m}{dx^2} \tag{1.13}$$

Here r_e and r_i are the extra- and intra-cellular resistivities respectively. Combining Equations 1.12 and 1.13 yields

$$\frac{1}{r_e + r_i} \frac{d^2V_m}{dx^2} = A_m(C_m \frac{dV_m}{dt} + \frac{V_m}{R_m}) \tag{1.14}$$

An integration of Equation 1.14 allows the calculation of the transmembrane potential at every point of the passive cable as a function of time.

Equation 1.14 can be adapted to the case of an active cable, where each cellular element actively contributes to the propagation of the electrical signal. In such circumstances, the current flowing through each membrane circuit takes the form

$$I_m = A_m(C_m \frac{dV_m}{dt} + I_{ion}) \tag{1.15}$$

where I_{ion} takes into account the cellular ionic currents of each component in the cable. Combining Equation 1.15 and Equation 1.13 then gives

$$\frac{1}{r_e + r_i}\frac{d^2V_m}{dx^2} = A_m(C_m\frac{dV_m}{dt} + I_{ion}) \tag{1.16}$$

which describes the propagation of the membrane potential along a cable of electrically active cells. Equation 1.16 will be used in this thesis to model the active propagation of electrical signals within a 1-D representation of the gastric musculature.

1.4.3 Three Dimensional Tissue Models

Biological tissues consist of a large number of discrete cellular components that interact with each other. Electrically active organs like the heart or the stomach possess a total number of cells on the order of 10^{10} (Malmivuo & Plonsey, 1994). As a consequence, a mathematical model that describes every single discrete component of such a system raises serious issues of computational tractability. To overcome this problem, investigators have employed continuum techniques based on averaging the electrical properties of single cells over a length greater than the single cell itself. The continuum modelling approach has been used extensively to model excitable tissues such as cardiac (Roth & Wikswo, 1986; Fischer *et al.*, 2000; Pullan *et al.*, 2005), gastric (Buist *et al.*, 2004) and intestinal (Lin *et al.*, 2006a) tissues.

One such technique is the bidomain model where the tissue consists of two interpenetrating domains representing the intra- and the extra- cellular spaces respectively. Figure 1.8 shows what will be referred to as the control volume,

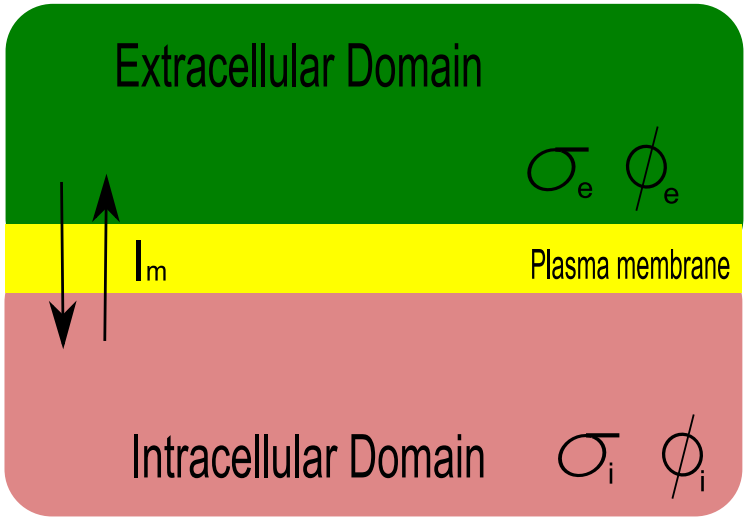

Figure 1.8: Schematic representation of the two domains of the bidomain framework. The extracellular domain is characterised by conductivity σ_e and potential ϕ_e while the intracellular domain is characterised by conductivity σ_i and potential ϕ_i.

composed of the two domains as well as the cell membrane separating them. Each domain is characterised by a potential field ϕ and the transmembrane potential can be expressed as

$$V_m = \phi_i - \phi_e \tag{1.17}$$

where ϕ_i and ϕ_e are intra- and extra- cellular potentials respectively. For each of the two domains, the multidimensional version of the Ohm's law can be written as

$$\mathbf{J}_i = -\sigma_i \nabla \phi_i \tag{1.18}$$

$$\mathbf{J}_e = -\sigma_e \nabla \phi_e \tag{1.19}$$

where the $\mathbf{J}$ terms are current densities and the σ terms are conductivities.

Conservation of charge dictates that there can be no net current flow into or out of the control volume. However, current can move between the intra- and extra-cellular spaces across the intervening membrane. Therefore we can write

$$-\nabla \cdot \mathbf{J}_e = \nabla \cdot \mathbf{J}_i = A_m I_m \tag{1.20}$$

where A_m is the surface to volume ratio of the cell and I_m represents the total transmembrane current. In other words, Equation 1.20 states that the current flowing out of one domain must be equal and opposite to that entering the other domain. Combining Equation 1.20 with Equations 1.18 and 1.19 yields

$$\nabla \cdot (\sigma_i \nabla \phi_i) = -\nabla \cdot (\sigma_e \nabla \phi_e) = A_m I_m \tag{1.21}$$

Equation 1.21 can be split into two equations, that, after eliminating the variable ϕ_i by substituting Equation 1.17 into 1.21, can be written as

$$\nabla \cdot ((\sigma_i + \sigma_e) \nabla \phi_e) = -\nabla \cdot (\sigma_i \nabla V_m) \tag{1.22}$$

$$\nabla \cdot (\sigma_i \nabla V_m) + \nabla \cdot (\sigma_i \nabla \phi_e) = A_m I_m \tag{1.23}$$

Following the Hodgkin and Huxley approach (Section 1.4.1), I_m can be expressed as

$$I_m = C_m \frac{\partial V_m}{\partial t} + I_{ion} \tag{1.24}$$

where C_m is the membrane capacitance and I_{ion} represents the summation of all the ionic currents flowing through the ion channels in the cell membrane. Fine details of cellular physiology can be incorporated into the tissue description

through the I_{ion} term. Substituting Equation 1.24 into Equation 1.23 yields

$$\nabla \cdot ((\sigma_i + \sigma_e)\nabla\phi_e) = -\nabla \cdot (\sigma_i \nabla V_m) + I_{s1} \tag{1.25}$$

$$\nabla \cdot (\sigma_i \nabla V_m) + \nabla \cdot (\sigma_i \nabla \phi_e) = A_m(C_m \frac{\partial V_m}{\partial t} + I_{ion}) - I_{s2} \tag{1.26}$$

where externally applied currents are taken into account through the I_s terms. Equations 1.25 and 1.26 are known as the bidomain equations.

Under the simplifying assumption that the extra-cellular domain is highly conducting, ϕ_e can be assumed constant and therefore its gradient is zero. Equations 1.25 and 1.26 can then be reduced to the following monodmain equation.

$$\nabla \cdot (\sigma \nabla V_m) = A_m(C_m \frac{\partial V_m}{\partial t} + I_{ion}) - I_{stim} \tag{1.27}$$

The monodomain approach is particularly suitable when the object of investigation is a biological tissue in isolation (i.e., without any externally applied stimuli that influence cellular ionic currents), whereas the full bidomain equations are required when the extracellular electrical state is of interest (Potse *et al.*, 2006). Having one equation instead of two, the monodomain approach has been adopted in many cases because of the reduction in computational time and complexity (Porras *et al.*, 2000; Potse *et al.*, 2006; Weiss *et al.*, 2007).

Chapter 2

GI Modelling Review

This chapter presents a summary of the computational models in the area of GI electrophysiology that have been developed over the past three decades. Single cell descriptions will be analysed in Section 2.1. Mathematical models at tissue and organ level will be discussed in Section 2.2. For each model, a critical assessment of their strengths and weaknesses is provided.

2.1 Single Cell GI Models

2.1.1 A Thermodynamic Approach: Skinner *et al.*

A statistical rate theory (SRT) approach was used by Skinner *et al.* (1993) to model some of the pumps and exchangers believed to be expressed in gastric smooth muscle. According to the SRT, the net rate of reaction, j, for any pump or exchanger where the reaction

$$\mathrm{A+B} \rightleftharpoons \mathrm{C+D} \tag{2.1}$$

occurs, is given by

$$j = K(\delta - \delta^{-1}) \tag{2.2}$$

where K is the equilibrium exchange rate which, in general, depends on the concentration of the biochemical species that regulate the function of the exchanger and δ is given by

$$\delta = exp(\frac{\mu_A + \mu_B - \mu_C - \mu_D}{RT}) \tag{2.3}$$

where a generic μ_x is defined as the electrochemical potential of the component x and is, by definition, given by

$$\mu_x = \mu_x^0 + RTlog(a_x) + zF\phi. \tag{2.4}$$

Here μ_x^0 is the reference chemical potential for species x, R and T are the universal gas constant and absolute temperature respectively. a_x is the activity and z is the valence of species x, F is the Faraday's constant and ϕ is the electrical potential. δ^{-1} refers to the reaction rate of Equation 2.1 going from left to right and subsequently changes the signs in the numerator of Equation 2.3. Specific expressions following this approach have been derived for the Ca^{2+} pump, the Na^+-Ca^{2+} exchanger and the Na^+-K^+ pump. The authors then proceed to integrate the thermodynamic expressions derived for the pumps and exchangers into a whole cell electrophysiological description based on a Hodgkin and Huxley approach where four ion channel types were included alongside the electrical contribution of the three pumps and exchangers (Figure

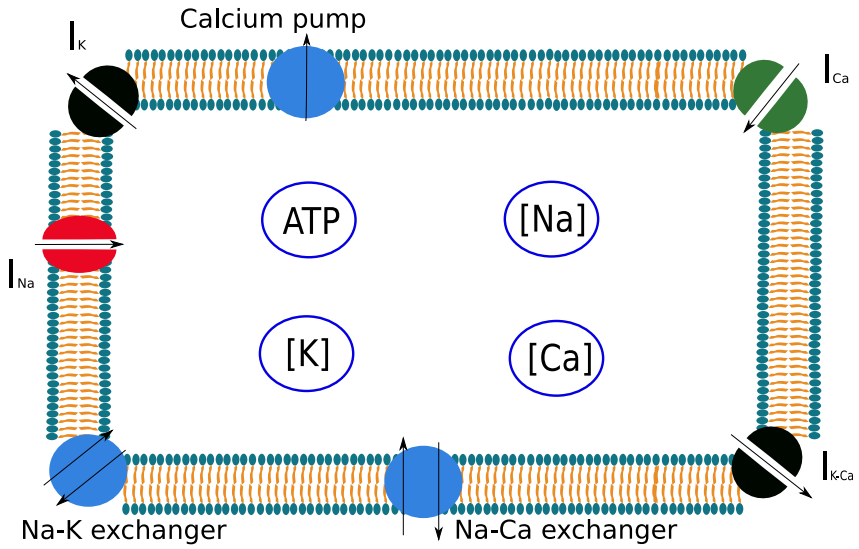

Figure 2.1: Schematic view of the Skinner *et al.* (1993) model of a gastric SM cell

2.1). The governing equation is given by

$$C_m \frac{dV_m}{dt} = -(I_{Na} + I_K + I_{Ca} + I_{K-Ca} + I_{Na-Ca} + I_{Ca-pump} + I_{Na-K}) \quad (2.5)$$

where I_{Na} is a Na^+ current, I_K is a K^+ current, I_{Ca} is a Ca^{+2} current, I_{K-Ca} is a Ca^{2+}-activated K^+ current, I_{Na-Ca}, $I_{Ca-pump}$ and I_{Na-K} are the electrical currents generated by Na^+-Ca^{2+} exchanger, Ca^{2+} pump and Na^+-K^+ pump respectively, and all the other terms have the same meaning as in Equation 1.1. Figure 2.1 also shows the main four intracellular species that were tracked over time by means of explicit ordinary differential equations (ODE) describing their concentration and, for the case of ATP, also its biochemical configurations. Particular attention is dedicated to modelling the ATP-related metabolic reactions because, in this publication, the oscillatory ATP concen-

tration (and its ability to regulate pumps and exchangers) is assumed to be primary source of the oscillatory electrical behaviour exhibited by the gastric musculature (slow waves).

The novel thermodynamic approach used to generate equations for the description of pumps and exchangers is the focus of this publication. This approach proved particularly suitable for modelling the intracellular biochemical metabolic reactions, mainly involving phosphate species, that were assumed to regulate the function of the pumps and exchangers. This gave the authors the opportunity to build on the assumption that an oscillation in the concentration of one or more of the metabolic components (i.e., ATP) gave rise to oscillating behaviour in the membrane pumps and exchangers which in turn, resulted in the observed oscillating membrane potential of gastic SM cells. Unfortunately this assumption has been later disproved as the oscillating pattern of SM membrane potential was found to be linked to the connection to ICC and not to any internal intracellular process occurring in SM cells (Sanders *et al.*, 2006a). Nevertheless, the Skinner model should be credited as the first attempt at describing the electrical activity in SM cells starting from the SRT governing the biochemical reactions.

2.1.2 A Simple Generic Model: Lang & Rattray-Wood

A simplified approach to modelling smooth muscle cellular activation was presented by Lang & Rattray-Wood (1996). Only four ion channel types were included in a Hodgkin and Huxley-type modelling framework. The governing

equation is given by

$$C_m \frac{dV_m}{dt} = -(I_{Ca} + I_{Kdel} + I_{K-Ca} + I_{leak}) \tag{2.6}$$

where I_{Kdel} is K^+ delayed rectifier current, I_{leak} is a leak current and all the other terms have the same meaning as in Equation 2.5. Intracellular Ca^{2+} dynamics were included in the description because of their regulatory effect on Ca^{2+} and K^+ channels within a submembrane space. The equations describing the ionic currents have been validated individually by comparing the simulated currents under voltage clamp conditions with the whole-cell experimental recordings under the same conditions. A variety of waveforms were presented as simulation results. By varying the size of the submembrane compartment as well as some of the ionic conductances (G_{K-Ca}, G_{Kdel}, G_{leak}), different *plateau* potentials are obtained, resembling experimental recordings from different regions of the GI tract. The Lang & Rattray-Wood (1996) model should be commended for presenting a very flexible and simple description of SM electrophysiology. Under a computational point of view, these qualities become even more apparent as potential multicellular simulations based on the Lang & Rattray-Wood model might benefit from its computational efficiency. Nevertheless, the biological complexity that this model is able to capture is relatively modest and its application range might be limited. Moreover it neglects the fundamental role of ICC in GI electrophysiology, not fully established at the time of publication.

2.1.3 The Miftakhov Models of the Small Bowel

Between 1996 and 1999 the research group headed by Miftakhov published a series of models of the small bowel (Miftakhov & Abdusheva, 1996; Miftakhov & Wingate, 1996; Miftakhov *et al.*, 1999a,b). These models attempted to produce a biophysical description of the cellular components believed to be responsible for intestinal motility. The models describe the activity of an intestinal smooth muscle cell under the control of an unmyelinated cholinergic neuron. Seven sets of equations were proposed to describe the electrophysiology of intestinal motility. Six of them were devoted to describing the electrical stimulus within the ENS: one for the dendritic mechanoreceptor, one for the propagation of soma action potentials, one for the axonal action potentials, two for the the biochemical dynamics within the adrenergic synapse and one for the generation of the excitatory post-synaptic potential. The latter was coupled with the seventh set of equations describing intestinal smooth muscle electrophysiology. A total of five ion channels were included in the SM model, two Ca^{2+}, two K^+ and one Cl^- channel

$$\alpha C_m \frac{dV_m}{dt} = -(I^f_{Ca} + I^s_{Ca} + I_{Ca-K} + I_K + I_{Cl}) \tag{2.7}$$

Here α is a numerical parameter of unspecified nature, C_m is the membrane capacitance and V_m is the membrane potential. I^f_{Ca} and I^s_{Ca} are fast and slow Ca^{2+} currents, corresponding to T-type and L-type channels, respectively. I_{Ca-K} is a Ca^{2+}-activated K^+ current, I_K is a K^+ current and I_{Cl} is a chloride current. The formalism used for each ionic current was adapted from the

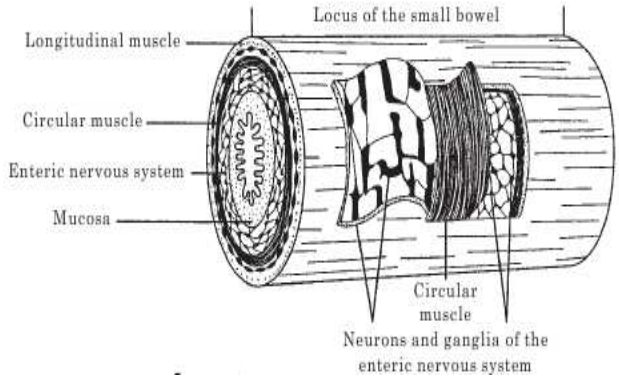

Figure 2.2: A schematic diagram of the structural components responsible for intestinal motility (locus) as hypothesised by Miftakhov *et al.* (1999a). Note the lack of ICC whose fundamental pacemaker function for intestinal motility was unknown at the time of publication.

Hodgkin and Huxley approach. The kinetics constant of the ion channels, however, have been adapted to reproduce realistic intestinal slow waves. As the authors sought to model not only the slow waves but also the spiking activity which is associated with contraction, a phenomenological time-dependence was added to the T-type Ca^{2+} conductance (g^f_{Ca})

$$g^f_{Ca} = \begin{cases} at^2 + bt + c & \text{if } [Ca^{2+}] > 0.5 \text{ mM} \\ 0.51 & \text{if } [Ca^{2+}] \leq 0.5 \text{ mM} \end{cases} \tag{2.8}$$

This time-dependence allowed the authors to produce simulation results that appear similar to the recorded spike activity in the intestine.

These publications should be credited for having pioneered biophysically based cellular modelling in the GI tract. Unfortunately, some of the underlying assumptions on which the models were based upon later proved to be

incorrect. In particular, the role of ICC as pacemaker cells was unknown at the time of publication and therefore the authors assume the existence of a *locus* (Fig 2.2) formed by ENS neurons and SM cells where the neurons provided the electrical stimulus for SM cell to contract. In this model, the smooth muscle cells are therefore responsible for slow wave activity. The Miftakhov models therefore do not take into account the slow wave pattern generated by the ICC network in the intestine that acts in combination with the ENS to regulate intestinal motility. Furthermore, the description of the spike activity is obtained through a direct time-dependency of the T-type Ca^{2+} conductance. This empirical description makes the model unsuitable for long time simulations, as the value of g^f_{Ca} will increase indefinitely and unrealistically as simulation time increases. For these reasons, the potential applications of the Miftakhov models are somewhat limited.

2.1.4 A Phenomenological Model: Aliev *et al.*

After the role of ICC as pacemaker cells in the GI tract became apparent, Aliev *et al.* (2000) proposed a simple phenomenological description of the electrical activity in the intestine. The model is based on the following two linear ODE modified from the original equations by Fitzhugh (1962).

$$\frac{du}{dt} = ku(u-a)(1-u) - v \tag{2.9}$$

$$\frac{dv}{dt} = \epsilon(\gamma(u-\beta) - v) \tag{2.10}$$

Here u represents the normalised transmembrane potential and v is a recovery variable. All of the parameters (k, a, ϵ, δ, β) have been tuned in order to replicate the observed intestinal slow wave profile (Figure 2.5). The major strength of this model is its simplicity and, subsequently, its computational efficiency that makes it particularly suitable for inclusion in larger scale models of tissues (e.g. Pullan *et al.* (2004)). On the other hand, no attempt is made to describe the underlying physiology of the ion channels responsible for the generation of the slow waves. The parameters in the model have no direct physical meaning, making the Aliev model not applicable for the study of ion channel pathophysiologies. Moreover, Lin *et al.* (2006b) reported computational stability issues with the Aliev model when simulating long periods of slow wave activity.

2.1.5 Modelling Intracellular IP3 Dynamics: Imtiaz *et al.*

As the regulatory effects of intracellular IP3 on slow wave activity became apparent from experimental results, Imtiaz *et al.* (2002) proposed a mathematical description of slow wave regulation by voltage-dependent IP3 dynamics aimed at explaining experimental observations on intact muscle preparations from the guinea-pig stomach. Voltage dependent regulation of IP3 synthesis had been postulated as one of the key mechanisms in slow wave generation. The electrophysiological model of the plasma membrane is extremely simplified, reflecting the intention of the authors to focus on intracellular IP3-related

biochemical processes. The governing equation is given by

$$C_m \frac{dV_m}{dt} = I_{lumped} - I_{Ca} + I_{inj} \tag{2.11}$$

where all the symbols have the same meaning as in Equation 2.5 and I_{lumped} is simply given by

$$I_{lumped} = G_{lumped} * (V_m - E_{lumped}) \tag{2.12}$$

This represents, in a single term, all of the ion channels in the plasma membrane except I_{Ca}. E_{lumped} is the reversal potential of this abstract current and G_{lumped} its maximal conductance. I_{inj} is a current injected into the cell to control the membrane potential. This oversimplified and abstract formulation finds its justification in the stated intention of focusing on the relationship between IP3 dynamics and membrane potential. Having an explicit term (I_{inj}) that artificially modifies the membrane potential (Figure 2.3) allows an easy manipulation of the slow wave profile. The postulated regulatory feedback loop involving I_{inj}, V_m, intracellular Ca^{2+} and IP3 is shown in Figure 2.3. Slow wave profiles for different values of I_{inj} were presented and compared to experimental slow wave recordings following external application of hyperpolarising or depolarising stimuli. Good correspondence between simulation results and experimental observation was reported for a variety of experimental settings and this was used to reinforce the the hypothesis of voltage-mediated IP3 synthesis. While providing interesting insights into the possible regulatory mechanisms between IP3 and slow wave activity, this model focuses

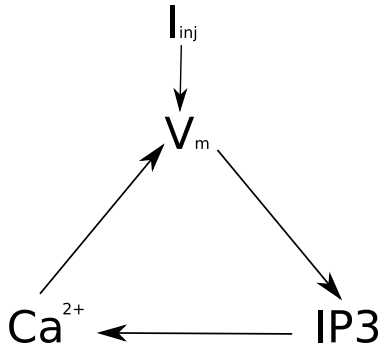

Figure 2.3: Schematic view of the regulatory loop of IP3, Ca^{2+} and V_m as modelled by Imtiaz *et al.* (2002).

only on one particular aspect of the complex process of slow wave generation. Its usefulness in understanding ion channel physiology is also limited by the oversimplified description of the plasma membrane. Furthermore, the role of voltage-mediated synthesis of IP3 as primary origin of the oscillatory behaviour of the membrane potential of the slow waves has been called into question as it became apparent that the interplay between mitochondria and ER (IP3-mediated) Ca^{2+} handling may constitute the fundamental process in slow wave generation (Ward *et al.*, 2000).

2.1.6 A Model of an Intestinal ICC: Youm *et al.*

The first model of a biophysically based cellular description of an ICC was developed by a South Korean research group (Youm *et al.*, 2006). This model carefully characterises the biophysical properties of the major ion channels believed to be expressed in ICC. A total of four ion channels and three exchangers were included in the description of the plasma membrane (Figure 2.4.

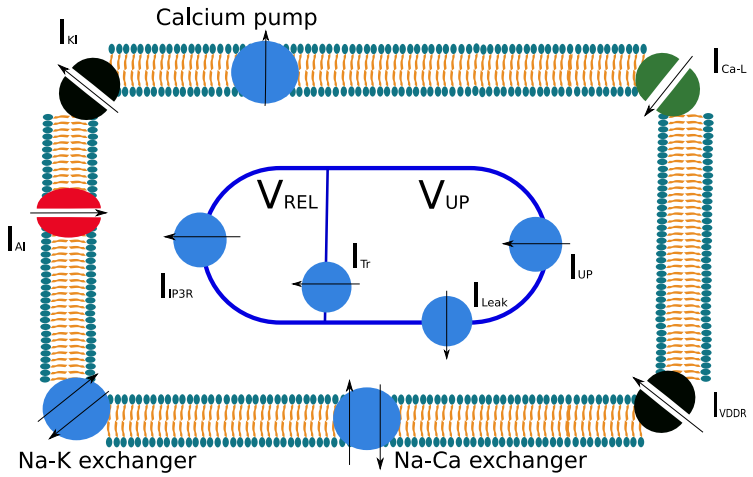

Figure 2.4: Schematic view of the Korean model of intestinal ICC (Youm *et al.*, 2006), where four membrane ion channels, three ionic exchangers and the Ca^{2+} handling by the SR are included.

The governing equation is given by

$$C_m \frac{dV_m}{dt} = -(I_{VDDR} + I_{K1} + I_{CaL} + I_{AI} + I_{Na-Ca} + I_{Ca-pump} + I_{Na-K}) \quad (2.13)$$

where all the symbols have the same meaning as in Equation 2.7, I_{VDDR} is a DHP-resistant Ca^{2+} current, I_{K1} is an inward rectifier K^+ current, I_{CaL} is a L-type Ca^{2+} current and I_{AI} is an autonomous inward current that guarantees the spontaneity of slow wave generation. This current was modelled according to experimental recordings from the mouse small intestine (Goto *et al.*, 2004) and it was assumed to be regulated by intracellular Ca^{2+} which, in turn, is regulated by the IP3-mediated release of Ca^{2+} from the ER. This assumption has been later reinforced by further experimental data and is currently accepted as physiologically relevant. For this reason, the authors detail the intracellular Ca^{2+} dynamics as the result of the interplay between membrane

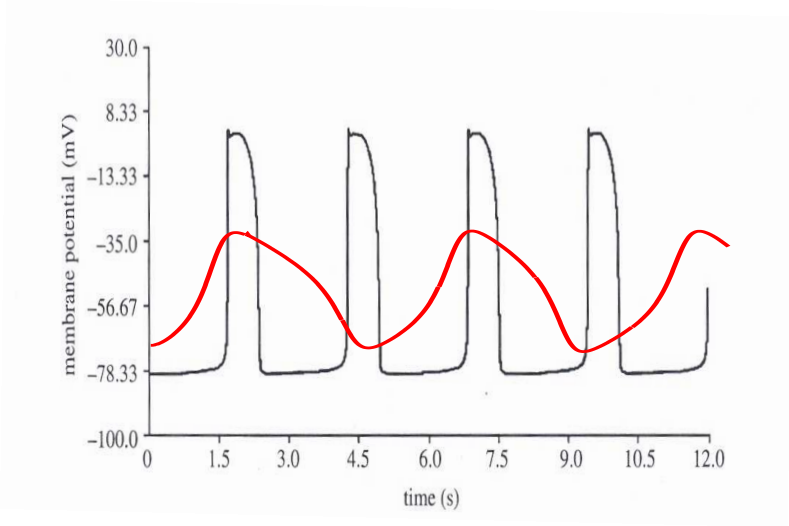

Figure 2.5: Results from two models of intestinal ICC. The results of the model of murine intestinal ICC by Youm *et al.* (2006) (in black) compared to the predicted slow wave profile in human intestinal ICC according to the Aliev model (Aliev *et al.*, 2000), shown in red.

Ca^{2+} channels (I_{CaL} and I_{VDDR}) and the Ca^{2+} handling by the sarcoplasmic reticulum (SR) (I_{IP3R}, I_{UP} and I_{Leak}). Nevertheless, recent experiments have also highlighted the role of mitochondria in regulating the intracellular Ca^{2+} concentration as one of the fundamental components needed for the generation of slow waves. Numerous investigators have indeed shown that in presence of mitochondrial uncouplers, ICC lose the ability to generate slow waves (Kim *et al.*, 2006a; Ward *et al.*, 2000). The absence of mitochondria for the regulation of the intracellular Ca^{2+} concentration constitutes the major weakness of this model. Furthermore, the authors do not include some of the ion channels whose presence has been confirmed in ICC, such as the Ca^{2+}-activated (BK) K^+ channels (Cho & Daniel, 2005), ether-a-go-go (ERG) K^+ channels (McKay *et al.*, 2006) and Na^+ channels (Strege *et al.*, 2003). These weaknesses may

hinder the potential use of the model in further investigation with clinical relevance. For example, Na^+ channels in the GI tract have been recently suggested as responsible for the onset of a series of debilitating symptoms that affects patients diagnosed with a cardiac SCN5A mutation (Locke *et al.*, 2006). In such a case, a cellular model that includes a description of Na^+ channels would be required in order to capture the influence of a Na^+ channel mutation on the cellular behaviour and obtain better insight into the pathophysiological mechanisms. The slow wave profile predicted by the model of Youm *et al.* (2006) is shown in Figure 2.5.

2.2 Multi Dimensional Tissue Models

2.2.1 Models Based on Coupled Relaxation Oscillators

The oscillatory behaviour of the membrane potential in the GI musculature has been known for several decades and the first attempts at modelling slow wave propagation were based on sets of ODEs containing polynomial equations that, once solved, gave rise to oscillatory behaviour in the dependent variable (in this case, the amplitude of the slow waves). The theoretical framework is based on the Van der Pol equation, which was originally formulated to describe self-sustaining oscillations in which energy is fed into small oscillations and removed from large oscillations. The Van der Pol equation is given by

$$\frac{\partial^2 x}{\partial t^2} - \alpha(1 - x^2)\frac{\partial x}{\partial t} + \omega^2 x = 0 \tag{2.14}$$

where x is the dependent variable (the amplitude of the oscillations), α is the damping coefficient and ω is the undamped natural frequency of the oscillations. Equation 2.14 can be reduced to a set of two first order differential equations. Following the approach proposed by Fitzhugh (1962) and Roberge (1969), Sarna *et al.* (1971) derived, from Equation 2.14, the following equations for each oscillator

$$\frac{dx}{dt} = \alpha(ey + fx + gx^2 + hx^3) \tag{2.15}$$

$$\frac{dy}{dt} = -\frac{1}{\alpha}(by + \omega x^2 + cx^2 + dx^3 - a) \tag{2.16}$$

where x remains as the dependent variable, y is an auxiliary state variable and all the other symbols are model parameters with no direct physical meaning. By appropriately tuning these parameters, it was possible to reconstruct an oscillating profile that replicated slow wave activity. In an electrically coupled tissue, such as the gastric musculature, each oscillator operates under the influence of its neighbours. The equations describing the n^{th} oscillator are given by

$$\frac{dx_n}{dt} = \alpha(ey_n + fx_n + gx_n^2 + hx_n^3 + I_n) \tag{2.17}$$

$$\frac{dy_n}{dt} = -\frac{1}{\alpha}(by_n + \omega x_n^2 + cx_n^2 + dx_n^3 - a) \tag{2.18}$$

where I_n denotes the combined input of other oscillators to the n^{th} oscillator. In the simplified example of Figure 2.6, I_n would be given by

$$I_n = C_{n1}x_{n-1} + C_{n2}x_{n+1} - C_{n3}x_{n+1} \tag{2.19}$$

where C_{n1}, C_{n2} and C_{n3} are the coupling coefficients.

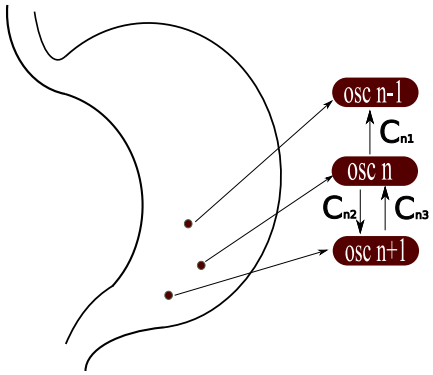

Figure 2.6: Simplified diagram showing three coupled relaxation oscillator (osc n-1, osc n and osc n+1) arbitrarily placed in the antral region of the stomach as in the approach proposed by Sarna *et al.* (1972a). C_{n1}, C_{n2} and C_{n3} are coupling coefficients. Note that this a simplified example with only three oscillators only for illustrative purposes. The original publication (Sarna *et al.*, 1972a) describes thirteen oscillators arranged throughout the distal corpus and antral region of the stomach (see Figure 2 of Sarna *et al.* (1972a)).

This approach was widely used in a variety of simulated experimental setups (Nelsen & Becker, 1968; Sarna *et al.*, 1972a,b). Nevertheless, several issues were raised regarding its adequacy and utility (Publicover & Sanders, 1989). The critisisms were based on two main limitations of the relaxation oscillator models. Firstly, the ability of such models to accurately replicate the waveforms that were experimentally recorded along the GI tract was put into question as Equations 2.15 and 2.16 proved unable to replicate important features of the slow waves such as the relatively flat inter slow wave profile and the biphasic slow wave shape (rapid upstroke followed by partial repolarisation and plateau phase) recorded from antral preparations. Secondly, doubts were cast over the utility of relaxation oscillator models in predicting the effects of pharmacological agents. The parameters of Equations 2.15 and

2.16 have no direct physical meaning and it is very difficult, if not impossible, to correlate a change in one of these parameters to the effects of a particular chemical or drug and to make predictions pertaining to its effects on the slow wave activity. Ultimately, because of these two limitations, relaxation oscillator models became less popular and the development of biophysically-based realistic mathematical descriptions of the cellular events that lead to slow wave generation was advocated (Publicover & Sanders, 1989).

2.2.2 A Planar Model: Sperelakis & Daniel

Sperelakis & Daniel (2004) simulated a two-dimensional sheet of intestinal ICC and SM cells using a dedicated software application called PSpice with the aim of investigating the propagation of the excitatory signal from ICC to SM cells. They simulated a 5X5 planar network of SM cells that was activated at one corner by a single ICC. The main aim of the paper was to elucidate whether gap junction communication between ICC and SM cells is required for the propagation of the electrical stimulus within the gastric musculature. For this purpose the authors modelled a situation where there are no gap junctions in the 2D network. In their model, excitation was only transmitted by electric fields that spread through the intercellular clefts (junctional clefts). The authors concluded from their simulation results that an ICC is capable of exciting a network of SM cells in absence of gap junctions. Careful examination of the paper, however, reveals that the membrane potential in the ICC reached non-physiological values. In the results section, the ICC membrane potential had an overshoot to +32 mV a value that is at least 40 mV higher than the

physiological range (Hirst & Edwards, 2006) and is, in fact, more similar to cardiac pacemaker cells than intestinal ICC. In a study where the attenuation of the signal generated by the ICC is the main object of investigation, the non-physiological excitation of the ICC might have a non-negligible impact on the conclusions that were drawn. Furthermore, in the planar network that was modelled, each cell was connected to its neighbours by resistive elements that the authors called junctional resistences. This is postulated to simulate a situation where there are no gap junctions connecting the cells. However, resistive elements have been extensively and successfully employed to model gap junction connections between cells (Vogel & Weingart, 2002), which is precisely what they are supposed not to represent in this model. The conclusions that can be drawn by the use of this model can be put into question by these discrepancies and the potential use of this model is therefore limited for the study of GI pathophysiology.

2.2.3 A Cable Model: Edwards & Hirst

A one dimensional cable description of the gastric musculature was developed by Edwards & Hirst (2005) for the study of the propagation of slow waves. The authors aimed to characterise the propagation of the electrical impulse from the ICC in the myenteric plexus towards the longitudinal SM layer and the circular SM layer. For this purpose they introduced three equivalent electrical circuits, one for the ICC-MY, one for the circular SM layer and one for the longitudinal SM layer (Figure 2.7). The equivalent circuits representing the different muscle layers were made of parallel connections between a capacitor

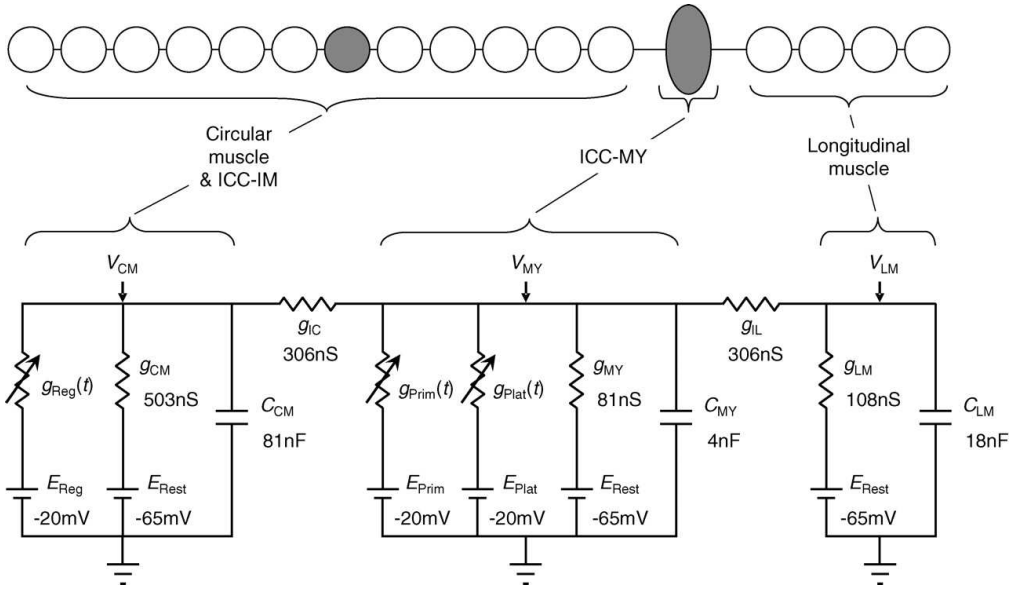

Figure 2.7: Cable model of the gastric musculature as published by Edwards & Hirst (2005). Each layer in the gastric musculature is modelled with a simple electrical circuit.

and one or more variable resistances. The governing equations for each of the cell types was as per Equation 1.1.

The model of the circular layer (Edwards & Hirst, 2003) is based on a phenomenological description of the plateau phase of the SM slow waves (termed regenerative potentials) that was assumed by the authors to be the result of the summation of unitary potentials (small increases in membrane conductance that have been observed experimentally (Beckett *et al.*, 2004)). The rate of discharge of unitary potentials (λ) was assumed to be dependent on the concentration of a messenger, whose identity was suggested to be IP3, according to the following Hill equation

$$\lambda = \frac{\lambda_{max}}{1 + (\frac{K_d}{[messenger]})^H} \tag{2.20}$$

where λ_{max} is the maximal discharge rate, K_d and H are the Hill half-value and steepness parameters respectively and [messenger] represents the concentration of the messenger, which was assumed to be determined by the following two-stage biochemical reaction.

$$[precursor] \underset{K_B}{\overset{mhK_F}{\rightleftharpoons}} [intermediate] \xrightarrow{K_M} [messenger] \xrightarrow{K_H} \tag{2.21}$$

Here m and h are Hodgkin and Huxley gating variables, K_F and K_B are the forward and backward reaction rates respectively for the intermediate species (of unspecified nature), and K_M and K_H are the reaction rates for the messenger formation and degradation respectively. The rate of discharge of unitary potentials was used to compute the value of $g_{reg}(t)$ in Figure 2.7 as follows. First, $g_{reg}(t)$ was written as the summation of N unitary conductances

$$g_{reg}(t) = \sum_{j=1}^{N} g_j(t) \tag{2.22}$$

where each $g_j(t)$ can be written, assuming a particular unitary event starting at time t_j, as

$$g_j(t) = \begin{cases} 0 & \text{if } t < t_j \\ A_j * (e^{-(t-t_j)/0.434} - e^{-(t-t_j)/0.077})^3 & \text{if } t \geq t_j \end{cases} \tag{2.23}$$

where the random variable A_j represents the amplitude of the unitary potential. Second, at every time step, the total number of unitary potentials, N,

was related to the mean frequency of discharge of unitary potentials by

$$\sum_{j=1}^{N}(t_j - t_{j-1}) = \frac{N}{\lambda} \tag{2.24}$$

Hence, at every time step, λ is calculated from the equations arising from the reaction in Equation 2.21 and the intervals between forthcoming unitary potentials are modified accordingly (Equation 2.24), allowing the calculation of $g_{reg}(t)$ using Equations 2.22 and 2.23. The membrane potential in the CM layer (left of Figure 2.7) is then calculated by

$$C_{CM}\frac{dV_{CM}}{dt} = -(g_{reg}(t) * (V_m + 20) + g_{CM} * (V_m + 65)) + I_{IC} \tag{2.25}$$

where I_{IC} is the current exchanged between ICC-MY and CM layers and is given by

$$I_{IC} = g_{IC} * (V_{CM} - V_{MY}) \tag{2.26}$$

The slow wave activity in the ICC-MY network was modelled by the equivalent circuit shown in Figure 2.7 (centre). The variable conductance $g_{prim}(t)$ was introduced to model the primary component of the slow wave and is given by

$$g_{prim}(t) = G_{PRIM} * A * N \tag{2.27}$$

where G_{PRIM} is a maximal conductance value, and A and N are Hodgkin and Huxley-type voltage dependent gating variables. The other variable conductance $g_{Plat}(t)$ was introduced to simulate the plateau phase of the slow wave in the ICC. Since this phase was assumed by the authors to be the result

of a summation of unitary potentials, the same formulation used for $g_{reg}(t)$ was again employed. The governing equation for the ICC-MY layer (centre of Figure 2.7) is then given by

$$C_{MY}\frac{dV_{MY}}{dt} = -(g_{Plat}(t) * (V_m + 20) + g_{prim}(t) * (V_m + 20) + \\ + g_{MY} * (V_m + 65)) - I_{IC} - I_{IL} \quad (2.28)$$

where I_{IL} is the current exchanged between the ICC-MY and LM layers and is given by

$$I_{IL} = g_{IL} * (V_{LM} - V_{MY}) \quad (2.29)$$

Finally, the longitudinal muscle layer was modelled by the simple circuit shown on the right of Figure 2.7. The governing equation is given by

$$C_{LM}\frac{dV_{LM}}{dt} = -g_{LM} * (V_m + 65) + I_{IL} \quad (2.30)$$

The model presented by Edwards & Hirst (2005) accurately reproduces slow wave activity recorded from the different layers of the guinea-pig stomach. This model is phenomenological in nature as only limited attempts at modelling the underlying physiology of the cellular components have been made. All of the conductances in Figure 2.7 have no direct physical meaning that relates them to actual ion channels expressed in ICC and SM cells; only the dynamics of synthesis and degradation of the intracellular messenger (Equation 2.21) represents an attempt of modelling a biophysical process that underlie the generation of the slow waves. The major limitation here is, therefore, that

no investigation on how individual ion channels pathologies affect slow wave propagation is possible.

2.2.4 The Auckland Stomach and Small Intestine Models

Over the last decade, a research group at the University of Auckland has developed a series of anatomically realistic models of gastric and intestinal electrophysiology (Buist *et al.*, 2004; Lin *et al.*, 2006b; Pullan *et al.*, 2004). The anatomical details of the organs under investigation (i.e., stomach and small intestine) have been digitised from photographic images from the Visible Human Project (Spitzer *et al.*, 1996) (Figure 2.8). A computational three-dimensional mesh has then been generated over the geometries.

Equations 1.25 and 1.26 have been integrated using a finite element method (FEM) approach over the meshes. Due to a lack of biophysically based cellular models of gastric and intestinal cells, the I_{ion} term in Equation 1.25 was calculated by tuning the parameters of the phenomenological Aliev model (Aliev *et al.*, 2000) in order to replicate the behaviour of stomach and intestinal ICC and SM cells. The solution of Equations 1.25 and 1.26 allows the computation of V_m as a function of time throughout the geometry of the stomach. An illustrative example of the results of such simulations is shown in Figure 2.9 where the transmembrane potential on the surface of stomach and intestine at different times instants is displayed. The potential field generated by the electrical activity within the stomach was then evaluated throughout the human torso, which was assumed to act as a volume conductor (Cheng *et al.*, 2006).

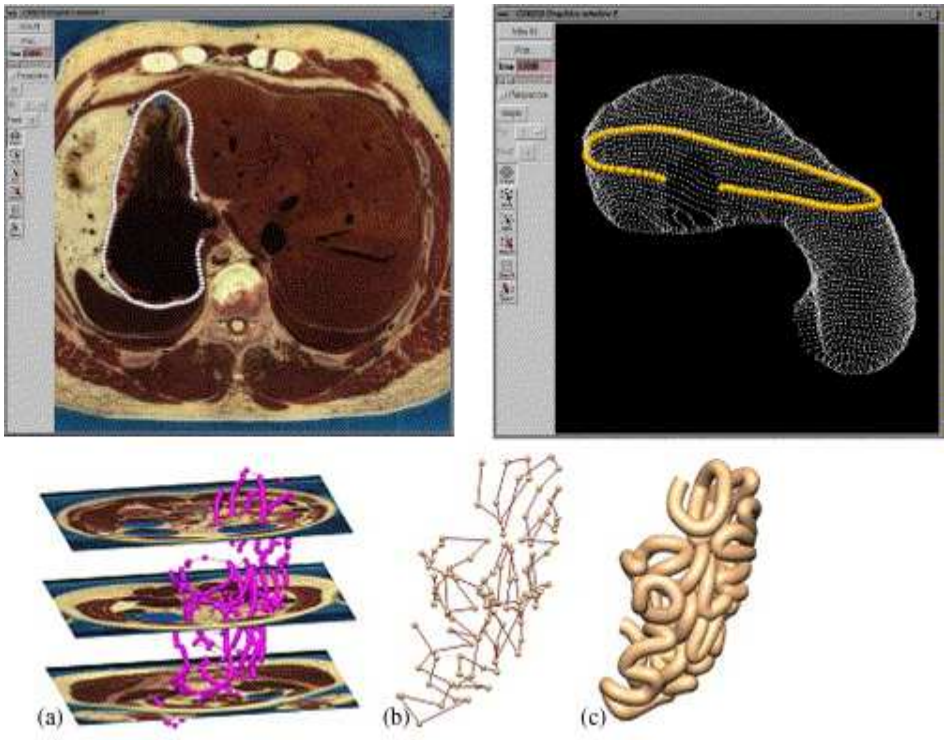

Figure 2.8: Upper panel: digitisation of the stomach from visible human project images (adapted from Pullan *et al.* (2004)). Lower Panel: the same operation performed for the small bowel (adapted from Lin *et al.* (2006b).

The electrical activity in the stomach can be recorded by means of surface electrodes placed on the skin (Chang, 2005). These recordings are known as electrogastrograms or EGGs. Computational models of the EGG are intended to help clinicians associate an abnormal EGG profile with an underlying gastric pathology. In this view, the Auckland research group developed the first computational framework for the simulation of the EGG. The modelling framework is based on the calculation of equivalent current sources **J** that would generate

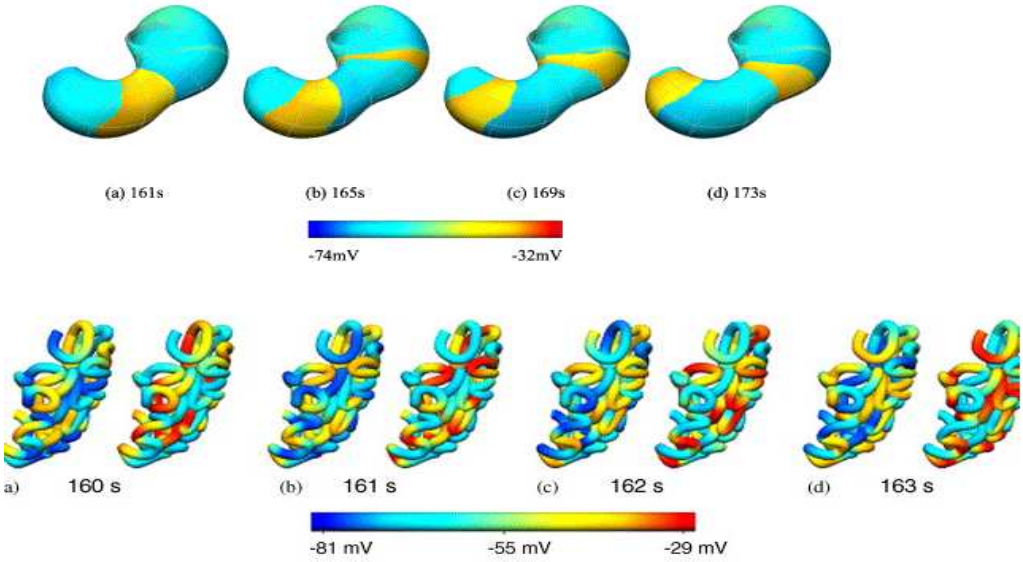

Figure 2.9: Upper panel: Simulation results of slow wave propagation in the stomach (adapted from Pullan *et al.* (2004)). Lower Panel: simulation results slow wave propagation in the intestine (adapted from Lin *et al.* (2006b)).

the same far-field electrical activity as the stomach through the equation

$$\mathbf{J} = -\sigma \nabla V_m \tag{2.31}$$

where σ is the stomach tissue conductivity. For each current source, the electrical field on the torso is given by

$$\nabla \cdot (\sigma_o \nabla \phi) = \nabla \cdot \mathbf{J} \tag{2.32}$$

where σ_o is the conductivity in the torso (a passive volume conductor) and ϕ is the torso potential. By calculating the potential at locations corresponding to the location of recording electrodes, realistic EGG traces were successfully simulated. As a further step, the magnetic field ($\mathbf{B}$) that is associated with the time-varying electrical field was also calculated by

$$\nabla \times \mathbf{B} = \mu_\mathbf{0} \mathbf{J} \tag{2.33}$$

where μ_0 is the magnetic permeability of free space, with the aim of helping the interpretation of magneto-gastrograms and magneto-enterogram traces.

As pointed out by the Auckland researchers themselves (Pullan *et al.*, 2004), the lack of an underlying biophysical cell model that is capable of describing at a fine scale the complexity of a variety of cellular events constitutes the major limitation of this approach. In fact, the phenomenological Aliev model is not capable of including a description of cellular abnormalities and evaluating their significance. Chapters 3 and 4 of this thesis are primar-

ily devoted to filling in this gap as the development of realistic, biophysically based cell models of ICC and SM cell will be discussed.

Chapter 3

Gastric Smooth Muscle Cell Model

3.1 Introduction

In this chapter we present a mathematical description of the electrophysiology of a gastric SM cell when activated by a neighbouring ICC. Section 3.2 details the description of the main intracellular processes and membrane ion channels that are currently believed to mediate the electrical cellular response of a gastric SM cell. In Section 3.3 the validation of the model in control and pharmacologically altered conditions is discussed.

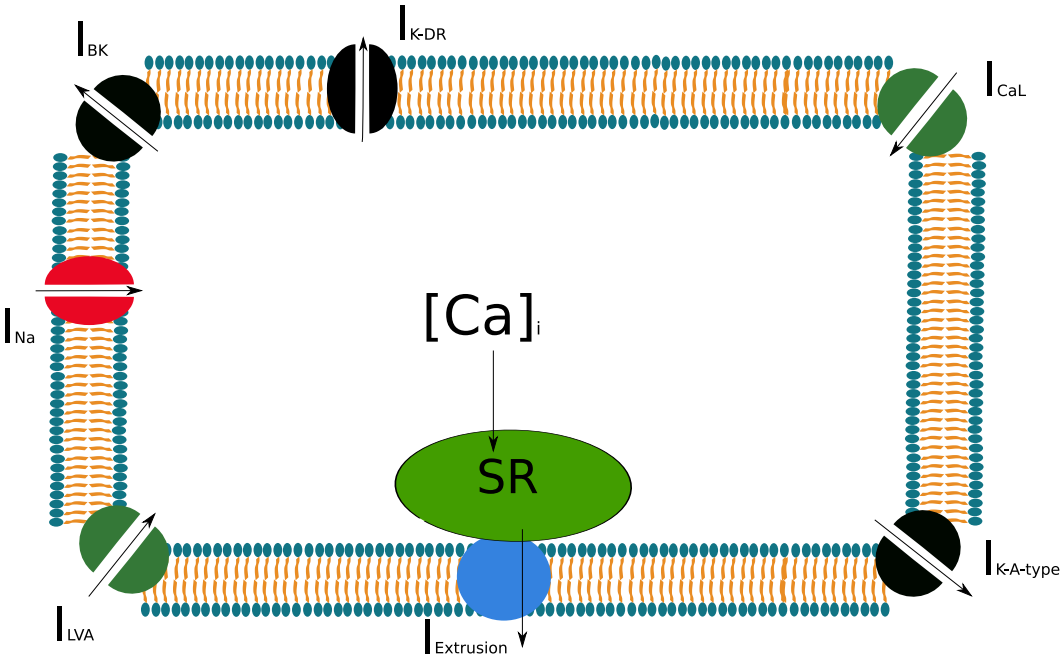

Figure 3.1: Schematic view of the gastric SM cell model. All the membrane ion channels and transport mechanisms included in the model are depicted.

3.2 Model Structure

3.2.1 Overview of the Model

The model is based on a classical Hodgkin-Huxley approach where the cell membrane is described by an equivalent electrical circuit consisting of a capacitance connected in parallel with a number of variable conductances representing the different pathways for the movement of charged ions. The time dependence of the membrane potential is governed by

$$C_m \frac{dV_m}{dt} = -I_{ion} + I_{stim} \tag{3.1}$$

where V_m (in mV) represents the transmembrane potential, C_m is the cell capacitance and its value was set at 77 pF (Sims, 1992a). I_{ion} (in pA) represents the sum of the ionic currents crossing the cell membrane. I_{stim} represents an external stimulus current that, *in vivo* is provided by the ICC network.

3.2.2 Membrane Ion Channels

Each of the major membrane ionic conductances that have been experimentally described in SM cells (shown in Figure 3.1) were included in the I_{ion} term of Equation 3.1.

$$I_{ion} = I_{CaL} + I_{LVA} + I_{Na} + I_{BK} + I_{K-DR} + I_{K-A-type} + I_{bK} \tag{3.2}$$

Details of each of these conductances are given below. Table 3.1 contain the parameters of the Hodgkin and Huxley-type gating variables for each conductance.

L-type Ca^{2+} Channels

I_{CaL} represents the influx of Ca^{2+} ions through voltage-gated, dihydropyridine (DHP)-sensitive L-type Ca^{2+} channels that are commonly expressed in the muscle cells of mammalian organisms.

$$I_{CaL} = G_{CaL} * d_{CaL} * f_{CaL} * f_{Ca} * (V_m - E_{Ca}) \tag{3.3}$$

Here E_{Ca} is the Nernst potential for Ca^{2+}, calculated using an extracellular Ca^{2+} concentration of 2.5 mM (Casteels, 1981; Knot *et al.*, 1995). The in-

tracellular Ca^{2+} concentration is the result of intracellular Ca^{2+} dynamics as described later in this section. G_{CaL} is the maximum channel conductance whose value (65 nS) was chosen to reproduce the Ca^{2+} current characteristics recorded in voltage clamp experiments on canine gastric smooth muscle cells (Vogalis *et al.*, 1992), and d_{CaL} and f_{CaL} are Hodgkin-Huxley type activation and inactivation gating variables respectively (see Table 3.1 and Figure 3.2). Measurements of the steady state voltage dependency of d_{CaL} and f_{CaL} in smooth muscle cells from guinea pig taenia coli (Yamamoto *et al.*, 1989), canine jejunum (Farrugia *et al.*, 1995), human colon (Xiong *et al.*, 1995) and canine colon (Langton *et al.*, 1989b) have shown prominent inter-organ variability. The half maximal values for the steady state activation vary from 6 mV in the canine jejunum (Farrugia, 1999) to 27.5 mV in the human colon (Xiong *et al.*, 1995). In the absence of direct experimental data from the stomach we have adopted the formulation of Akbarali & Giles (1993) where the half maximal value for the steady state activation was 17 mV. The steady state inactivation curve was taken from experiments on canine gastric smooth muscle (Vogalis *et al.*, 1992). Inactivation kinetics have been measured in human (Xiong *et al.*, 1995) and canine (Koh *et al.*, 2001) colonic myocytes as well as canine pyloric myocytes (Vogalis & Sanders, 1990). The time constant was taken from the same pyloric myocyte study (86 ms) which also showed the process to be largely voltage independent. Both activation and inactivation rate constants were measured during experiments at room temperature and have been adjusted to 37°C using a Q_{10} of 2.1 (Farrugia, 1999). Ca^{2+} dependent inactivation of the L-type Ca^{2+} current has been observed experimentally

where an accumulation of intracellular Ca^{2+} reduces the Ca^{2+} conductance and provides a negative feedback mechanism to control Ca^{2+} influx (Ganitkevich *et al.*, 1987; Vogalis *et al.*, 1992). This has been incorporated into the model through a Ca^{2+} dependent inactivation variable, f_{Ca}. The steady state equation for the f_{Ca} variable was estimated using data from canine gastric smooth muscle experiments (Vogalis *et al.*, 1992). By comparing the difference in the peak current elicited when Ba^{2+} or Ca^{2+} were used as the charge carrier at different voltages in conjunction with the corresponding changes in intracellular Ca^{2+} concentration, six data points were manually extrapolated and Equation 3.4 was fitted to these points to obtain the steady state behaviour.

$$f_{Ca\infty} = 1 - \frac{1}{1 + e^{-\frac{\Delta[Ca]_i - h_{Ca}}{s_{Ca}}}} \tag{3.4}$$

Here $\Delta[Ca]_i$ is the variation of cytoplasmic concentration (in nM) from the value in resting conditions, while h_{Ca} (201.4 mM) and s_{Ca} (13.1 mM) are the half concentration and slope factor respectively. In absence of data from gastric smooth muscle, we have adopted the formulation of ten Tusscher *et al.* (2004) for the rate constant of f_{Ca} (τ_{fCa}=2 ms).

Low Voltage Activated Ca^{2+} Current

I_{LVA} represents the low voltage-activated, fast-inactivating, DHP-insensitive component of the inward current that has been described in several types of SM cells (Farrugia, 1999; Vivaudou *et al.*, 1988; Yamamoto *et al.*, 1989; Yoshino *et al.*, 1988; Yunker & McEnery, 2003) and is often termed a T-type

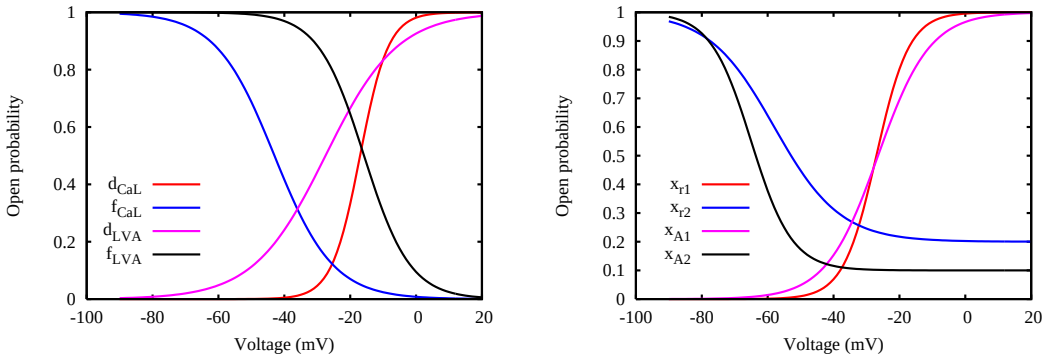

Figure 3.2: Steady states curves for voltage dependent gating variables in the SM cell. Ca^{2+} channel gating variables are shown in the left graph and K^+ channel gating variables are shown in the right graph.

Ca^{2+} current.

$$I_{LVA} = G_{LVA} * d_{LVA} * f_{LVA} * (V_m - E_{Ca}) \tag{3.5}$$

G_{LVA} is the maximum conductance of the channel and its value (0.18 nS) was chosen to reproduce voltage clamp experiments in canine gastric smooth muscle cells (in combination with I_{CaL}) (Vogalis *et al.*, 1991). The resulting reproduction is illustrated in Figure 3.3. d_{LVA} and f_{LVA} are Hodgkin-Huxley type activation and inactivation gating variables respectively and their steady-state kinetics (see Table 3.1 and Figure 3.2) were chosen to match experimental observations from *Bufo Marinus* gastric smooth muscle cells (Vivaudou *et al.*, 1988). Since this current was found to have an activation threshold at -50 mV and was still active at -10 mV, half maximal values of -27.5 mV and -18.8 mV were chosen for steady state activation and inactivation respectively. The activation time constant was obtained from time-to-peak data obtained by

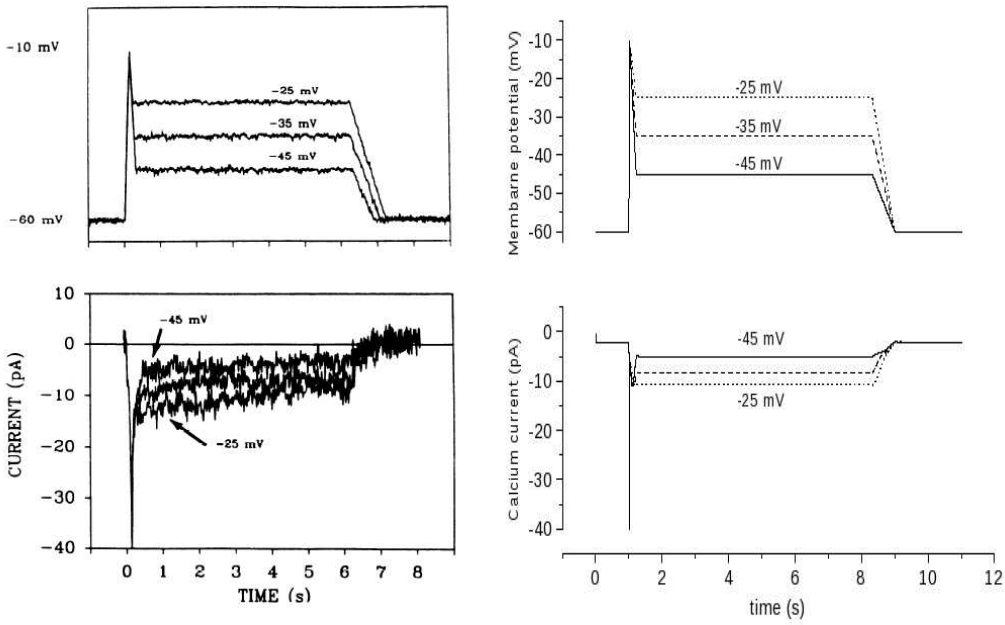

Figure 3.3: Experimental basis for the model description of Ca^{2+} currents. (A) Voltage clamp protocol applied to canine gastric smooth muscle. (B) Ca^{2+} currents elicited by the voltage clamp protocols from (A). (C) Simulated voltage clamp protocol. (D) Simulation of Ca^{2+} currents (I_{CaL}+I_{LVA}) elicited by the voltage clamp protocol shown in (C). (A) and (B) are reproduced from Vogalis *et al.* (1991).

Table 3.1: Parameters of the Hodgkin-Huxley type voltage dependent gating variables. Steady state equation for variable x is given by $x_\infty = \frac{A}{1+e^{\frac{V+V_h}{h}}} + (1.0 - A)$ and τ is the time constant.

Variable name	V_h(mV)	h (mV)	A	τ(ms)
d_{CaL}	17	-4.3	1.0	0.47
f_{CaL}	43	8.9	1.0	86
d_{LVA}	27.5	-10.9	1.0	3
f_{LVA}	15.8	7	1.0	$7.58*e^{0.00817*V_m}$
x_{r1}	27	-5	1.0	80
x_{r2}	58	10	0.8	$-707+1481*e^{\frac{V_m+38}{95}}$
x_{A1}	26.5	-7.9	1.0	$31.8+175*e^{(-0.5\frac{V_m+44}{22.3})^2}$
x_{A2}	65	6.2	0.9	90
d_{Na}	47	-4.8	1.0	$-0.017*V_m+0.44$
f_{Na}	78	3	1.0	$-0.25*V_m+5.5$
m_{NSCC}	25	-20	1.0	$\frac{150}{1+e^{-\frac{V_m+58}{26}}}$

Vivaudou *et al.* (1988) and had a value of 3 ms. The weak voltage dependency of the inactivation time constant was described by fitting to experimental data from *Bufo Marinus* stomach (Vivaudou *et al.*, 1988) at -30 mV and -40mV and from guinea pig taenia coli (Yamamoto *et al.*, 1989) at more depolarised voltages.

Delayed Rectifier K^+ Channels

I_{Kr} refers to the typically TEA and 4-AP sensitive delayed rectifier potassium channels commonly expressed in a wide variety of excitable cells. The Nernst potential, E_K, was calculated using concentration data from Casteels (1981) and Knot *et al.* (1995).

$$I_{Kr} = G_{Kr} * x_{r1} * x_{r2} * (V_m - E_K) \tag{3.6}$$

Here G_{Kr} is the maximum conductance and its value (35 nS) was obtained from the slope of the predominantly linear I-V plot resulting from patch-clamp experiments in canine gastric smooth muscle (Sims, 1992a). In the absence of quantitative gastric data, the steady-state and time constant formulations for the Hodgkin-Huxley type activation (x_{r1}) and inactivation (x_{r2}) gating variables (see Table 3.1 and Figure 3.2) were taken from the colonic myocyte data of Koh *et al.* (1999) where two time constants were required to properly represent the potassium inactivation kinetics. Both activation and inactivation time constants were corrected for the temperature difference between experiments (21°C) and physiological conditions (37°C) by using a Q_{10} value of 1.5 (Tiwari & Sikdar, 1999).

A-type K^+ Channels

I_{KA} refers to the fast inactivating, Ca^{2+}-independent, TEA-insensitive, outward K^+ current that was first described in mollusc neurons (Amberg *et al.*, 2002; Farrugia, 1999; Hagiwara *et al.*, 1961).

$$I_{KA} = G_{KA} * x_{A1} * x_{A2} * (V_m - E_K) \tag{3.7}$$

The maximal conductance G_{KA} was fitted in the same manner as G_{Kr}. Here a value of 9 nS was obtained from experiments on guinea pig gastric myocytes (Noack *et al.*, 1992). The steady state equations for the activation (x_{A1}) and inactivation (x_{A2}) Hodgkin-Huxley type gating variables (see Table 3.1 and Figure 3.2) have been taken from data from murine gastric smooth muscle (Amberg *et al.*, 2002). Similar behaviour was also found in cells from newborn

rat ileum (Smirnov *et al.*, 1992) and are consistent with the notion that A-type channels are almost completely inactivated at -50mV. The activation time constants were fitted from the time-to-peak data from Amberg *et al.* (2002). The value of the inactivation time constant was chosen to be 90 ms in agreement with experimental data from murine gastric smooth muscle cells (Amberg *et al.*, 2002).

Large Conductance Ca^{2+}-activated K^+ Channels

Ca^{2+}-activated K^+ channels have traditionally been divided in three categories according to their large (BK), intermediate (IK) or small (SK) conductance. IK and SK have been implicated as mediators of inhibitory signals from the ENS for the generation of inhibitory junction potentials. In our description of the gastric SM cell, we therefore included only BK channels through the current I_{BK}.

$$I_{BK} = G_{BK} * P_o * (V_m - E_K) \tag{3.8}$$

Here, G_{BK} (45.7 nS) represents the maximal conductance (Barrett *et al.*, 1982). BK channels appeared not to inactivate therefore an inactivation gating variable has not been included. P_o represents the Ca^{2+}-dependent open probability that has been quantitatively described in the gastrointestinal tract by Carl *et al.* (1996).

$$P_o = \frac{1}{1 + e^{\frac{V_m}{k_{BK}} - h_{BK} log \frac{[Ca]_i}{Ca_{set}}}} \tag{3.9}$$

K_{BK} (-17 mV), Ca_{set} (0.001 mM) and h_{BK} (2) values were taken from the formulation proposed in the original paper for data from canine colonic myocytes.

Sodium Channels

The presence, genotype and function of sodium channels in the gastrointestinal tract have been the subject of some debate. The variety of IC_{50} values for the best known sodium channel blocker, TTX, underlies a probable variety of isoforms expressed throughout the gastrointestinal tract (Sanders *et al.*, 2006b). Sodium currents have been reported in guinea-pig gastric fundus (Muraki *et al.*, 1991) and, more recently, in human jejunal smooth muscle (Holm *et al.*, 2002). It has also been shown that TTX (up to 1 μM) does not affect the shape, amplitude and propagation of slow waves and smooth muscle depolarisations in the guinea-pig gastric antrum (Huang *et al.*, 1999). We have therefore chosen to include the relatively TTX-resistant sodium channel that was described by Holm *et al.* (2002). This channel was unaffected by presence of 100 nM of TTX and its amplitude was reduced by only 30% in the presence of 1 μM TTX.

$$I_{Na} = G_{Na} * d_{Na} * f_{na} * (V_m - E_{Na}) \tag{3.10}$$

Here, G_{Na} represents the maximal Na^+ conductance and its value (3 nS) was chosen to reproduce the experimental observation that a peak current of 14 pA was elicited when the voltage was stepped from a holding potential of -70 mV to -20 mV. d_{Na} and f_{Na} represent the Hodgkin-Huxley type gating variables for activation and inactivation respectively. Their steady-state curves were

taken from Holm *et al.* (2002). The equation for the activation time constant was obtained by fitting data at -60 mV and 0 mV extrapolated from time-to-peak measurements. Similarly, the inactivation time constant was fitted to data at -50 mV and -10 mV. Model parameters were adjusted to 37°C using a Q10 of 2.45, a value obtained by comparison of inactivation time constants at 10°C and 21°C measured in freshly dispersed cells from the rat gastric fundus (Muraki *et al.*, 1991).

Non-Selective Cationic Channels

Non-selective cationic channels (NSCC) have been described in guinea-pig (Kang *et al.*, 2001) and canine (Sims, 1992b; Vogalis & Sanders, 1990) gastric smooth muscle as well as in the guinea-pig ileum (Inoue & Isenberg, 1990b,a) and murine colon (Koh *et al.*, 2001).

$$I_{NSCC} = G_{NSCC} * m_{NSCC} * r_{lig} * h_{NSCC-Ca} * (V_m - E_{NSCC}) \qquad (3.11)$$

G_{NSCC} represents the maximal conductance and its value (50 nS) was chosen to yield an I-V profile that matches the one experimentally recorded in canine gastric smooth muscle cells under voltage clamp conditions where voltage was held at -60 mV and then brought from -120 mV to -10 mV with ramp commands (Sims, 1992b). m_{NSCC} represents the voltage dependence of the activation kinetics. Its steady state curve was also obtained from canine gastric data (Sims, 1992b), however, in the absence of a detailed kinetic description from canine gastric smooth muscle, the time constant was fitted to data from the guinea-pig ileum (Inoue & Isenberg, 1990a). r_{lig} takes into

account the observation that NSCC are activated experimentally by the presence of particular ligands (muscarinic stimulation). One such formulation can be obtained from isolated smooth muscle cells from the guinea-pig ileum (Inoue & Isenberg, 1990a). The authors found that the effect of acetylcholine on the cellular response could be described with the following Michaelis-Menten equation

$$r_{lig} = \frac{1}{1 + \frac{K_m}{[Ach]}} \tag{3.12}$$

where K_m (10 μM) is the half maximal value. The variable $h_{NSCC-Ca}$ was introduced in order to describe the facilitation effect that intracellular Ca^{2+} has on I_{NSCC} and was formulated as shown in Equation 3.13.

$$h_{NSCC-Ca} = \frac{1}{1 + (\frac{[Ca^{2+}]_i}{K_{CaNSCC}})^{n_{Ca}}} \tag{3.13}$$

The values of the parameters K_{CaNSCC} (200 nM) and n_{Ca} (-4) were taken from the guinea-pig ileum (Inoue & Isenberg, 1990b) where values of 200 nM and 1 μM were obtained for half-maximal and sub-maximal Ca^{2+} concentrations respectively. The value of the reversal potential E_{NSCC} (-28 mV) was taken from canine pyloric smooth muscle data (Vogalis & Sanders, 1990).

Background K^+ conductance

A background potassium conductance was included and described by

$$I_{Kb} = G_{Kb} * (V_m - E_K) \tag{3.14}$$

The value of the conductance G_{Kb} (0.0014 nS) was chosen in order to yield a stable resting membrane potential equal to that observed experimentally in canine gastric smooth muscle (Ward *et al.*, 2004).

Calcium Homeostasis

Control of the intracellular Ca^{2+} concentration is of primary importance as Ca^{2+} mediates a variety of processes including the regulation of several types of ion channels. The influx of Ca^{2+} from the extracellular space is mediated by plasma membrane Ca^{2+} channels. Ionic exchangers and intracellular stores such as the sarcoplasmic reticulum (SR) also play a significant role in maintaining intracellular Ca^{2+} homeostasis. The SR was found to be co-localised with Na^{+} /Ca^{2+} exchangers (Moore *et al.*, 1993) and spatially closely associated with the plasma membrane (Sanders, 2001). In the absence of contraction, Ca^{2+} influx through the L-type membrane channels does not appear to elicit a significant Ca^{2+} release from the SR during slow wave activity in SM cells (Bradley *et al.*, 2002; Kim *et al.*, 1997; Wu & Fry, 2001). The SR therefore adopts primarily a storage role (with ryanodine and IP3-sensitive stores) (Bradley *et al.*, 2002; White & McGeown, 2000). Moreover, it was observed that the rate of Ca^{2+} uptake is voltage independent and that Na^{+}/Ca^{2+} exchanger activity does not contribute directly to the rate of decline of intracellular Ca^{2+} (Bradley *et al.*, 2002). Plasma membrane Ca^{2+} pumps (PMCA) (Hurwitz *et al.*, 1973; Monteith *et al.*, 1996) and mitochondrial uptake (Sanders, 2001) have also been indicated as homeostatic mechanisms for cytoplasmic Ca^{2+}.

Due to the incomplete nature of current experimental data and our desire to describe slow waves in SM cells (in absence of contraction) in a computationally efficient way, we have implemented a phenomenological model of Ca^{2+} uptake and extrusion. By grouping together the aforementioned components, Equation 3.15 was derived to describe the depletion of free Ca^{2+} ions from the intracellular space.

$$I_{CaExt} = 0.317 * [Ca^{2+}]_i^{1.34} \tag{3.15}$$

I_{CaExt} (in mM/ms) therefore represents the total rate of Ca^{2+} uptake by the sarcoplasmic reticulum, mitochondria and extrusion via PMCA. The parameters of Equation 3.15 were chosen to ensure Ca^{2+} homeostasis and that a physiological level of $[Ca]_i$ was achieved during each slow wave in the SM cell.

Electrical Stimulus from ICC

The stimulus from the ICC network was modeled as an injected current whose value was obtained by dividing experimental (voltage) recordings of ICC from guinea pig gastric antrum by the value of the coupling resistance between ICC and smooth muscle. A detailed, biophysical model of an ICC will be discussed later in Chapter 4. For simplicity, here we use the following phenomenological equation that reproduces an ICC slow wave profile to stimulate the smooth muscle model.

$$I_{stim} = \begin{cases} G_{couple} * \Delta V_{ICC} & \text{if } t < t_{peak} \\ G_{couple} * \Delta V_{ICC} * \frac{1}{1+e^{\frac{t-8000}{1000}}} & \text{if } t_{peak} \leq t < t_{plateau} \\ I_{stim|t=t_{plateau}} * \frac{1.3}{1+e^{\frac{t-8000}{150}}} & \text{if } t_{plateau} \leq t < t_{SW} \end{cases} \tag{3.16}$$

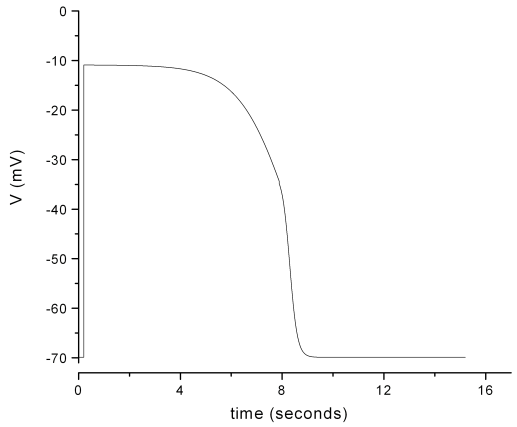

Figure 3.4: Slow wave profile of an ICC designed to reproduce experimental traces recorded from the guinea-pig gastric antrum. The voltage of this slow wave was divided by a coupling resistance and injected into the smooth muscle cell.

We chose an ICC profile with an amplitude (ΔV_{ICC}) of 59 mV (Sanders *et al.*, 2006b) and a duration of just under 10 seconds (Cousins *et al.*, 2003; Forrest *et al.*, 2006; Hirst & Edwards, 2004; Sanders *et al.*, 2006a) by setting t_{peak}, $t_{plateau}$ and t_{SW} to 98 ms, 7.58 s and 10 s respectively. The upstroke phase was characterised with a maximum gradient of 600 mV/s to reproduce experimental observations in canine gastric smooth muscle (Ward *et al.*, 2004). The coupling between ICC and smooth muscle was studied by Cousins *et al.* (2003) with experiments on guinea pig gastric antrum tissue samples. The value of the overall bulk coupling resistance between ICC and the nearby muscle layer (longitudinal and circular) was found to be 306 nS, representing the mean value of four measurements ranging from 157 nS to 877 nS. This value should be interpreted as a bulk tissue conductance and not the coupling conductance between a single ICC and a single SM cell. Indeed using this as a coupling

conductance produced SM membrane potentials that were significantly higher than the normal physiological range. It was therefore necessary to adopt a much smaller value (G_{couple}=1.3 nS) for the cell-cell coupling conductance to restrict the stimulus current to a more realistic amplitude. Figure 3.4 shows the ICC slow wave profile used to excite the SM cell model in this chapter.

3.3 Model Predictions and Validation

The results from a simulation showing a series of slow waves in SM cells in the absence of muscarinic stimulation ([ACh] = 10 nM) are shown in Figure 3.5. Experimentally recorded SM slow waves from a canine antral smooth muscle strip are also displayed (Ward *et al.*, 2004). The shape of the simulated SM slow waves resembles those published in the literature (Sanders *et al.*, 2006b; Ward *et al.*, 2004) and the typical phases (upstroke, notch, plateau and repolarisation) can be clearly identified. The amplitude of the SM slow waves was slightly more than 30 mV, consistent with experimental findings (Huang *et al.*, 1999; Huizinga, 2001; Sanders *et al.*, 2006a; Suzuki, 2000) and the membrane potential repolarisation was 98% complete after 10 seconds in agreement with published experimental data (Huang *et al.*, 1999; Sanders *et al.*, 2006a). Figure 3.6 shows the time dependency of several of the main model currents. In experiments on canine gastric smooth muscle cells, slow waves in SM cells caused an increase in the intracellular Ca^{2+} concentration of approximately 200 nM (Vogalis *et al.*, 1991). Other reports on different smooth muscles found an increase on the order of 400 nM (reviewed in Carl *et al.* (1996)). Our simulation results predict a rise in intracellular Ca^{2+}, as a

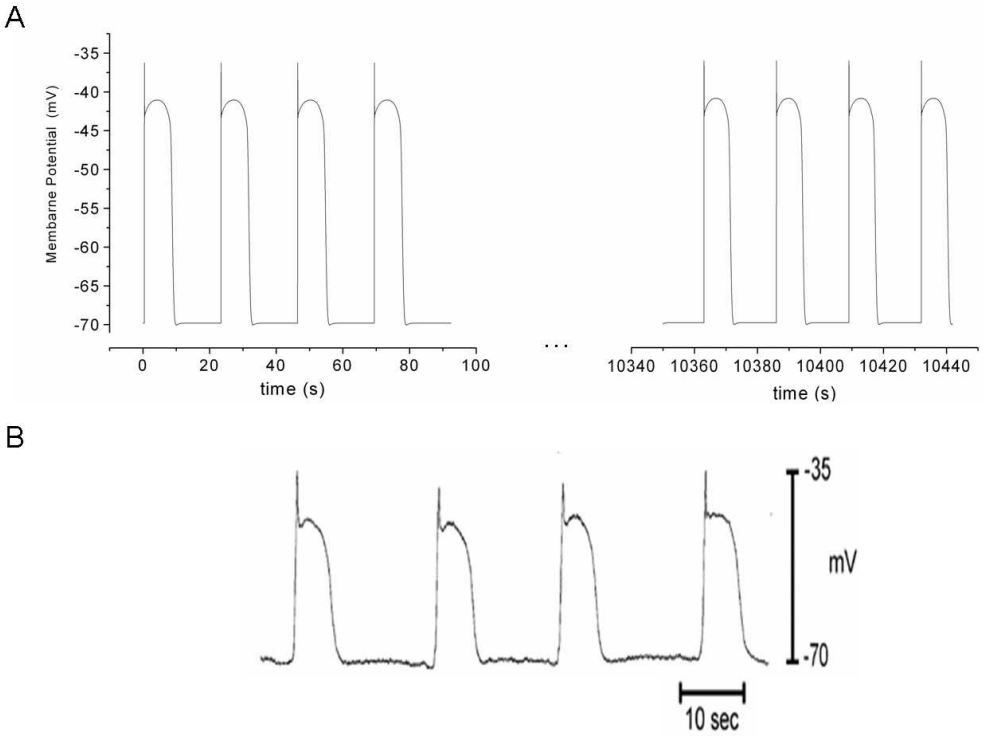

Figure 3.5: Simulation results: (A) Simulated slow waves in a SM cell at the beginning of the simulation and after 17 minutes of activity at 2.6 cycles per minute (cpm). (B) Experimental recording obtained from a canine gastric smooth muscle strip; reproduced from Ward *et al.* (2004).

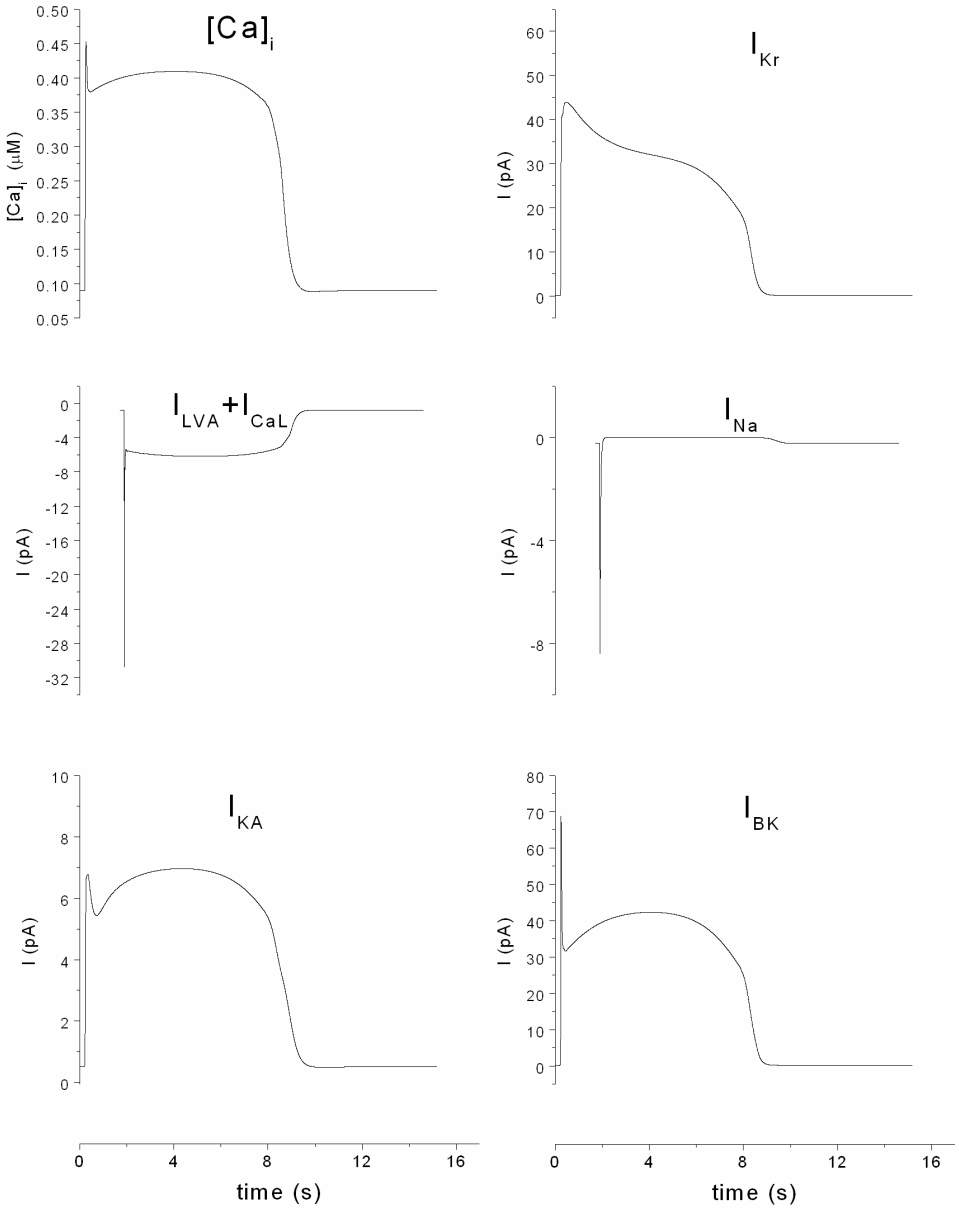

Figure 3.6: The main currents in the model are displayed over time for a single SM slow wave along with the profile of the intracellular calcium transient (top left panel).

result of Ca^{2+} influx through ion channels and intracellular uptake, of 300 nM in line with these experimental observations.

3.3.1 Effect of Potassium Channel Blockers

A-type potassium channels have been implicated in setting the cellular resting membrane potential, however their contribution to the plateau phase of a SM slow wave was found to be limited. In experiments on murine gastric smooth muscle cells the presence of flecainide (a known A-type channel blocker) in concentrations near its IC_{50} raised the resting membrane potential by 8.1% (Amberg *et al.*, 2002). Here we simulated the presence of flecainide near its IC_{50} by halving the A-type potassium conductance. The results this simulation show a 5.7% rise in the resting membrane potential but no significance difference in the plateau potential (Figure 3.7A).

The effect of another common potassium channel inhibitor 4-aminopyridine (4-AP) on the SM slow waves was studied in feline gastric (Boev *et al.*, 1985), canine colonic (Thornbury *et al.*, 1992) and guinea-pig airway smooth muscle (Isaac *et al.*, 1996). 4-AP in a concentration of 5mM is a known blocker of both A-type and delayed rectifier potassium conductances (reviewed in Sanders *et al.* (2006b)) and therefore its presence was simulated by setting both the A-type and delayed rectifier conductances to zero. The resulting SM slow waves (shown in Figure 3.7B) are in agreement with the 10-20 mV depolarisation in the resting potential observed experimentally (Isaac *et al.*, 1996). Moreover, the simulated plateau potential was raised by 5 mV, which is consistent with the notion that the presence of 4-AP enhances contractility and the ap-

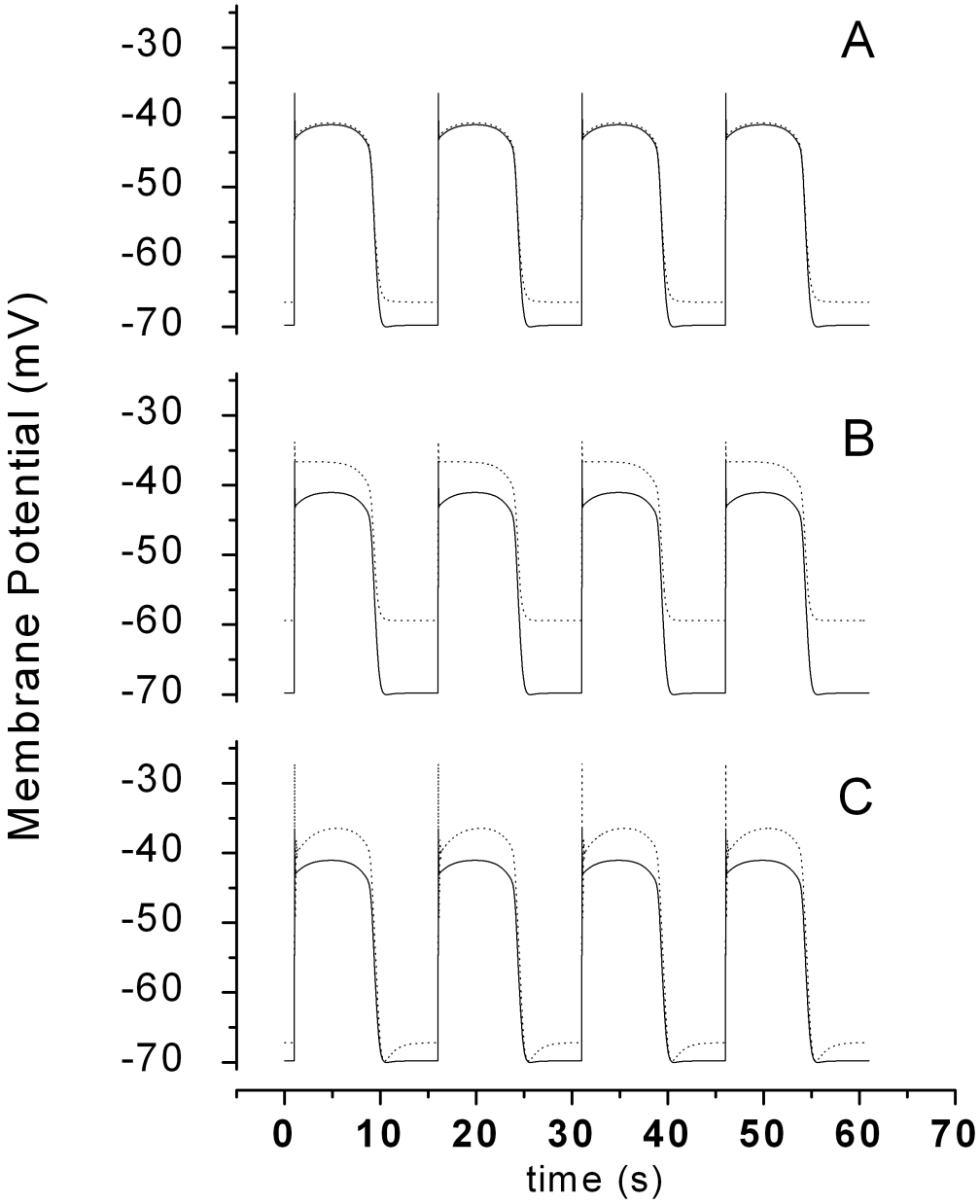

Figure 3.7: Effects of channel blockers on the SM slow wave profile: (A) Simulated presence of flecainide (30 μM) causing blockage of 50% of the A-type potassium conductance (dotted line) compared to control conditions (solid line). (B) Simulated presence of 4-AP (5 mM) with blockage of A-type and delayed rectifier potassium currents (dotted line) compared to control conditions (solid line). (C) Simulated presence of TPeA (20 M) with blockage of BK channels (dotted line) compared to control conditions (solid line).

pearance of spike potentials observed in guinea-pig gastric antrum due to the increased level of the plateau potential (Boev *et al.*, 1985). Experiments on intact smooth muscle preparations from canine colonic myocytes revealed that the addition of a potent BK channel blocker such as tetrapentylammonium (TPeA) extracellularly in concentrations of 20 μM (about ten times its K_d value) caused a rise of 7 mV in the plateau phase of the SM slow waves and eventually locked the membrane potential at the plateau level as the repolarisation failed to occur (Carl *et al.*, 1993). Here we simulated the presence of TPeA by shutting down the BK conductance (G_{BK}=0). The result (Figure 3.7C) was a rise in the plateau by 4.6 mV in general agreement with the experimental observation (Carl *et al.*, 1993). In our simulations, however, the membrane did not fail to repolarise as observed experimentally; a possible explanation for this discrepancy may be the effect of TPeA on the ICC in the intact muscle preparation as this was not incorporated here.

3.3.2 Effect of Intracellular Ca^{2+} on BK and Ca^{2+} Channels

During a SM slow wave the Ca^{2+} concentration in the cytoplasm rises as a result of the ionic influx through voltage gated Ca^{2+} channels. If the amount reaches a certain threshold spike potentials can be observed in the antral and pyloric regions and a contractile response occurs (Sanders *et al.*, 2006b). The regulatory mechanisms of the plateau phase of the SM slow waves have been attributed to the interplay between Ca^{2+} and potassium channels. The presence of Ca^{2+}-activated potassium channels in gastric muscle is expected to

cause decreased plateau potentials in response to an increased (depolarising) Ca^{2+} current through Ca^{2+} channels. Here the effects of an altered intracellular Ca^{2+} transient were simulated by modifying the inhibitory effect that Ca^{2+} ions have on L-type Ca^{2+} channels i.e. releasing or tightening the self regulatory mechanism of L-type Ca^{2+} channels through the variable f_{Ca}. Partial inhibition of the regulatory mechanism was simulated by shifting the steady state curve of the variable f_{Ca} (half inactivation value shifted to 401.4 nM). By partially and completely inhibiting this negative feedback mechanism (see Figure 3.8 for details), the plateau Ca^{2+} level was predicted to be 500 nM and 630 nM respectively. This triggered an increased BK current (around 53 pA and 70 pA respectively) which, despite an increase in the inward Ca^{2+} current, caused a shift in the plateau membrane potential in the polarised direction. These results appear to support the view that during activation in phasic muscles, Ca^{2+}-activated BK channels may act as intracellular Ca^{2+} sensors and limit the degree of depolarisation and contraction (Carl *et al.*, 1996).

3.4 Summary of the Smooth Muscle Model

The main objective of this chapter was to develop and validate a model of a gastric smooth muscle cellular electrophysiology. Due to the multitude of ion channel species expressed in such cells, the present description includes only those components that were deemed to significantly contribute to the cellular electrical response to a stimulation coming from the ICC network during basal electrical activity in the absence of contraction-associated spikes). For those ionic currents whose activation is mediated by the presence of, for example,

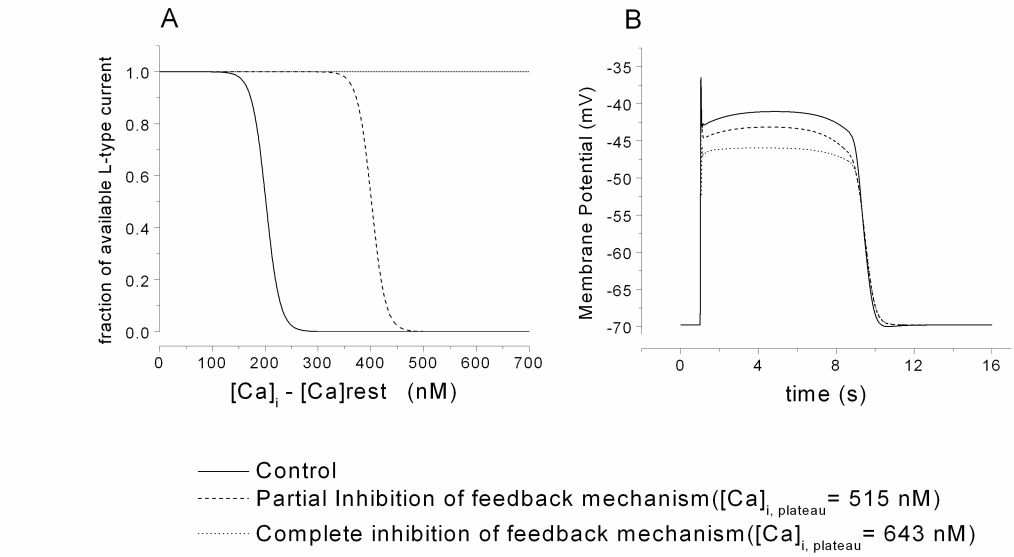

Figure 3.8: Comparison between the normal situation and the case of partial and complete inhibition of the $[Ca^{2+}]_i$ influence on L-type Ca^{2+} channels. (A): different curves used for the variable f_{Ca}. h_{Ca}=201.4 nM for the control case, and 401.4 nM for the partially inhibited case. s_{Ca}= 13.1 in both cases. f_{ca}=1 when the feedback is completely inhibited. (B): influence of the feedback mechanism on the SM slow waves.

particular ligands, we have chosen to either group the channel species into one component or to exclude them from the present description. The main reason for these simplifications is a lack of quantitative experimental data. These simplifications do, however, mean that only a relatively small number of equations are needed to describe the system making it suitable for large scale multi-cellular studies.

The trade-off between opposing needs of simplicity for computational efficiency and complexity for a complete description of the physiological reality resulted in a total of 8 ionic currents, 4 of which are carried by potassium ions. The variety of potassium channels that has been identified in GI smooth muscle to date posed a challenge in determining which ones to include as major players in gastric SM slow waves. We grouped the so-called Two-Pore K^+ (families of TREK and TASK channels) and the ether-a-go-go (ERG) channels to the background potassium current, that is believed to influence the resting membrane potential without characterising their response to particular stimuli. ATP-dependent potassium channels (K_{ATP}) were not included but would arguably be required to describe the response of a cell to metabolic stimuli (such as a drop in the ATP concentration below 1 mM) or ischemic conditions.

The presence of chloride currents in gastrointestinal smooth muscle has not yet been fully demonstrated. Some pharmacological studies seem to imply the presence of such currents, however the non-specificity of the drugs used in these studies together with the lack of a genotypic identification of such channels leaves the topic controversial. For this reason we decided not to include a Ca^{2+}-

activated chloride conductance. A volume-sensitive chloride conductance has also been reported in smooth muscle cells from guinea-pig stomach, however, since in the present model we are not considering any mechanical deformations, this conductance has not been included.

Due to the fact that sodium and potassium ions generally do not possess the same ability to act as second messengers for important intracellular regulatory mechanisms as Ca^{2+} does, only the Ca^{2+} ion concentration was tracked over time whereas the K^+ and Na^+ concentrations were considered invariant. Quantitative data regarding the kinetics and regulatory aspects of intracellular Ca^{2+} ions dynamics are difficult to obtain and, as a consequence, the available literature is incomplete. Although it is known that intracellular Ca^{2+} uptake is dependent on the combined activity of SR, mitochondria and PMCA, it is not known how the contribution of each uptake pathway affects the overall Ca^{2+} dynamics in the cytoplasm. Owing to these limitations, we summarised the intracellular Ca^{2+} uptake with one equation (Equation 3.15) assuming that all intracellular uptake pathways depend only on the intracellular Ca^{2+} concentration. Such simplifications can be addressed in the future when sufficient experimental data becomes available.

Over the past few decades, patch clamp experiments have been performed on smooth muscle cells from different regions of the GI tract and from several different animal species. Inter-species differences in the electrophysiological properties of muscular tissues are widely reported. Moreover, within the same species, prominent regional differences between different tissues in the GI tract in terms of SM slow wave shape, frequency and duration have been noted

and attributed to different underlying cellular mechanisms. We found that there was not enough experimental data available to construct a complete model of a gastric SM cell from a single animal species. We have adopted experimental data from canine gastric smooth muscle cells whenever possible and when such data were not available, we preferentially included data from gastric smooth muscle cells from other species, and finally smooth muscle data from other GI regions. For example, steady-state parameters in Equation 3.7 were taken from experiments on murine gastric myocytes, half-activation parameters in Equation 3.13 were adopted from guinea-pig ileum experiments while time-dependent parameters in Equation 3.6 were taken from murine colonic myocytes. In the study of the electrophysiology of a specific animal species, these discrepancies might potentially introduce some inaccuracies that may only be negated by the availability of a full set of experimental data from the species under consideration.

While the resulting description is predominantly a description of a canine gastric SM cell, the limitations inherent in adopting data from other GI smooth muscle cells should not be ignored when interpreting model results, in particular where the goal is to relate an observed behaviour to the underlying physiology. Nevertheless, the simulated SM slow wave traces share many common features with those recorded experimentally from canine gastric smooth muscle preparations (Figure 3.5). Simulated intracellular Ca^{2+} dynamics also resembled experimental measurements from canine gastric preparations. In order to further validate the model, we simulated the presence of known channel blockers or inhibitors by accordingly modifying the of that specific channel

and checked whether the predicted SM slow wave outcome matched the experimental SM slow wave recording in presence of that specific blocker (Figure 3.7). Results of such simulations are also in agreement with experimental data.

Although the results presented in this chapter are encouraging, much has to be done in order to establish electrophysiological models of the stomach as a reliable tool for investigating the pathophysiological aspects of this tissue in the same way as is done for the heart. In this context, the development of a complementary gastric ICC model and subsequent incorporation into multicellular tissue-level simulations will be discussed in the next chapters.

Chapter 4

Gastric ICC Model

4.1 Introduction

In this chapter we present a mathematical description of single cell gastric ICC electrophysiology. Section 4.2 details the main intracellular processes that are currently believed to provide the pacemaker signal as well as the membrane ion channels that have been identified and functionally characterised in ICC. In Section 4.3 the validation of the model in control and pharmacologically altered conditions will be discussed.

4.2 Structure of the Model

4.2.1 Overview of the Model

The model is based on a classical Hodgkin-Huxley approach where the cell membrane is described as an equivalent electrical circuit consisting of a ca-

pacitance connected in parallel with a number of variable conductances representing the different pathways for the movement of charged ions. The time dependence of the membrane potential is governed by

$$C_m \frac{dV_m}{dt} = -I_{ion} \tag{4.1}$$

where V_m (in mV) represents the transmembrane potential, C_m is the cell capacitance and its value was fixed at 25 pF (Kim *et al.*, 2002). I_{ion} (in pA) represents the sum of the ionic currents crossing the cell membrane. Equation 4.1 is the same as Equation 1.1 where the I_{stim} term equals zero. The reason for this simplification is due to the fact that ICC are capable of generating slow waves without any external stimulus. Figure 4.1 presents a schematic overview of the model where the four main intracellular compartments (bulk cytoplasm, mitochondria, endoplasmic reticulum (ER) and submembrane space (SS)) are displayed together with the ion channels and transport mechanisms included in the plasma membrane. The fraction of volume occupied by the mitochondria was estimated at 13% of the total intracellular space for the following reasons: firstly, it was noted by several authors that ICC display particularly abundant mitochondria (Komuro, 1999) and it was therefore deemed reasonable to choose a value higher than estimates given for other cell types (e.g 5% on pancreatic β-cells (Fall & Keizer, 2001)). Secondly, a value of 13% is compatible with confocal images obtained in the presence of MitoTracker Green FM on cultured murine jejunal ICC when compared with whole cell c-kit staining of the same cell (Ward *et al.*, 2000). The proportion of the intracellular volume occupied by the ER was set to 10%, similar to estimates made by other investi-

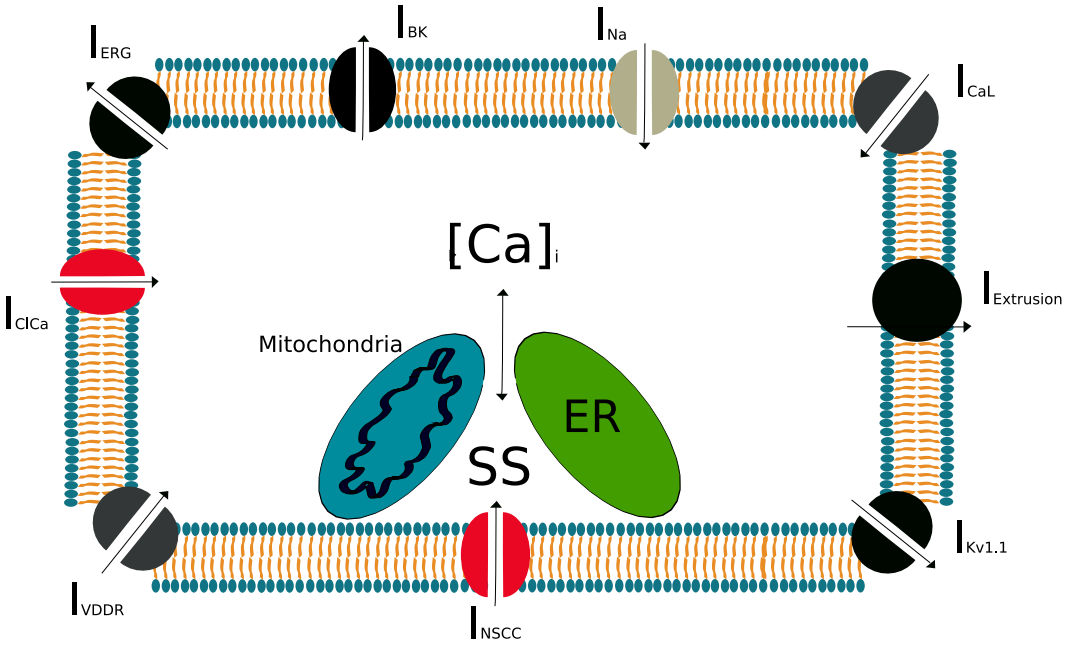

Figure 4.1: Schematic view of the ICC model. The intracellular space is divided in four compartments: cytoplasm, mitochondria, endoplasmic reticulum (ER) and submembrane space (SS). All the membrane ion channels and transport mechanisms included in the model are depicted. Details of the SS are given in Figure 4.2. Please note that endoplasmic reticulum is used in this model instead of sarcoplasmic reticulum because ICC are not generally classified as muscle cells.

gators on intestinal ICC (Youm *et al.*, 2006), pancreatic β-cells (Fall & Keizer, 2001) and cardiac myocytes (Jafri & Gillo, 1994). The SS was defined to be a subcellular compartment limited by the plasma membrane, mitochondria and ER. It has been suggested that Ca^{2+} shuttling between the mitochondria and ER within this enclosed space is responsible for the pacemaking capabilities of ICC (Sanders *et al.*, 2006a). Quantification of the volume occupied by the SS is made difficult because of the lack of specific morphological information about its geometry. Sanders *et al.* (2006a) suggested that its volume should be 'very small'. Given a lack of quantitative information, a value 0.1% of the cell volume was chosen based on its ability to able to yield appropriate physiological Ca^{2+} concentrations. The bulk cytoplasm, defined as the space available for ionic diffusion, was assumed to occupy 70% of the cellular volume. This value is slightly higher than that used by Fall & Keizer (2001) (50%), due to experimental observations on ICC that have shown a particularly 'electron-dense' cytoplasm (Komuro, 1999).

4.2.2 Pacemaker Unit

The intracellular mechanisms responsible for the pacemaker activity in gastrointestinal ICC have been object of controversy. Although many intracellular players have been implicated in the generation of the slow waves, several experimental observations appear to agree on identifying the interplay between mitochondria and ER in Ca^{2+} handling as the main process involved in initiating the electrical activity in gastrointestinal ICC (Sanders *et al.*, 2006a; Takaki, 2003; Ward *et al.*, 2000). Based on these observations, comprehensive theories

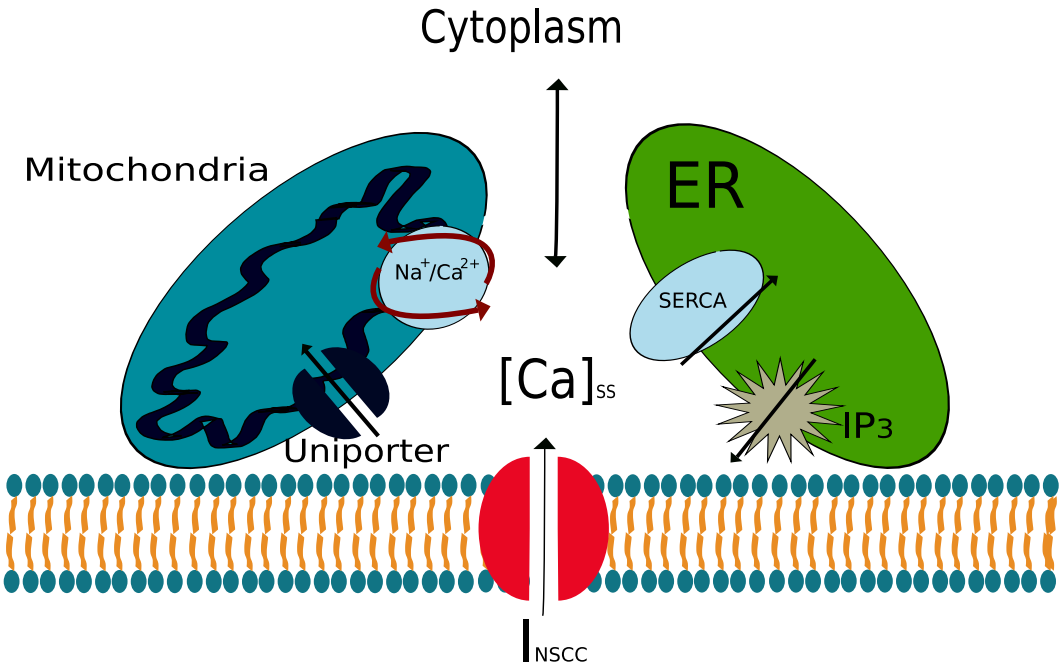

Figure 4.2: Schematic view of the submembrane space (SS). The Ca^{2+} concentration in the SS is the result of the interplay between mitochondrial Ca^{2+} handling proteins (Uniporter and Na^+/Ca^{2+} exchanger), processes involving the ER (uptake through SERCA pump and IP3-mediated release) and a small leakage between the SS and the cytoplasm. In the figure, red arrows represent Ca^{2+} fluxes, whereas blue arrows represent monovalent cationic fluxes (Na^+or K^+).

have recently been proposed (Sanders *et al.*, 2006a; Kito & Suzuki, 2003). The initiating event is proposed to be a Ca^{2+} release from IP3-operated stores in the ER into an intracellular subspace (the SS) formed by the ER, mitochondria and plasma membrane. Upon the subsequent rise in Ca^{2+} concentration in this subspace, the Ca^{2+} uniporter on the mitochondrial membrane is gated open and Ca^{2+} ions flow into the mitochondria down the steep electrochemical gradient. This is thought to remove a larger number of Ca^{2+} ions from the subspace than had previously entered from the ER causing a temporary drop in the SS Ca^{2+}concentration. A recently identified Ca^{2+} -inhibited non

specific cationic conductance (NSCC) (Koh *et al.*, 2002) responds to the decrease in SS Ca^{2+} by opening the channel and allowing a cationic influx that depolarises the plasma membrane. These depolarisations are referred to as unitary potentials and are thought to be the initiating electrical events that, in turn, activate voltage-gated Ca^{2+} channels and subsequently all of the other ion channels on the plasma membrane responsible for the observed slow wave profile. A number of mathematical models describing intracellular Ca^{2+} dynamics have appeared in literature in the past few decades (Marhl *et al.*, 2000; Roux *et al.*, 2006; Schuster *et al.*, 2002) each focusing on particular aspects of the ubiquitous role of Ca^{2+} ions in the cytoplasm. After an extensive search, the model developed by Fall & Keizer (Fall & Keizer, 2001)(F&K) was chosen to represent the behaviour of the intracellular Ca^{2+} handling proteins for the following reasons. Firstly, it describes the activity of mitochondrial uniporter, mitochondrial Na^{+}/Ca^{2+} exchanger, SERCA pump and IP3-mediated Ca^{2+} release from the ER, all of which appear to be included in the pacemaker mechanism of gastric ICC (Sanders *et al.*, 2006a). These four Ca^{2+} proteins combine to determine the Ca^{2+} concentration in the SS ($[Ca^{2+}]_{SS}$) as follows

$$\frac{d[Ca^{2+}]_{SS}}{dt} = -J_{UNI} + J_{NaCa} - J_{SERCA} + J_{ER} - J_{leak} \tag{4.2}$$

where the J terms are Ca^{2+} fluxes. J_{leak} is the leakage of Ca^{2+} ion between SS and cytoplasm. Secondly, the frequency of the Ca^{2+} cycling predicted by the F&K model is close to the typical frequency of the generation of the slow wave in the stomach (3 cpm) (Sanders & Publicover, 1995). Finally, the F&K model explicitly describes the dynamics of the mitochondrial membrane potential as

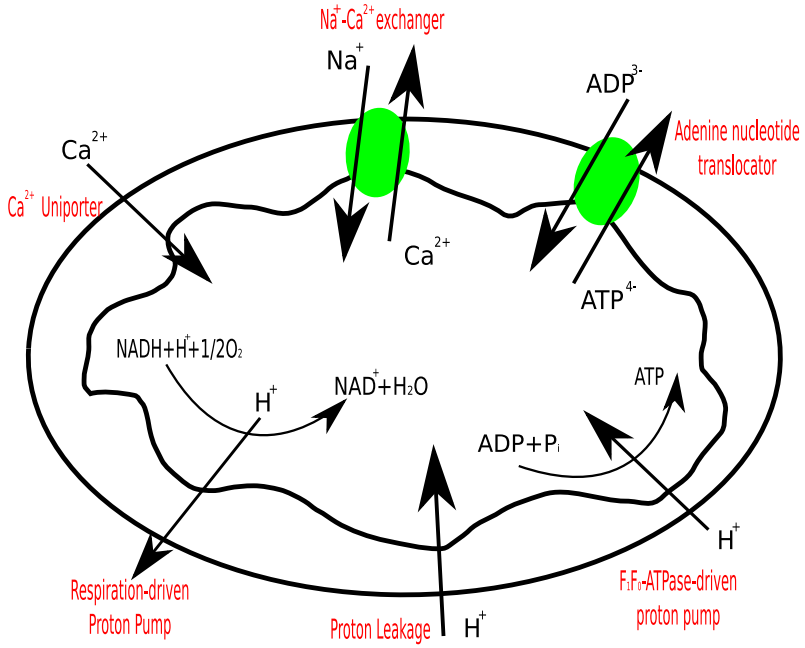

Figure 4.3: Schematic view of the mitochondrial model of Magnus & Keizer (1997) that was incorporated into the ICC model.

this has been shown to play a crucial role in the pacemaker activity of ICC in the guinea-pig stomach (Ward *et al.*, 2000). Briefly, the F&K model describes the behaviour of the mitochondrial membrane potential in terms of the main ionic transport proteins on the mitochondrial membrane, including the F0F1 ATPase proton pump, the respiration driven proton pump, the adenine nucleotide translocator and the aforementioned Ca^{2+} handling proteins (Figure 4.3). The F&K model is itself largely based on previously descriptions of intracellular dynamics (Magnus & Keizer, 1997, 1998a,b) and interested reader may find details as well as validations of these models in the referenced publications. The kinetics of the F&K model were left unaltered with the exception of the parameters describing the volume fractions of each subspace which were

Table 4.1: Ionic concentrations in the intracellular and extracellular space. The ionic concentration in the extracellular space are the same as for the SM model (Chapter 3).

Ion	Intracellular (mM)	Extracellular (mM)
Na^+	30	137
K^+	101	5.9
Ca^{2+}	Equation 4.19	2.5
Cl^-	88	134

modified to include the SS.

4.2.3 Membrane Ion Channels

Each of the major membrane ionic conductances that have been experimentally described in ICC (shown in Figure 4.1) were included in the I_{ion} term of Equation 4.1

$$I_{ion} = I_{CaL} + I_{VDDR} + I_{Na} + I_{ERG} + I_{Kv11} + I_{BK} + I_{ClCa} + I_{NSCC} + I_{bK} + \\ + 2 * F * V_{cyto} * J_{Ca-EXT} \quad (4.3)$$

Details of these conductances are given below. The calculation of the Nernst potential for each of the ion channels was based on the ionic concentrations of Table 4.1.

Calcium Channels

At least two types of Ca^{2+} channel have been identified in ICC. One is a DHP-resistant conductance that was resolved with patch clamp experiments on ICC isolated from the murine small intestine (Kim *et al.*, 2002), whereas the

Table 4.2: Parameters of the Hodgkin-Huxley type voltage dependent gating variables. Steady state equation for variable x is given by $x_\infty = \frac{A}{1+e^{\frac{V+V_h}{h}}} + (1.0 - A)$ and τ is the time constant.

Variable name	V_h(mV)	h (mV)	A	τ(ms)
d_{VDDR}	26	-6	1.0	6
f_{VDDR}	66	6	1.0	40
d_{CaL}	17	-4.3	1.0	1
f_{CaL}	43	8.9	1.0	86
d_{kv11}	25	-7.7	1.0	5
f_{kv11}	44.8	4.4	0.5	5
d_{ERG}	20	-1.8	0.8	3
d_{Na}	47	-4.8	1.0	3
f_{Na}	78	8	1.0	1.6

other one has been molecularly classified as an L-type Ca^{2+} channel (Cho & Daniel, 2005). We therefore include two equations, one for each Ca^{2+} channel conductance:

$$I_{VDDR} = G_{VDDR} * d_{VDDR} * f_{VDDR} * (V_m - E_{Ca}) \tag{4.4}$$

$$I_{CaL} = G_{CaL} * d_{CaL} * f_{CaL} * f_{Ca} * (V_m - E_{Ca}) \tag{4.5}$$

where I_{VDDR} and I_{CaL} represent the ionic currents flowing through the DHP-resistant and L-type channels respectively. E_{Ca} is the Nernst potential for Ca^{2+} ions while d_{VDDR} and f_{VDDR} represent activation and inactivation gating variables. Their steady state equations (see Table 4.2 and Figure 4.4) have been taken directly from experimental values and their time constants have been chosen to replicate the results from voltage clamp experiments (Kim *et al.*, 2002). In absence of direct measurements of L-type Ca^{2+} currents

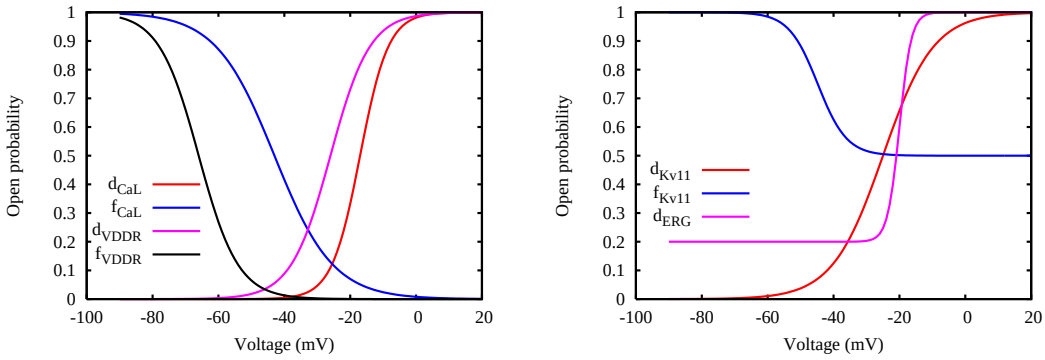

Figure 4.4: Steady states curves for voltage dependent gating variables in ICC. Ca^{2+} channel gates are shown on the left figure, K^+ channel gating variable are shown on the right figure.

from isolated gastric ICC, a description of L-type Ca^{2+} channels in gastric smooth muscle was adopted (Corrias & Buist, 2007). Again the d_{CaL} and f_{CaL} represent voltage dependent activation and inactivation gating variables (see Table 4.2) while f_{Ca} represents the Ca^{2+}-dependent inactivation.

$$f_{Ca\infty} = 1.0 - \frac{1.0}{1 + e^{-\frac{\Delta[Ca]_i - h_{Ca}}{s_{Ca}}}} \tag{4.6}$$

where $\Delta[Ca]_i$ is the variation of cytoplasmic concentration (in nM) from the value in resting conditions, while h_{Ca} (201.4 nM) and s_{Ca} (13.1 nM) are the half concentration and slope factor respectively. The time constant for this inactivation was chosen to be 2 ms (Corrias & Buist, 2007). The values of the maximal conductances G_{VDDR} and G_{CaL} (3 nS and 2 nS respectively) were chosen in order to reproduce the voltage clamp experiments of Kim *et al.* (2002) (see Figure 4.5).

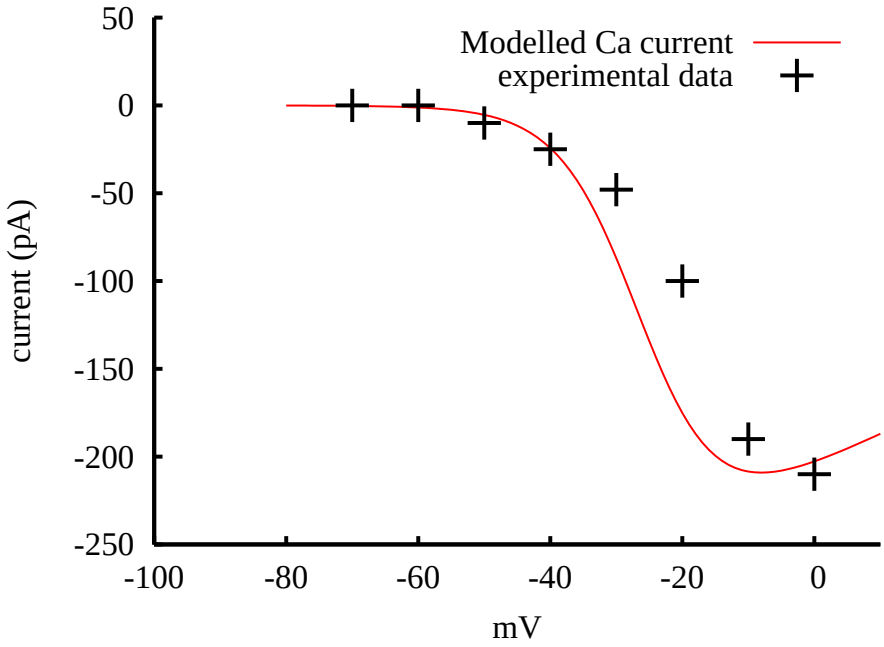

Figure 4.5: I-V plot in the physiological range for Ca^{2+} currents (I_{L-type}+I_{VDDR}): the black crosses are manually extrapolated from Figure 3E of Kim *et al.* (2002) while the red line is obtained by applying to Equations 4.4 and 4.5 (with the parameters of Table 4.2) the same voltage clamp protocol and the same ionic concentrations ($[Ca^{2+}]_o$=2 mM) as in Kim *et al.* (2002).

Potassium Channels

Voltage dependent K^+ channels encoded by the $K_v1.1$ gene have been identified in cultured murine ICC by immunohistochemical experiments using the double labelling technique and functionally characterised with patch clamp experiments on xenopus oocytes transfected with mRNA encoding canine Kv1.1 (Hatton *et al.*, 2001). The following equation was adopted

$$I_{kv11} = G_{kv11} * d_{kv11} * f_{kv11} * (V_m - E_K) \tag{4.7}$$

Here I_{kv11} is the current flowing through these voltage dependent K^+ channels. G_{kv11} (6.3 nS) is the maximal conductance, E_K is the Nernst potential for K^+ ions, d_{kv11} and f_{kv11} represent voltage dependent gating variables whose parameters (see Table 4.2 and Figure 4.4) have been fitted to voltage clamp experiments (Hatton *et al.*, 2001)(Table 4.2).

Ether-a-go-go (ERG) channels have been proposed as important regulators of pacemaker activity in ICC (Zhu *et al.*, 2003). The characteristics of the ERG channels in ICC have been studied in detail in ICC by McKay *et al.* (2006) from which the following equation was derived

$$I_{ERG} = G_{ERG} * d_{ERG} * (V_m - E_K) \tag{4.8}$$

where I_{ERG} is the current flowing through ERG channels. d_{ERG} is a voltage-dependent gating variable (see Table 4.2 and Figure 4.4) and G_{ERG} (2.5 nS) is the maximal conductance.

The presence of Ca^{2+}-activated K^+ channels (BK) has been confirmed in

ICC via immunocytochemical techniques in the murine jejunum and lower oesophageal sphincter (Cho & Daniel, 2005). A similar conductance had been previously identified in canine colonic ICC (Langton *et al.*, 1989a) and no major difference between BK conductance in ICC and and surrounding myocytes was found in terms of their voltage and intracellular Ca^{2+} dependency (Farrugia, 1999). The BK channels in ICC were therefore assumed to be not substantially different from those in gastric SM cells and the same description used by Corrias & Buist (2007) was adopted.

$$I_{BK} = G_{BK} * P_{BK} * (V_m - E_K) \tag{4.9}$$

Here I_{BK} is the ionic current flowing through BK channels and G_{BK} (23 nS) represents the temperature dependent maximal conductance and P_{BK} is the Ca^{2+} and voltage-dependent open probability that is given by

$$P_{BK} = \frac{1.0}{1 + e^{\frac{V_m}{K_{BK}} - h_{BK} * log\frac{[Ca]_i}{Ca_{set}}}} \tag{4.10}$$

where the values of K_{BK} (-17), Ca_{set} (100μM) and h_{BK} (2) were taken from Carl *et al.* (1996). A background K^+ conductance was also included in the model and was described as

$$I_{Kb} = G_{Kb} * (V_m - E_K) \tag{4.11}$$

where I_{Kb} represents the total background potassium current with a maximal conductance G_{Kb} of 0.15 nS.

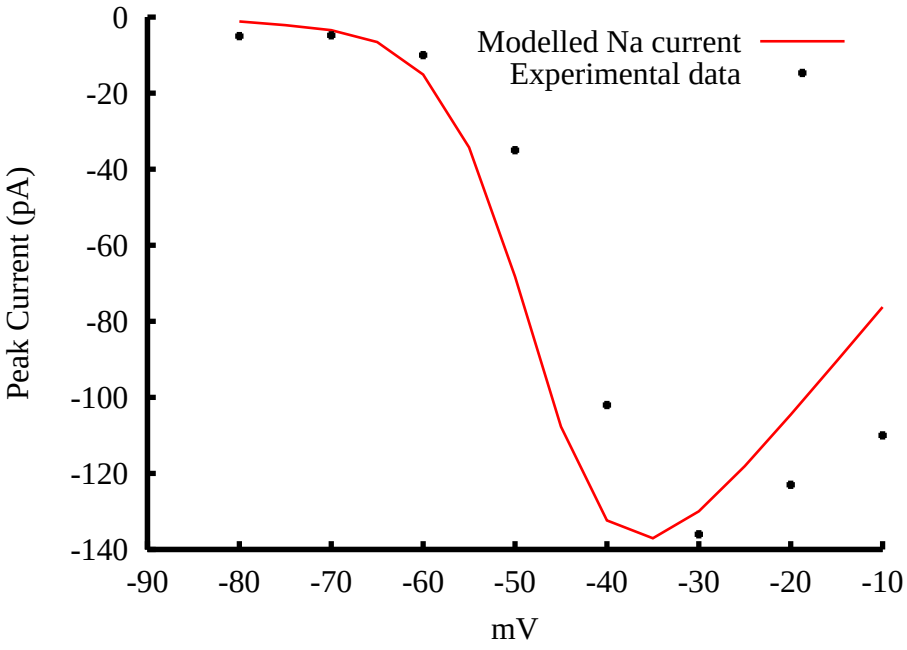

Figure 4.6: I-V plot in the physiological range for Na^+ currents: the black crosses are manually extrapolated from Figure 3 of Strege *et al.* (2003) while the red line is obtained by applying to Equation 4.12 (with the parameters of Table 4.2) the same voltage clamp protocol and the same ionic concentrations ($[Na^+]_o$=149.2 mM and $[Na^+]_i$=70 mM) as in Strege *et al.* (2003).

Sodium Channels

An SCN5A-encoded Na^+ conductance has been found in human intestinal ICC by RT-PCR experiments (Strege *et al.*, 2003). This current, believed to influence the rise phase of the slow waves, is Tetrodotoxin (TTX)-resistant. The following equation was used to describe this current.

$$I_{Na} = G_{Na} * d_{Na} * f_{Na} * (V_m - E_{Na}) \tag{4.12}$$

Here I_{Na} represents the ionic current flowing through Na^+ channel, E_{Na} is the Nernst potential for Na^+ ions, d_{Na} and f_{Na} represent voltage dependent gating variables whose parameters (Table 4.2) along with the maximal conductance G_{Na} (20 nS), have been chosen to replicate voltage clamp experiments (Strege *et al.*, 2003) as shown in Figure 4.6.

Non-specific Cationic Conductance

NSCC are theorised to be the primary pacemaking conductance and allow ionic fluxes into the SS. The following equation was introduced to describe the NSCC channels

$$I_{NSCC} = G_{NSCC} * P_{openNSCC} * (V_m - E_{NSCC}) \tag{4.13}$$

where I_{NSCC} is the ionic current and G_{NSCC} is the maximal conductance (12.15 nS). The value of G_{NSCC} was chosen to produce pacemaker potentials of sufficient size to activate the conductances on the plasma membrane responsible for the upstroke of the slow wave under normal conditions. E_{NSCC} is the reversal potential for NSCC channels which was calculated with the Goldman-Hodgkin-Katz equation

$$E_{NSCC} = \frac{RT}{F} log \frac{[K]_o + P[Na]_o}{[K]_i + P[Na]_i} \tag{4.14}$$

where P is the ratio between Na^+ and K^+ permeability and was set to 1.056 in agreement with the notion that NSCC channels are substantially equally permeable to Na^+ and K^+. $P_{openNSCC}$ is the Ca^{2+}-dependent open probability

whose Ca^{2+} dependence has been briefly illustrated previously (Sanders *et al.*, 2006a). Here a Hill equation was used to describe the experimental data.

$$P_{openNSCC} = \frac{1.0}{1 + (\frac{K_{openNSCC}}{[Ca]_{SS}})^{h_{openNSCC}}} \tag{4.15}$$

$[Ca]_{SS}$ is the Ca^{2+} concentration in the pacemaker unit, $K_{openNSCC}$ and $h_{openNSCC}$ are half value and Hill coefficient respectively and their values (74.5 μM and -85 respectively) have been chosen to yield a physiological response with respect to the expected Ca^{2+} concentrations in the SS.

Chloride Channels

The presence and functions of Cl^- in ICC has been object of controversy (Sanders *et al.*, 2006a). Zhu *et al.* (2005) identified an inwardly rectifying whole cell current that the authors believe is carried by Cl^- ions. This dependence was described by the following equation

$$I_{Cl} = G_{Cl} * d_{Cl} * (V_m - E_{Cl}) \tag{4.16}$$

where I_{Cl} is the ionic current, E_{Cl} is the Nernst potential for Cl^- ions, G_{Cl} (10.1 nS) is the maximal conductance and d_{Cl} is a gating variable that takes into account the mechanisms of intracellular regulation of Cl^- channels. Although not fully understood, some investigators have suggested that intracellular Ca^{2+} may play a role in regulating Cl^- currents in ICC (Tokutomi *et al.*, 1995; Zhu *et al.*, 2005). Intracellular Ca^{2+} is already proposed as a regulatory component of Cl^- channels in smooth muscle cells in different organs with thresholds of

activation above 100 nM (Carl *et al.*, 1996). Here the following Hill equation was used to model the steady state effect of intracellular Ca^{2+} on the Cl^- current.

$$d_{Cl\infty} = \frac{1.0}{1 + (\frac{K_{Cl-act}}{[Ca]_i})^{h_{Cl}}} \tag{4.17}$$

Here K_{Cl-act} represents the activation threshold and h_{Cl} represents the Hill coefficient. Their values (140 nM and 3 respectively) have been chosen in view of the intracellular Ca^{2+} concentrations experienced in ICC as well as taking into account activation thresholds measured in other cell types for this type of conductance (Carl *et al.*, 1996). A time constants of 30 ms has been used to represent the kinetics of Cl^- channels opening in the calculation of d_{Cl}.

Ca^{2+} Extrusion Mechanism

At least two proteins have been identified in ICC for the purpose of Ca^{2+} extrusion from the cytoplasm, the plasmalemmal Ca^{2+} pump (PMCA) and the Na^+/Ca^{2+} exchanger (NCX1) (Cho & Daniel, 2005). As quantitative data pertaining the kinetics of these proteins was not available, a phenomenological description of these Ca^{2+} extrusion mechanisms was included in order to provide long term intracellular homeostasis.

$$J_{Ca-EXT} = J_{Ca-EXT-MAX} \frac{1.0}{1 + (\frac{K_{Ca-EXT}}{[Ca]_i})} \tag{4.18}$$

Here J_{ca-EXT} is the Ca^{2+} efflux (in mM/s), $J_{ca-EXT-MAX}$ (0.0885 mM/s) and K_{Ca-EXT} (298 nM) are the maximal flux and the half concentration respec-

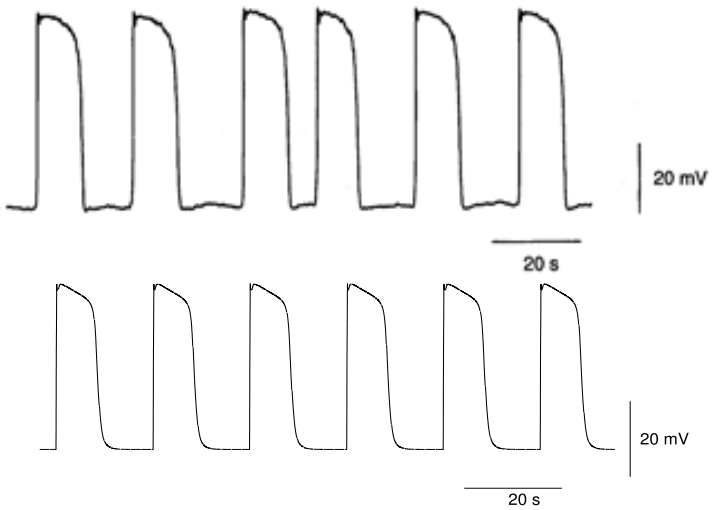

Figure 4.7: (A) Slow waves recorded from guinea-pig antral ICC (adapted from Hirst & Edwards (2001)). (B) Simulated gastric slow waves obtained after 10 minutes of simulated slow waves activity from the presented model.

tively. Intracellular Ca^{2+} concentration is therefore determined by

$$\frac{d[Ca]_i}{dt} = -\frac{I_{CaL} + I_{VDDR}}{2F * V_{cyto}} - J_{Ca-EXT} + J_{leak} \tag{4.19}$$

where V_{cyto} is the cytoplasmic volume.

4.3 Model Predictions and Validation

Integration of Equation 4.1 with the incorporation of the other model equations yields the ICC membrane potential as a function of time as is shown in Figure 4.7. The generation of slow waves occurred spontaneously and steadily even for long simulation times (> 1 hour). The frequency was 3.02 waves

per minutes, in general agreement with experimental recordings at 37 degrees from the canine gastric antrum (2.8 waves per minute) (Ward *et al.*, 2004), and guinea-pig gastric antrum (3.6 waves per minute) (Hirst & Edwards, 2001). Three waves per minute is also the dominant frequency in the normal human stomach (Koch, 2001). The value of the resting potential at -67.6 mV was, again in agreement with experimental measurements from guinea-pig gastric antrum (ranging from -65.7 mV (Hirst & Edwards, 2001) to -70 mV (Ward *et al.*, 2000)). The primary component and plateau phase could be clearly distinguished in the profile of a simulated slow wave (Figure 4.8). The amplitude of the primary component was 43.63 mV and the peak amplitude was 43.8 mV. These values were found to have an average of 44.5 mV and 45.9 mV respectively in a series of experiments on guinea-pig antral ICC (Hirst & Edwards, 2001). The half width and maximal upstroke rate of the simulated slow wave were 8.31 seconds and 0.5 V/s respectively; both values are very similar to the ones obtained from guinea-pig antral ICC (8.36 seconds and 0.4 V/s respectively (Hirst & Edwards, 2001)).

To further ensure the validity of the model, the effect of several different experimental conditions was simulated to determine their effect on the behaviour of the generated slow waves.

4.3.1 Involvement of Mitochondrial Activity in Generation of Slow Waves

The involvement of mitochondria in the pacemaker mechanism in ICC has been subject of several experiments. An addition of CGP37157, a potent in-

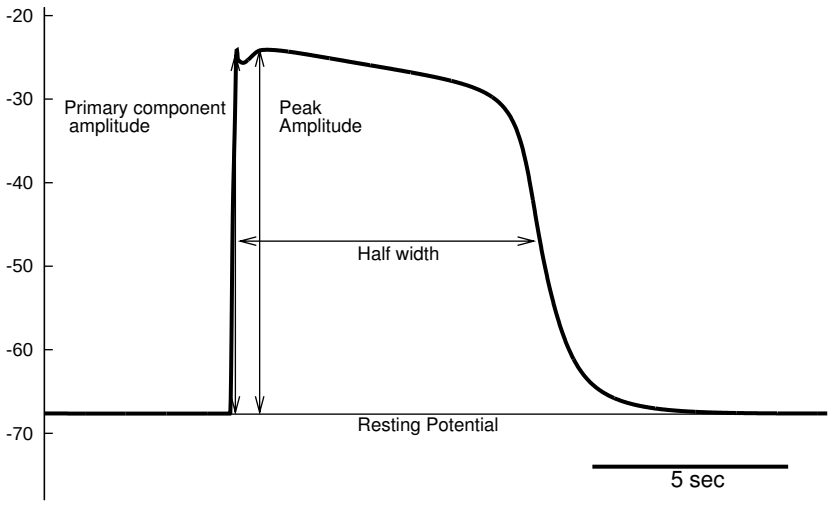

	Simulation	Experiments
Frequency (cpm)	3.02	2.8 to 3.6
RMP (mV)	-67.7	-70 to -65
Amplitude of Primary component (mV)	43.6	44.5
Peak amplitude (mV)	43.8	45.9
Half width (s)	8.31	8.36
Maximum upstroke velocity (V/s)	0.49	0.4

Figure 4.8: Detail of a single simulated slow wave and quantitative comparison with experimental values. The experimental values are taken from the following references: Hirst & Edwards (2001), Ward *et al.* (2000) and Forrest *et al.* (2006).

hibitor of the mitochondrial Na^+/Ca^{2+} exchanger, caused the inhibition of slow wave activity in the murine intestine (Kim *et al.*, 2006a). This was simulated by altering the conductance of the mitochondrial Na^+/Ca^{2+} exchanger and under these conditions the model also ceased to generate slow waves. Similarly, experiments have been performed to determine the involvement of the mitochondrial membrane potential on the generation of slow waves in the guinea-pig (Beckett *et al.*, 2004; Fukuta *et al.*, 2002) and canine (Ward *et al.*, 2004) stomach as well as in murine jejunum (Ward *et al.*, 2000). In all cases, the addition of mitochondrial uncouplers such as CCCP caused a cessation of slow wave generation. Such an addition was simulated by decreasing the magnitude of the mitochondrial membrane potential. Again the model correctly showed a termination of slow waves generation under such conditions.

4.3.2 Involvement of the ER on Slow Wave Activity

Malysz *et al.* (2001) investigated the influence of IP3-dependent Ca^{2+} release on slow wave activity in the murine small intestine. They found that blockade of IP3-dependent Ca^{2+} release by Xestospongin C eventually abolished slow wave activity. Similar observations were made in similar tissue by Ward *et al.* (2000). On the other hand, it was observed that stimulation of IP3-dependent Ca^{2+}release by generation of IP3 through a G protein-dependent pathway (triggered by stimulation of α1-adrenoreceptors) caused an increase in the frequency of slow wave activity coupled with a suppressed plateau phase in the murine small intestine (Malysz *et al.*, 2001). The model was tested under both of these conditions by conducting two separate simulations, one with

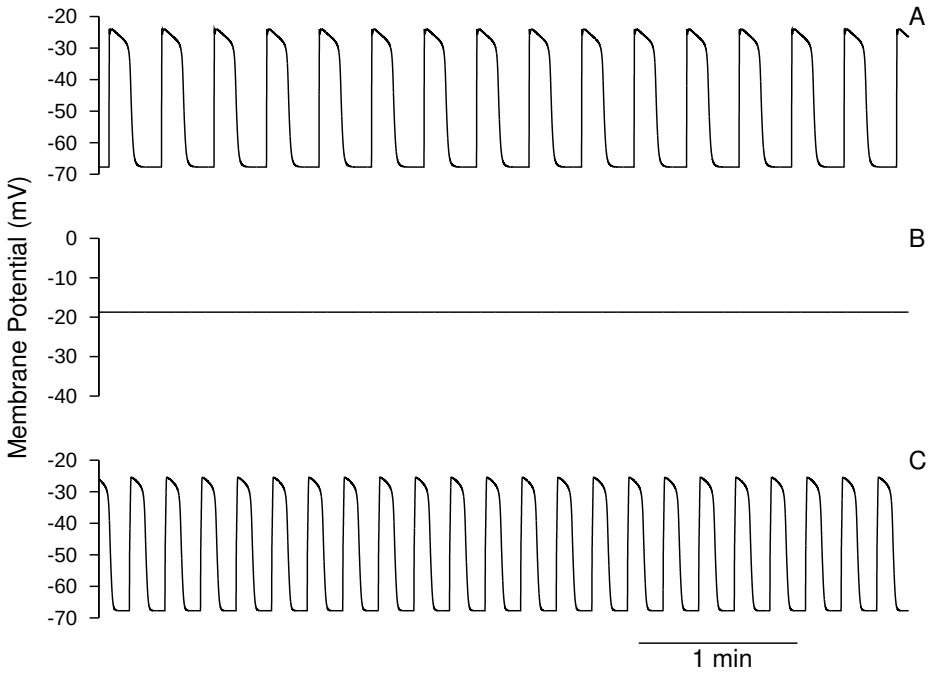

Figure 4.9: (A) Simulated slow waves in control condition. (B) Simulated presence of Xestospongin C by setting to zero the Ca^{2+} release from the ER. (C) Simulated presence of α1-adrenoreceptors stimulation with consequent increase in IP3 level by 70 nM.

the value of the IP3-mediated Ca^{2+} efflux from the ER set to zero (blockade) and the other with an increased concentration of IP3. Figures 4.9B and 4.9C shows the results of simulated slow waves in such conditions compared to control conditions in Figure 4.9A. Here the lack of IP3-mediated Ca^{2+} release abolished slow waves (Figure 4.9B), in agreement with the observed effects of Xestospongin C (Malysz *et al.*, 2001). Increasing the concentration of IP3 by 70 nM caused an increase in slow wave frequency to 4.0 cycles per minute and a reduced plateau phase (half width reduced from 8.2 to 5.8 seconds, Figure 4.9C) in agreement with the experimental observations (Malysz *et al.*, 2001).

2-Aminoethoxydiphenyl Borate (2APB) is known to be a membrane permeable agent capable of compromising Ca^{2+} handling by the ER. Recent reports suggest that it directly inhibits Ca^{2+} entry pathways into the ER (Bootman *et al.*, 2002; Dobrydneva & Blackmore, 2001). Fukuta *et al.* (2002) observed that addition of 2APB caused a reversible blockade of slow wave activity in the guinea-pig stomach (Figure 4.10A). We simulated the presence of 2APB by inhibiting the Ca^{2+} entry pathway into the ER. The results of these simulations showed a reversible cessation of slow wave activity (Figure 4.10B) in agreement with the experimental data. In the experimental recordings, the effects of 2APB were gradual and not immediate, i.e., after addition of 2APB to the bath solution, some time is necessary before slow waves start decreasing in amplitude and eventually disappear. This is presumably due to the time taken by 2APB to diffuse within the bath, enter the cell under investigation and start acting on the ER proteins in a dose-dependent manner. Similar time-dependent effects were seen for the wash-out of 2APB, presumably due to the time taken to remove 2APB from the solution. In our simulations, however, application of 2APB is instantaneous, i.e., at a given time the variable J_{SERCA}, which describes Ca^{2+} entry in our model, is put to zero, thus simulating an instantaneous effect of 2APB. The time taken by 2APB to reach the cell as well as the time taken to act on the ER proteins are therefore neglected. Similar considerations can be made for the wash-out of 2APB which, in our model is instantaneous.

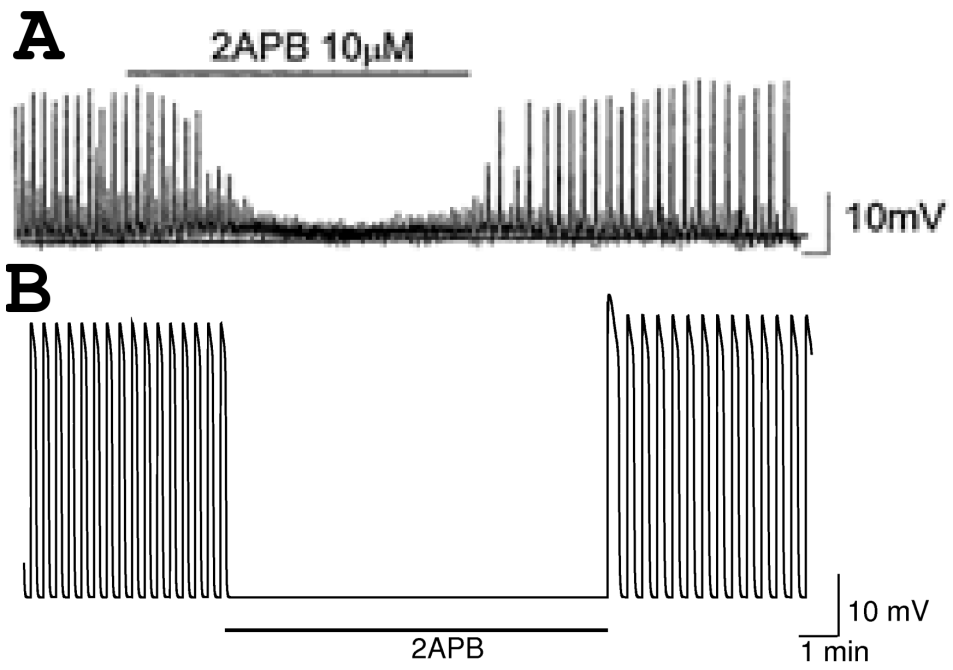

Figure 4.10: A) Effect of addition of 2APB on ICC gastric slow waves from guinea-pig adapted from Fukuta *et al.* (2002) B) Simulated slow waves in the presence of 2APB, a blocker of Ca^{2+} entry into ER.

4.4 Summary of the ICC Model

Although the first hints of autonomous ICC electrical activity have been apparent since the end of nineteenth century, it was only about two decades ago that ICC were definitively established as pacemaker cells in the GI region (Langton *et al.*, 1989a; Barajas-Lopez *et al.*, 1989). Since then, ICC have received an ever increasing amount of attention by many research groups as several motility dysfunctions such as gastroparesis, functional dyspepsia and gastrointestinal stromal tumours have been related to abnormal ICC behaviour (Streutker *et al.*, 2007). In spite of this, the cellular mechanisms that underlie slow wave generation are not yet fully understood. Here the hypothesis that a Ca^{2+}-inhibited NSCC is the primary pacemaker conductance has been adopted. This operates under the primary influence of the Ca^{2+} concentration in a space delimited by ER, mitochondria and plasma membrane as proposed by Sanders *et al.* (2006a). There is also debate regarding the possible molecular candidates for the NSCC. Although a relationship between a melastatin type transient receptor potential (TRPM7) and pacemaker currents in ICC has been suggested (Kim *et al.*, 2006b) the molecular identity of the NSCC remains unknown. Although a definitive determination of the molecular identity of the NSCC would allow a better understanding of ICC pathophysiology, this would not have a direct impact on the validity of this model as it is the properties of the channel and not its molecular identity that are of primary importance here.

There exist other theories that differ from the NSCC hypothesis. Of particular note is the hypothesis that it is a Cl^- conductance and not a NSCC

that is the primary pacemaker conductance (Zhu *et al.*, 2005). This theory is based on single channel recordings obtained from non-enzymatically isolated ICC with the cell-attached patch clamp technique (Huizinga *et al.*, 2002). Such recordings showed a periodic, spontaneous channel opening at the same frequency as the slow wave generation on the same tissue. This current was identified as a Cl^- current primarily based on the observed reversal potential (-34 mV), consistent with conduction of Cl^- ions. Also other authors hypothesised that the pacemaker conductance in ICC was a Cl^- one (Tokutomi *et al.*, 1995) after observing a cessation of slow wave generation in presence of 4-acetoamido-4-isothiocyanat-ostilbene-2,2'-disulphic acid (SITS), a known Cl^- channel blocker. Nevertheless, the association of pacemaker currents with a Cl^- conductance has been challenged (Sanders *et al.*, 2006a) on grounds of the non-specific effects that SITS might have on the cellular activity. Should the NSCC theory be displaced in the future, this model, due to its modular nature, can easily be updated by replacing the current primary pacemaker conductance (NSCC) with an equation describing the kinetics of the alternate mechanism.

Despite this ongoing controversy about the nature of the primary pacemaker conductance, there seem to be agreement on the role played by Ca^{2+} and its handling by the ER and mitochondria in regulating ion channels and consequently, in the generation of slow waves. The model was therefore developed starting with a validated model of mitochondrial and ER activity (Fall & Keizer, 2001). To this, descriptions of the main membrane ion channels that have been identified in ICC were coupled. Where possible, data was adopted

from isolated gastric ICC. Where direct measurements of currents from gastric ICC were not available, data from intestinal ICC or from gastric SM cells were used. The equations that were chosen to describe the ion channels were validated by simulated voltage clamp experiments and the results were compared with published experimental data under the same conditions wherever possible.

Some debate also exists with regard to the ionic conductances that are involved in the plateau phase. In particular, the form of the depolarising current that counterbalances the activation of K^+ conductances during the plateau has not been resolved. It has been suggested that more than one conductance may participate and that L-type Ca^{2+} channels may have a role due to their incomplete inactivation during voltage clamp experiments (Molleman, 1995). The same investigator deemed it unlikely that L-type Ca^{2+} channels were the sole depolarising factor during the plateau phase and observed that manipulation of Cl^- and Na^+ concentrations led to modifications of the slow wave plateau. The involvement of Cl^- (Kito & Suzuki, 2003) and possibly other Na^+ dependent membrane ionic mechanisms was therefore hypothesised. A Cl^- conductance was included in the model description due to reports of its presence and influence in ICC activity (Huizinga *et al.*, 2002; Zhu *et al.*, 2005), in particular in the regenerative component of the slow wave (Hirst *et al.*, 2002). Here the Cl^- conductance does not constitute a primary pacemaker conductance but contributes to the plateau phase of the slow wave. Other investigators have suggested that the plateau of the slow wave might arise from the summation of many pacemaker potentials entrained successively by an initial event (Sanders

et al., 2006a). The velocity of slow wave conduction would, however, suggest that in this case either not all of the pacemaker units are activated by the initial upstroke of the slow wave as it moves through the tissue, or that some pacemaker units recover quickly enough to be discharged a second time during the plateau phase. As is the case in other cell types, here the SS represents the summation of individual subcellular spaces but it is clear that in the future further investigation is needed in this area.

The four K^+ conductances included in the model represent those that have been well quantified through patch clamp experiments and are all believed to provide significant contributions to the slow wave. It should be noted, however, that this is not an exhaustive list of those K^+ channels that have been found in ICC. In particular, ATP dependent K^+ channels, intermediate (IK) and small (SK) Ca^{2+} -activated K^+ channels may also be included in the model description once comprehensive quantitative characterisations become available.

The model can be thought of as two tightly coupled components, the internal calcium cycling mechanisms that initiate pacemaker activity and the components on the plasma membrane that form the slow wave in response to this activity. As demonstrated in Figure 4.9C, spontaneous rhythmicity can be maintained over a range of pacing frequencies by an appropriate manipulation of the appropriate calcium cycling parameters. The shape of the resulting slow wave is primarily determined by the parameters of the plasma membrane components and in general these may be adjusted to alter the shape of the slow wave without a cessation of activity.

In conclusion, we have developed and validated a robust model of slow wave generation by a gastric ICC. We have realistically described all the main ion channels and intracellular processes that are believed to contribute to the generation of the slow waves. This confers to the presented mathematical model important predictive abilities that can be exploited for a better understanding of ICC pathophysiology. In particular, it could be possible to evaluate the effects of the altered functioning of certain cellular components over the overall cellular physiology thus gaining an insightful understanding of the pathophysiological processes underlying a disease state.

Chapter 5

One Dimensional Simulations

5.1 Introduction

Having presented single cell descriptions, one dimensional simulations represent the next conceptual step towards the development of a multiscale modelling framework. In this chapter, we will focus on a particular physiological property of the gastric tissue, the longitudinal Carbon Monoxide (CO) gradient along the stomach, by making use of the two cellular models described in Chapters 3 and 4 coupled together via a cable model.

5.2 Background

As mentioned in Section 1.3, two main types of ICC have been identified in the stomach. ICC-MY constitute a dense cellular network in the myenteric plexus while intramuscular ICC (ICC-IM) are interspersed in between SM cells, mainly in the circular layer, in all regions of the stomach. Recent morphological

and immunohistochemical studies have highlighted significant differences in the number of ICC, SM cells and distribution of gap junctions in different regions of the stomach (Komuro, 2006, 1999). A broad diversity in slow wave activity in different regions of the stomach has also been highlighted by many investigators. The stomach fundus is more depolarised than any other region of the stomach and, despite displaying a dense population of ICC (Stratton *et al.*, 2007; Komuro, 2006), is electrically silent (Szurszeswski JH, 1987). Slow waves are believed to originate in the mid-corpus region on the greater curvature of the stomach and propagate aborally towards the pylorus, which consitutes an electrical barrier to the slow wave propagation (Lammers *et al.*, 1998). Corporal slow waves present a characteristic triangular shape whereas in the antral circular muscle the shape becomes biphasic where a rapid upstroke phase is followed by a quick partial repolarisation and a long plateau phase (Dickens *et al.*, 1999; Hirst & Edwards, 2006). Antral slow waves have a more negative resting membrane potential (RMP) and greater amplitude than corporal slow waves (Hirst & Edwards, 2006).

Carbon Monoxide is a well known biomolecule that, under normal physiological conditions, is produced endogenously in many human tissues (see Durante *et al.* (2006) for a review). Recent experimental evidence has suggested that ICC in the GI tract produce CO through a heme-oxygenase-2 (HO-2)-mediated pathway (Szurszewski & Farrugia, 2004; Kadinov *et al.*, 2002). CO is believed to be a major hyperpolarising factor in the gastrointestinal musculature (Farrugia *et al.*, 2003). A gradient in CO concentration has been proposed to be responsible for the gradient in RMP that has been observed

along the GI tract (Szurszewski & Farrugia, 2004). Experimental observations made on genetically modified HO-2-null mice that lacked a membrane potential gradient (Farrugia *et al.*, 2003) appear to confirm the relationship between RMP and CO concentration gradients. The mechanisms through which CO causes membrane hyperpolarisation in GI SM cells have yet to be fully elucidated. Although all investigators seem to agree that the hyperpolarising effect is obtained through the activation of K^+currents by CO, it is not clear which particular K^+ current is involved and how it is augmented by CO. In vascular SM cells, a direct biochemical modification of Ca^{2+}- dependent K^+channels (K_{Ca}) by CO has been proposed (Wang & Wu, 1997). In guinea-pig gastric SM cells, a cGMP- and PKG-dependent vectorial intracellular mobilisation of Ca^{2+} ions has been suggested to cause the augmentation of I_K (Kadinov *et al.*, 2002). In human intestinal myocytes, on the other hand, no change on intracellular Ca^{2+} levels was noted after the application of exogenous CO (Farrugia *et al.*, 1998) supporting previous suggestions that the augmentation of I_K appears to be due to voltage dependent and not Ca^{2+}-activated K^+channels (Farrugia *et al.*, 1993). Moreover, this does not exclude localised changes in Ca^{2+} concentration.

In this chapter, we aim to investigate the effects and physiological significance of the different CO concentrations in different regions of the stomach. We simulated slow wave activity in a one dimensional cable that ran from the top of the fundus to the pylorus along the greater curvature of the stomach. Cable models have been widely used to describe the electrophysiology of a variety of tissues including neural tissue (Bedard & Destexhe, 2008), cardiac

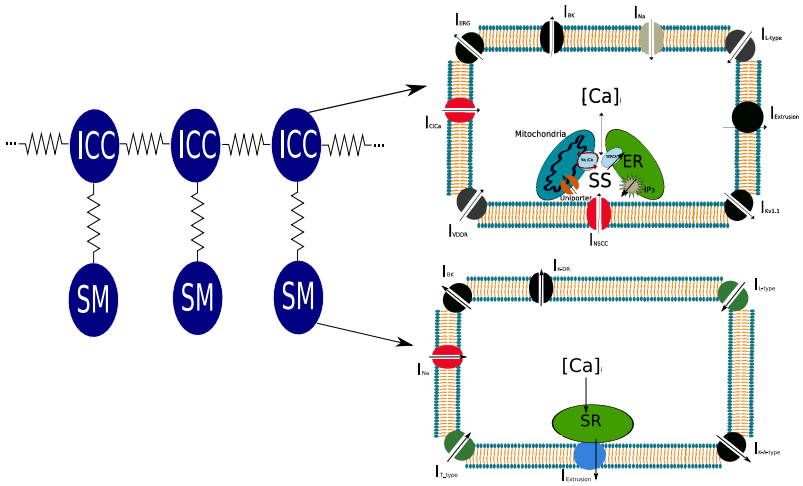

Figure 5.1: Schematic view of the one dimensional simulations. Electrical connections between ICC and SM cells along the fibre are shown on the left while a schematic view of the cellular models of ICC (upper panel) and SM cells (lower panel) are shown on the right.

muscle (ten Tusscher *et al.*, 2004; Bondarenko & Rasmusson, 2007) and skeletal muscle (Huang & Peachey, 1992). In the GI tract, a similar one dimensional modelling approach was employed by Edwards & Hirst (2005) who modelled slow wave propagation across the antral stomach wall (from serosa to mucosa) (Section 2.2.3). However, a phenomenological description of the equivalent circuits represented by ICC and SM cell was used and the model developed by Edwards & Hirst was hindered by the lack of an explicit description of the ion channels on which CO is believed to act. Our simulations make use of two realistic biophysically based computational descriptions of the electrophysiology of gastric ICC (Chapter 4) and SM cells (Chapter 3). Compared to a phenomenological description, a biophysically based model enables us to replicate the effects, at the ion channel level, of the different CO concentrations and make predictions regarding its physiological significance.

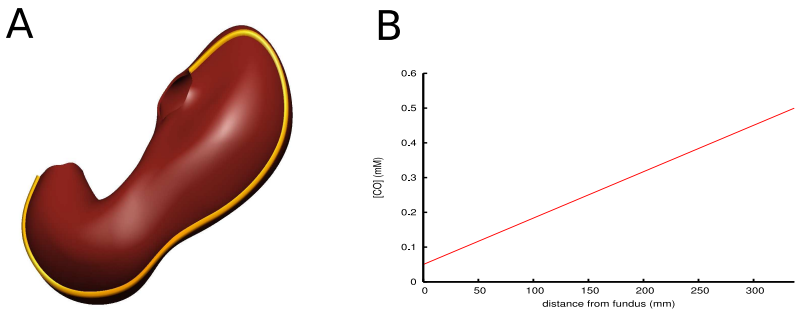

Figure 5.2: Illustration of the simulated cable: A) the one dimensional cable running from the top of the fundus to the pylorus is shown in a 3D model of the stomach. B) Carbon monoxide concentration as a function of position along the cable.

5.3 Mathematical Formulation

The two cell models described in Chapters 3 and 4 were incorporated into the description of a 1D cable as shown in Figure 5.1. The propagation of the electrical activity along a one-dimensional fibre of ICC was described following a standard nonlinear cable equation as previously discussed in Section 1.4.2 (Equation 1.16)

$$\sigma \frac{\partial^2 V_{m\_ICC}}{\partial x^2} = A_m (C_m \frac{\partial V_{m\_ICC}}{\partial t} + I_{ion}) \tag{5.1}$$

where V_{m_ICC} is the ICC transmembrane potential, x is a spatial coordinate along the axis of the fibre, C_m is the ICC membrane capacitance, A_m is the surface-to-volume ratio (200 mm^{-1}), and I_{ion} represents the summation of all the ionic currents as described in Equation 4.3 (Corrias & Buist, 2008) (also shown in Figure 5.1). In this formulation, each ICC is connected to a neighbouring ICC and to a SM cell (Cousins *et al.*, 2003; Dickens *et al.*, 1999;

Komuro, 1999). Both connections occur via gap junctions (Daniel, 2004) that are simulated via a fixed resistance. There appears to be no active propagation of electrical activity between SM cells (Sanders *et al.*, 2006a). The resulting electrical configuration is illustrated in Figure 5.1. At each time step, the calculated value of V_{m_ICC} was used to compute the value of the electrical current (I_{ext}) exchanged between the ICC and SM cells

$$I_{ext} = G_{couple}(V_{m\_SM} - V_{m\_ICC}) \tag{5.2}$$

where G_{couple} is the coupling resistance between the ICC and SM cells and was set at 1.3 nS, as previously discussed in Section 3.2.2, representing the passive conductance of the gap junction between ICC and SM cells. The transmembrane potential of the SM cell can then be calculated through

$$\frac{dV_{m\_SM}}{dt} = -\frac{1}{C_{m\_SM}}(I_{ion\_SM} + I_{ext}) \tag{5.3}$$

where V_{m_SM} is the SM cell transmembrane potential, C_{m_SM} is the membrane capacitance and I_{ion_SM} is given by Equation 3.2, representing the summation of all the ionic currents in the SM cell. We constructed a one-dimensional cable mesh based on a 337 mm long fibre. This length was chosen according to anatomical estimates, based on images from the Visible Human Project (Spitzer *et al.*, 1996), of the distance between the top of the fundus and the pylorus along the greater curvature of the stomach as shown in Figure 5.2A (Pullan *et al.*, 2004). All regions of the stomach have been reported to contain ICC (ICC-MY, ICC-IM or both) (Komuro, 1999, 2006). ICC have been found

even in the electrically silent fundus (Stratton *et al.*, 2007) and were therefore included along the entire fibre. The value of the tissue conductivity σ was chosen according to experimental measurements on the guinea-pig antrum (Cousins *et al.*, 2003). When small preparations (400-800 μm in length and 60-150 μm in diameter) were impaled and current stimuli were passed from one electrode to another, the resistance that the authors measured ranged from 3.75 to 17.3 MΩ in four experiments. The authors did not specify the distance between the electrodes. If we assume a distance between the electrodes of 400 μm and use the median value of the diameter at 105 μm, the resulting conductivity values (calculated as inverse of resistivity) range from 2.6 to 15.25 μS/mm. Here we chose a constant value of 5 μS/mm for the tissue conductivity.

The one-dimensional geometry was discretised with 400 elements over which Equation 5.1 was solved using the finite element method, with a time step of 0.1 ms.

5.4 Modelling CO Distribution and Action

We simulated the gradient in CO concentration along the long axis of the stomach with a linear relationship increasing from the fundus (minimal concentration=0.05 mM) to the pylorus (maximal concentration=0.5 mM) as shown in Figure 5.2B. The values of CO concentration were chosen according to experimental measurement on canine stomach showing that CO concentration increases its value in a linear manner from the fundus to the antrum (around 0.1 nmol/mg of wet tissue in the fundus to about 0.5 nmol/mg of wet tissue

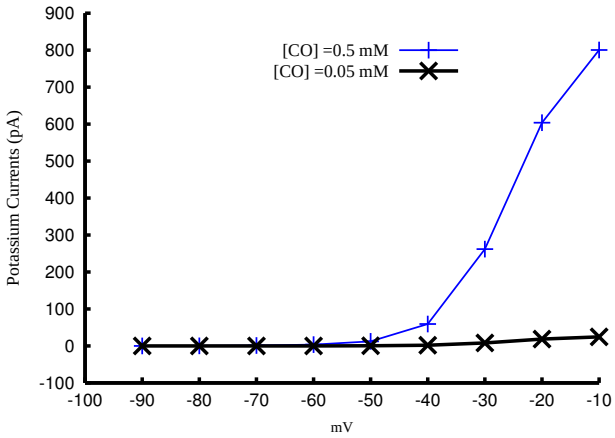

Figure 5.3: Corresponding I-V (peak currents) curve variation of voltage dependent K^+currents in the SM cell model under simulated voltage clamp condition. Minimal CO concentration is 0.05 mM (black line), maximal is 0.5 mM (blue line).

in the outer part of the antrum) (Farrugia *et al.*, 1998). We assumed CO to affect the voltage dependent K^+ channels of both ICC and SM cells in a dose dependent manner (Farrugia *et al.*, 1998). The higher the CO concentration, the bigger the maximal K^+current as shown in Figure 5.3. The effects of different CO concentrations on the cellular K^+ conductances has been simulated by introducing a CO-dependent multiplying scaling factor, f_{CO}, to the voltage dependent maximal conductances in the two cell models. The following linear expression for calculating f_{CO} has been used.

$$f_{CO} = 2.8 * [CO] - 0.1 \tag{5.4}$$

The parameters of such relationship have been chosen in order to replicate the experimental IV plots from patch clamp experiments conducted on isolated canine jejunal cells in presence of CO (compare Figure 5.3 with Figure 3 of

Farrugia *et al.* (1998)). The factor f_{CO} was added as an additional gating variable to the K^+ voltage dependent ionic currents in both the ICC and SM cell models. The I_{ion} terms of the cell models were therefore effectively rewritten as

$$I_{ion(ICC)} = I_{L-type}+I_{VDDR}+I_{ClCa}+I_{NSCC}+I_{BK}+I_{Na}+f_{CO}*(I_{kv11}+I_{ERG}+I_{bK}) \tag{5.5}$$

$$I_{ion(SM)} = I_{L-type} + I_{T-type} + I_{BK} + I_{Na} + f_{CO} * (I_{A-type} + I_{K-DR} + I_{bK}) \tag{5.6}$$

Frequency Gradient and Entrainment of Slow Waves

It is known that muscle strips isolated from the stomach generate slow waves at different frequencies. The frequency is higher in the corpus and lower in the antrum (Hirst & Edwards, 2006; Szurszeswski JH, 1987). Nevertheless, when the entire stomach is considered, higher frequency corporal slow waves are capable of entraining antral slow waves giving rise to a dominant frequency throughout the stomach (Hirst & Edwards, 2006; Sanders *et al.*, 2006a). While the mechanisms underlying this chronotropicity are not fully understood, it is known that IP3 has the ability to regulate slow wave frequency (Kim *et al.*, 2003). In our simulations, we included the capability of individual ICC cells in different locations to generate slow waves at different frequencies by setting a linear IP3 concentration gradient along the fibre. The gradient was from 670 nM at the top of the fundus (yielding an intrinsic pacemaking frequency of 4 cpm) to 600 nM at the pylorus (yielding an intrinsic pacemaking frequency of 3 cpm).

In an electrically coupled system such as the stomach tissue, where each

ICC is capable of spontaneously generating slow waves, a coordination mechanism that is capable of entraining the slow wave discharge across the tissue is necessary. Recent experimental evidence has shown that Ca^{2+} entry through voltage dependent, dihydropyridine-resistant pathways into the cell is involved in the coordination of slow wave discharge in the stomach (Lee *et al.*, 2007a; Bayguinov *et al.*, 2007). In order to replicate this entrainment mechanism, we modified the ICC model by redirecting 2% of dihydropyridine-resistent (I_{VDDR}) Ca^{2+} entry into the submembrane space.

5.5 Simulation Results

5.5.1 Generation and Propagation of Slow Waves

Results of numerical solutions of Equations 5.1-5.3 are summarised in Figure 5.4 where the SM cell transmembrane potential is shown along the one-dimensional fibre at different time instants. In the fundus, where the CO concentration is low and consequently K^+ currents are smaller, the membrane potential is locked in a depolarised state. The values of the SM cell membrane potential vary from -42.6 mV at the top of the fundus to -46.2 mV at 160 mm along the fibre, just before the site of slow wave initiation. This is consistent with experimental observations where slow waves could not be recorded from the fundus, and the value of the membrane potential was found to be -40 mV in guinea-pig gastric SM cells (Hirst & Edwards, 2006) and -48mV (Szurszeswski JH, 1987) in canine gastric SM cells.

Slow waves originated 178 mm from the top of the fundus in a location that

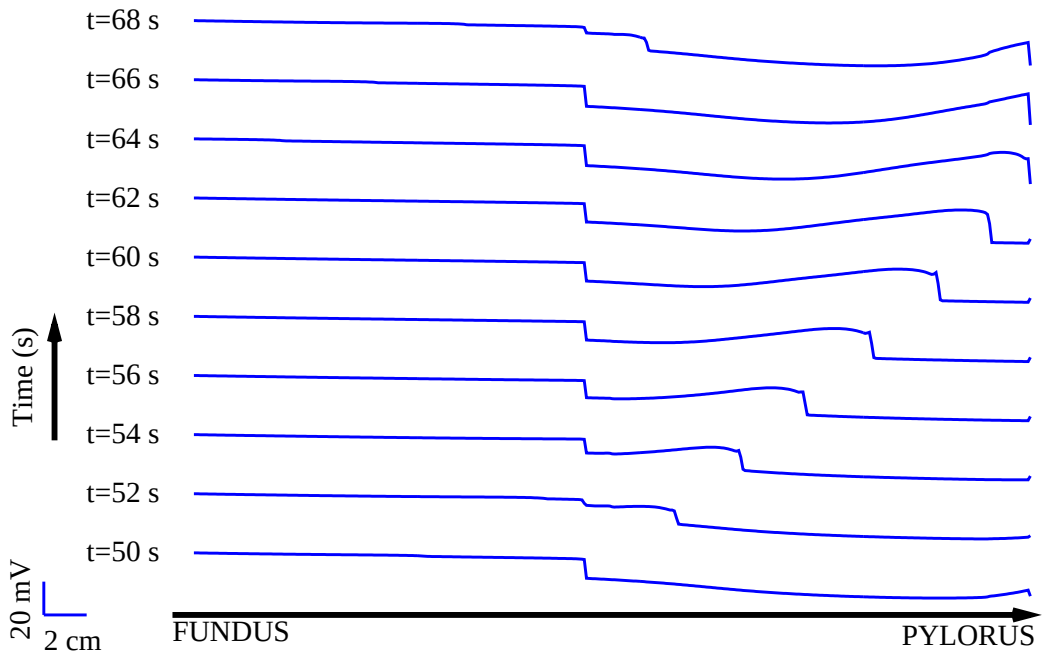

Figure 5.4: Propagation of slow waves along the fibre: SM cell transmembrane potential along the fibre at ten different time instants. Scale bars apply to all traces.

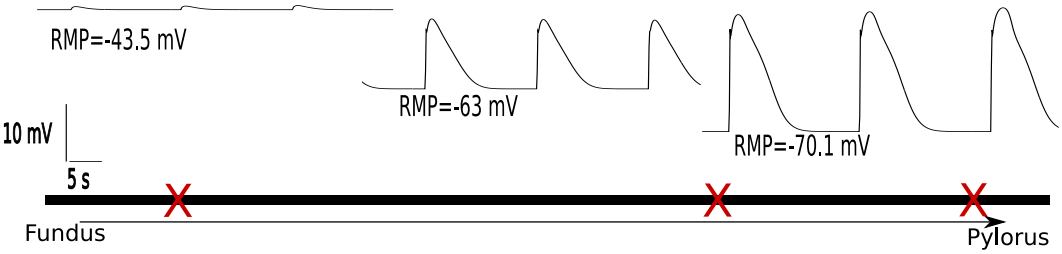

Figure 5.5: Simulated slow waves in different parts of the fibre. The traces show a period of simulated time between 75 and 130 seconds. Scale bars apply to all traces. The red crosses along the black fibre represent the three locations where the simulated traces are taken from. The distances from the top of the fundus are 42.5 mm, 210.6 mm and 294.9 mm respectively. Scale bars apply to all traces.

corresponds to the mid-corpus. Propagation along the remaining 159 mm of the fibre occurs at a velocity of 10 mm/s. The time taken to reach the pyloric ring was therefore around 16 seconds.

5.5.2 Slow Wave Heterogeneity

A slow wave displays different amplitudes and shapes as it moves through different locations along the fibre (see Figure 5.5). At the selected point in the fundus, slow waves failed to develop and the RMP was relatively constant at -43.5 mV. This value is well within experimental recordings which vary from -40 mV in the guinea-pig fundus (Edwards & Hirst, 2005) to -48 mV in the canine fundus (Szurszeswski JH, 1987). In the corpus the RMP was around -63 mV (RMP was found to be -60 mV in the canine mid orad corpus by Szurszeswski JH (1987)), slow waves were of small amplitude (13 mV) and had a triangular shape. The morphology of our simulated corporal slow waves matched well with recordings from the same region of the guinea-pig stomach

(Hashitani *et al.*, 2005; Edwards & Hirst, 2005) where the peak amplitude was found to be 15 mV. In the antrum, slow waves developed from a RMP of -70.1 mV (RMP was found to be -71 mV in the canine terminal antrum by Szurszeswski JH (1987)), were of bigger amplitude (23 mV, a value slightly smaller than the 30 mV recorded from guinea pig antrum by Edwards & Hirst (2005)) and displayed the characteristic biphasic shape.

5.5.3 CO Gradient and the Pacemaker Site

In order to investigate the influence of CO on the generation of slow waves, we simulated different gradients of CO along the fibre. Results are summarised in Figure 5.6 and reveal the ability of different CO gradients to shift the site of slow wave generation. When a CO gradient varying from 0.05 mM to 0.5 mM (red line in Figure 5.6) was simulated, the site of slow wave origin was found to be located 178 mm from the top of the fundus. Increasing the steepness of the CO gradient by 57%, which represents concentrations from 0.05 mM to 0.74 mM, (blue line in Figure 5.6) caused a shift in the site of slow wave origin in the orad direction. Under such conditions, slow waves originated 85 mm from the top of the fundus, compared to 178 mm for the reference simulation. On the other hand, decreasing the steepness of the CO gradient by 31%, which represents concentrations from 0.05 mM to 0.36 mM (green line in Figure 5.6), caused a shift in the site of slow wave origin in the anal direction. Under such conditions, slow waves originated 242 mm from the top of the fundus, compared to 178 mm for the reference simulation. Figure 5.7 confirms that in the case of a less steep gradient (corresponding to the green

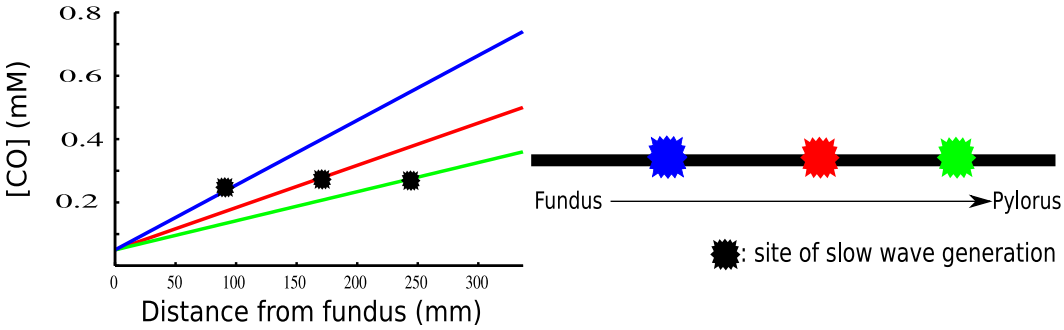

Figure 5.6: Three different CO gradients (left) and the corresponding locations of the site of generation of the slow waves along the fibre. The distances from the top of the fundus are 85 mm, 178 mm and 242 mm for the blue, red and green marks respectively.

line in the left panel of Figure 5.6), slow waves start propagating from a more aboral location compared to the case of a steeper gradient (corresponding to the blue line in the left panel of Figure 5.6).

5.6 Summary of One Dimensional Simulations

Experimental techniques involving quantitative measurements of CO concentration and simultaneous electrophysiological recordings present a variety of technical difficulties that have hindered a full understanding of the cellular mechanisms in response to different CO concentrations in the GI tract. Computational models are capable of succinctly describing cellular activity and are able to provide a unique insight to supplement the few available experimental findings. In this chapter, for example, we built upon the results of experiments that showed the ability of CO to activate K^+ currents in the GI tract and incorporated this information into two biophysically based cellular models of ICC and SM cell. The equations describing voltage dependent K^+

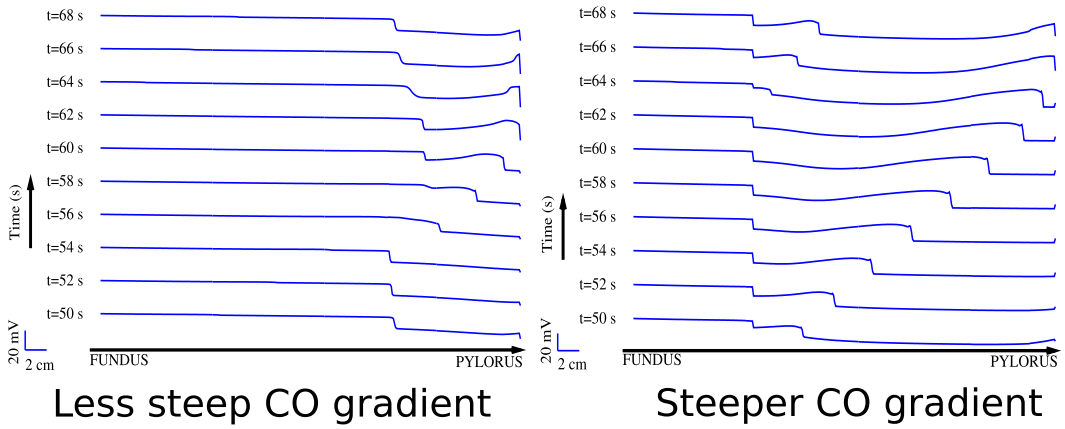

Figure 5.7: Propagation of slow waves with different CO gradients. The control case is the one described in Figure 5.4. Left panel shows the case of a CO gradient that is less steep than the control case (and corresponds to the green line in the left panel of Figure 5.6) while the right panel shows the case of a steeper gradient (and corresponds to the blue line in the left panel of Figure 5.6).

currents in the computational models of ICC and SM cell were modified in order to take into account different CO concentrations. From the simulations presented in this chapter, it appears that CO may determine the position of the pacemaker site in the stomach. The role of CO as a potential regulator of RMP via modulation of K^+ currents had been shown experimentally (Farrugia *et al.*, 2003). Our simulation results suggest that low CO concentrations in the fundus are able to lock the membrane potential of ICC and SM cell in a depolarised state that prevents the generation of slow waves. As the CO concentration linearly increases, K^+ currents are increasingly activated in a non-linear fashion, and this produces a threshold-like phenomenon at cellular level which causes a sharp shift in the RMP in the polarised direction and results in the generation of slow waves in a short restricted area along the cable. The threshold CO concentration at which the initiation occurs appear to be

around 0.28 mM (Figure 5.6). We have also postulated the ability of different CO gradients to shift the location of the pacemaker site. When the steepness of the CO gradient was increased, the slow wave initiation site was shifted in the oral direction, while a less steep gradient shifted the slow wave initiation site in the anal direction.

The mode of action of CO has not been fully elucidated and experimental evidence on different tissues has resulted in contradictory conclusions. While in vascular smooth muscle cells an influence on Ca^{2+}-activated K^+ channels channels has been proposed (Wang & Wu, 1997; Xi *et al.*, 2004), augmentation of voltage dependent K^+ currents was proposed in the GI musculature (Farrugia *et al.*, 1998). Here, the effect of CO on the ion channels of ICC and SM cells was modelled according to experimental evidence from the canine jejunum (Farrugia *et al.*, 1998) as we assumed CO affected voltage dependent and not Ca^{2+}-activated K^+ channels (BK). This choice was also motivated by the apparent effect of CO as regulator of the RMP in the GI tissue. BK channels are primarily activated after Ca^{2+} entry through voltage dependent Ca^{2+} channels on the plasma membrane and this, for the most part, does not occur under resting conditions. BK channels were proposed to play a role in modulating the plateau potentials in SM cells (Carl *et al.*, 1996) and our previous simulation results on our gastric SM cell model seem to confirm the influence of BK channels on the plateau potential of the slow waves and not on the RMP (Corrias & Buist, 2007).

Chronotropic mechanisms in the ICC network have been object of increasing interest over the past few years (Sanders *et al.*, 2006a). When studied in

isolation, ICC from different regions of the stomach pace at different frequencies. The existence of this frequency gradient along the longitudinal axis of the stomach has been shown in both dogs (Szurszeswski JH, 1987) and guinea-pigs (Hirst & Edwards, 2006). In the whole intact stomach, on the other hand, there appears to be one dominant frequency suggesting the existence of an entrainment mechanism (Hirst & Edwards, 2006). It has recently been proposed that this entrainment mechanism depends on Ca^{2+} entry through DHP-resistant pathways (Ward *et al.*, 2004). The modelling framework presented here has been designed to incorporate both the frequency gradient of isolated ICC as well as the Ca^{2+}-dependent coordination mechanism of entrainment. It should be noted that in a computational formulation, the existence of an intrinsic frequency gradient of the pacing cells in different location is essential if one wishes to realistically simulate the propagation of the slow waves from one point of the stomach to another. In fact, without such frequency gradient, all cells would activate at exactly the same time, giving raise to an unrealistic simultaneous activation of the whole stomach. We were able to regulate the intrinsic ICC frequency by tuning the value of the intracellular IP3 concentration. IP3 has been proposed as a regulator of slow wave frequency in the murine stomach (Kim *et al.*, 2003) and small intestine (Malysz *et al.*, 2001), although it remains unclear whether the existing frequency gradient in the stomach is achieved through different concentrations of IP3 or by other means. If the latter turns out to be the case, the cellular models used here should be modified to incorporate the newly found mechanism, nevertheless the predictions on the effects of CO on the location of the pacemaker site will remain substantially

valid because they are based on the membrane nonlinearities caused by K^+ currents and not by the frequency of slow wave generation.

Our choice, in this chapter, of conducting simulations in a one-dimensional situation is motivated by our primary interest to investigate the effects of a physiological property (CO concentration) as it changes longitudinally along the stomach. One-dimensional simulations are sufficient to capture the required information in this situation and, compared to two- or three-dimensional simulations, are computationally more efficient. Nevertheless, incorporating cellular activity into a realistic three dimensional description of the stomach may reveal other important functions of CO as well as other biomolecules. Three dimensional simulations may be able to capture other important physiological observations and help in a better understanding of their physiological significance. Chapter 6 will discuss the implementation of such a three dimensional modelling framework based on the two cellular models previously discussed.

Chapter 6

Whole Stomach Simulations

6.1 Introduction

After developing single cell models of the electrically excitable cells in the stomach (SM cell and ICC), the study of the propagation of gastric electrical activity throughout the stomach constitutes the next logical step towards the development of a fully integrated multiscale modelling framework. The incorporation of ICC and SM cell models into a realistic stomach geometry will be discussed in this chapter.

6.2 Geometry of the Stomach

The geometry of a human stomach had previously been digitised from photographic images from the Visible Human Project (see Section 1.4.3 and Pullan *et al.* (2004)). Data points were created from the images (Figure 2.8) and an initial bilinear surface mesh was created. Iterative procedures were then

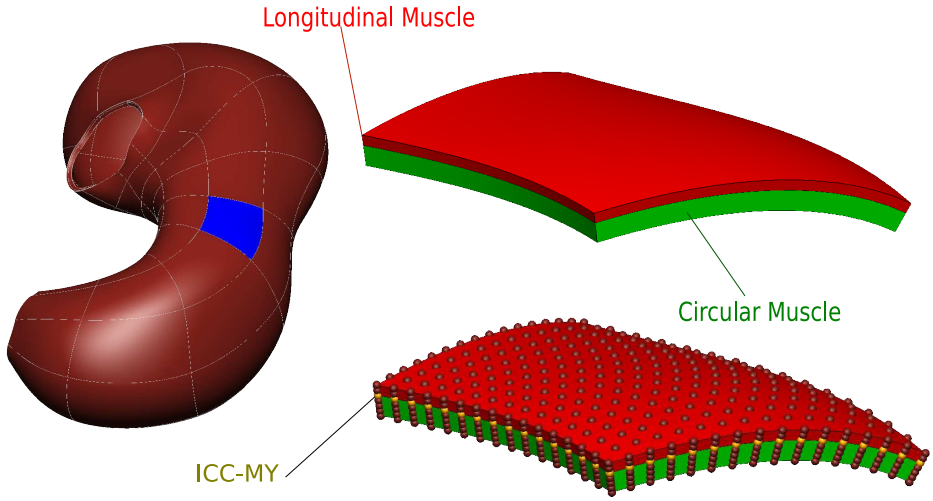

Figure 6.1: Geometry of the stomach: left panel shows the initial bicubic Hermite C^1 mesh describing the whole stomach. The right panel shows details of the element highlighted in blue in the left panel; above is the division between circular and longitudinal muscle layers, while the nodes of the high resolution mesh of the same elements are shown in the bottom part. The nodes belonging to the ICC-MY layer, which have been characterised with the I_{ion} term of an ICC cell (Equation 4.3) are shown in yellow.

employed to produce a bicubic Hermite C^1 continuous mesh with 72 nodes delimiting 64 elements, corresponding to the outer surface of the stomach. Starting from the coordinates of the fitted surface, here we generated the inner surfaces by normal inward projections from the outer surface. A thickness of 1.8 mm was chosen, consistent with endoscopic ultrasound measurement of the human *muscularis externa* (Huh *et al.*, 2003). This thickness was divided in two layers, a circular muscle layer (1.2 mm), a thinner longitudinal muscle layer (0.6 mm) (Figure 6.1, upper right panel). This initial discretised geometry consisted of 216 nodes that described 128 elements (Figure 6.1, left panel).

6.3 Mathematical Formulation

A continuum modelling framework was adopted, as outlined in Section 1.4.3. One such approach is the bidomain model (Figure 1.8), where the cellular components and the extracellular spaces are approximated by a continuous volume conductor that fills the volume of interest. In absence of any external stimulus, propagation of the electrical potential generated by the cells can be described by

$$\nabla \cdot ((\sigma_i + \sigma_e)\nabla\phi_e) = -\nabla \cdot (\sigma_i \nabla V_m) \tag{6.1}$$

$$\nabla \cdot (\sigma_i \nabla V_m) + \nabla \cdot (\sigma_i \nabla \phi_e) = A_m(C_m \frac{\partial V_m}{\partial t} + I_{ion}) \tag{6.2}$$

where the i and e subscripts represent intra- and extra- cellular variables respectively. The σ terms are tissue conductivities and are, in general, tensors whose values represent the local volume averaged properties of the intra- and

extra-cellular domains. Anisotropic characteristics, such as preferential conduction directions along fibres can be incorporated and accounted for in the computation of these terms. The ϕ terms are potentials, V_m is the transmembrane potential, A_m is the surface to volume ratio and C_m is the membrane capacitance. The I_{ion} term represents the summation of all the ionic currents flowing through the ion channels in the membrane of the cell in the tissue under investigation. Fine details of cellular physiology can be incorporated into the tissue description through the I_{ion} term.

If we assume the extracellular space to be highly conducing, $\nabla\phi_e$=0 and Equations 6.1 and 6.2 can be reduced to

$$\nabla \cdot (\sigma \nabla V_m) = A_m(C_m \frac{\partial V_m}{\partial t} + I_{ion}) \tag{6.3}$$

which is known as monodomain equation. It was recently shown that, for the study of propagation of cardiac electrical activity, both approaches are equally accurate (Potse *et al.*, 2006) and, having to integrate only one equation instead of two, the monodomain approach is computationally more efficient. We therefore make use of Equation 6.3 (monodomain approach) instead of Equations 6.1 and 6.2 (bidomain approach).

The coarse geometry described in Section 6.2 (Figure 6.1) is not sufficient to provide a numerically stable solution that captures cellular slow wave activity throughout the stomach geometry. Each of the 128 elements was therefore divided into a large number of smaller hexahedra. In particular, each of the 64 elements of the circular layer was divided into 900 hexaedra (15 in the longitudinal direction, 15 in the circumferential direction and 4 in the transmural

direction), while each of the 64 elements of the longitudinal layer was divided into 450 hexaedra (15 in the longitudinal direction, 15 in the circumferential direction and 2 in the transmural direction). This resulted in a new high-resolution mesh consisting of 86,400 hexaedral elements delimited by 101,640 nodes. The average spatial resolution of this mesh was 1.1 mm. Equation 6.3 was integrated by means of the finite element method over the high-resolution mesh (Buist *et al.*, 2003).

6.4 Numerical Simulations

To characterise the electrophysiology of the stomach wall, the two biophysically based cell models discussed in Chapters 3 and 4 were used. Each of the nodes in the high-resolution mesh can be thought as a continuum cell, as illustrated previously in Figure 1.8. It is therefore possible to spatially characterise the tissue with different cellular components by specifying, in Equation 6.3, different I_{ion} terms (which describe different cellular types) for each node in the high resolution computational mesh. Hence, the outer-most surface of the circular muscle layer (which corresponds to the myenteric plexus lying in between circular and longitudinal muscle layers) was characterised by being populated with only ICC cell models (Figure 6.1, bottom right), allowing a description of the ICC-MY layer. Owing to histological observations showing that ICC are also interspersed within the muscular layers of the stomach wall (Komuro, 1999), the two layers of smooth muscle cells (circular and longitudinal) were populated with both the ICC and SM cellular models in a 1:1 ratio. The final result was a geometrical model describing one ICC-MY layer sur-

rounded by two muscular layers where ICC were interspersed among SM cells, which is a realistic approximation of the actual microstructure of the gastric *muscularis externa* (see Section 1.3).

Assuming the absence of active electrical connections between SM cells (Sanders *et al.*, 2006a), the propagation of the electrical signal through the ICC network can be described by Equation 6.3, which, in the case of ICC network can be written as

$$\nabla \cdot (\sigma \nabla V_{m\_ICC}) = A_m (C_{m\_ICC} \frac{\partial V_{m\_ICC}}{\partial t} + I_{ion\_ICC}) \tag{6.4}$$

which is the multidimensional version of Equation 5.1 used to describe slow wave activity in the 1D situation. Equation 6.4 was integrated using the finite element method over the high resolution computational mesh described in Section 6.3. At each time step (0.25 ms), the computed value of V_{m_ICC} was used to calculate the value of the electrical current (I_{ext}) exchanged between ICC and SM cell

$$I_{ext} = G_{couple}(V_{m\_SM} - V_{m\_ICC}) \tag{6.5}$$

where G_{couple} is the coupling resistance between the ICC and the SM cell which was set at 1.3 nS (see Section 3.2.2) and represents the passive conductance of the gap junction between ICC and SM cells. The transmembrane potential of the SM cell was then calculated from

$$\frac{dV_{m\_SM}}{dt} = -\frac{1}{C_{m\_SM}}(I_{ion\_SM} + I_{ext}) \tag{6.6}$$

where V_{m_SM} is the SM cell transmembrane potential, C_{m_SM} is the membrane

capacitance and I_{ion_SM} is given by Equation 3.2 and represents the summation of all the ionic currents in the SM cell. We simulated a linear gradient in CO concentration from the fundus (0.05mM) to the pylorus (0.5mM) acting on the ICC and SM cell in the same way as described in Section 5.4. A gradient in the frequency of slow wave generation was also included by setting a gradient in the concentration of IP3 (from 670 nM to 600 nM) and the value of the tissue conductivity σ was chosen to be 5 μS/mm. Since each ICC is capable of spontaneously generating slow waves, a coordination mechanism that is capable of coordinating and entraining the slow waves discharge across the tissue was introduced as described in Section 5.4.

6.5 Simulation Results

Integration of Equations 6.4-6.6 over the mesh described in Section 6.3 enables the calculation of the transmembrane potential at all points in the stomach as a function of time. Figure 6.2 shows the SM membrane potential at seven different time instants. The fundus is predicted to be the most depolarised (around -43 mV) region and slow waves failed to develop in the fundus. This is consistent with many experimental observations where slow waves could not be recorded from the fundus and the value of the membrane potential was found to be -40 mV in guinea-pig gastric SM cells (Hirst & Edwards, 2006) and -45mV (Szurszeswski JH, 1987) in canine gastric SM cells. Simulated slow waves originated at the level of the mid-corpus and propagated in the anal direction with a velocity of 10 mm/s. This is also consistent with the experimental findings of Hirst & Edwards (2006) (reviewed by Sanders *et al.*

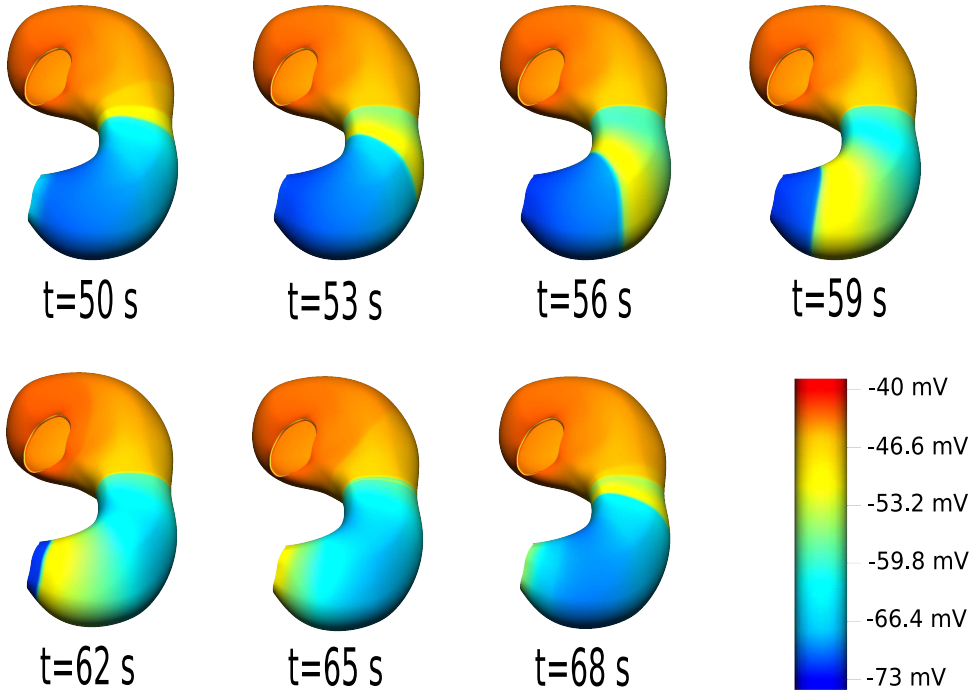

Figure 6.2: SM membrane potential on the serosal surface of the stomach at seven different time instants.

(2006a)). Similar to the one dimensional simulations, we found a characteristic non-linear behaviour of the cell membrane in presence of a linear gradient in CO concentration that caused the slow waves to originate in a relatively restricted region corresponding to the mid-corpus. Figure 6.3 shows the slow waves as a function of time from three different locations in the stomach, one in the fundus, one in the corpus and one in the antrum. Our 3D simulations capture the characteristic slow wave heterogeneity observed experimentally by placing recording electrodes in different parts of the stomach (Szurszeswski JH, 1987). In particular, our model predicts an absence of slow waves in the fundus, small slow waves of triangular shape in the corpus and bigger slow waves in the antrum, consistent with the experimental evidence (Szurszeswski JH, 1987; Hirst & Edwards, 2006).

6.6 Summary of 3D Simulations

In this chapter we presented a three dimensional model of stomach electrophysiology arising from the cellular activity of ICC and SM cells. The cellular models of Chapters 3 and 4 have been integrated into a realistic geometry of the stomach musculature where a thin layer of ICC was surrounded by a thick layer of SM cells on the mucosal side (circular layer) and a thin layer of SM cells on the serosal side. We simulated longitudinal gradients in the concentration of CO (which acts on cellular K^+ currents) and were able to simulate the generation of the slow waves around the mid-corpus as well as a realistic propagation of the slow waves towards the pylorus (Figure 6.5). To our knowledge, this is the first implementation where slow wave propagation

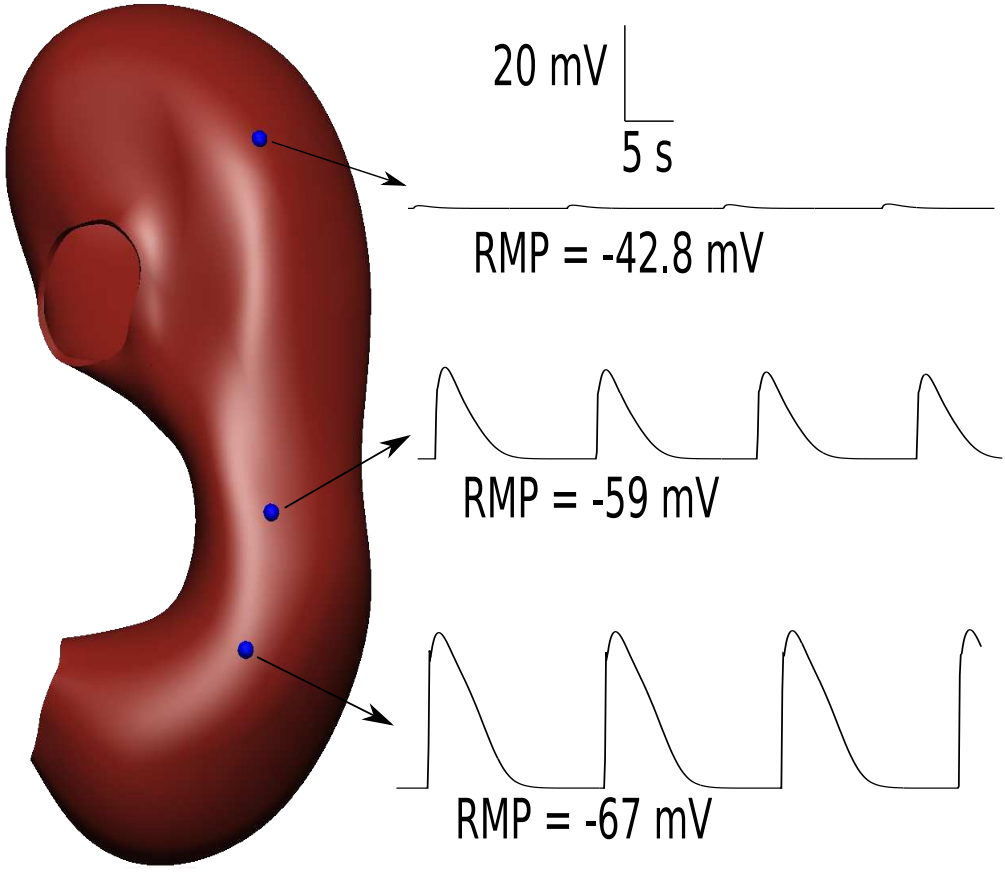

Figure 6.3: SM membrane potential as a function of time in three different locations in the stomach (indicated by blue spots), one in the fundus, one in the corpus and one in the antrum. Resting membrane potentials are -42.7 mV for the top trace (fundus), -59 mV for the middle trace (corpus) and -67 mV for the bottom trace (antrum). Scale bars apply to all traces.

throughout the stomach has been described with biophysially based cellular events as a starting point.

The mechanism of slow wave propagation has recently been the object of some discussion. In particular, the question of how each self pacing ICC could be entrained to produce a coordinated propagation pattern was raised. Experimental evidence seems to point toward a Ca^{2+}-mediated mechanism, where Ca^{2+} entry is capable of 'resetting' the internal pacemaking mechanism of each ICC and allowing the entrainment to occur (Bayguinov *et al.*, 2007; Sanders *et al.*, 2006a). Our single cell models have been adjusted to take into account this mechanism, as described in Section 5.4, by introducing a voltage dependent Ca^{2+}-entry into the submembrane space of the ICC with the aim of simulating the coordination mechanism that has been suggested (Bayguinov *et al.*, 2007). Alongside this modification, we introduced a frequency gradient along the longitudinal axis of the stomach, as described in Section 5.4, by adjusting the value of intracellular IP3 concentration (Kim *et al.*, 2003; Malysz *et al.*, 2001).

The three dimensional analysis of the gastric slow waves presented here is seen as a first step towards the establishment of modelling as a predictive tool in gastric pathophysiology and it is possible to identify several areas of future improvement that might help in this process. As far as the tissue characterisation is concerned, we assumed a homogeneous distribution of cells across the stomach; we also assumed a uniform thickness of the gastric *muscularis externa*. Few studies provide an investigation into the microstructure of the gastric musculature and its inhomogeneous nature (Komuro, 2006, 1999). No

specific functions for these inhomogeneities have been proposed and, once a precise characterisation of the tissue microstructure becomes available, it will be interesting to modify the existing geometry to incorporate the inhomogeneous nature of the gastric *muscularis externa* and infer its functions. Moreover, our simulated distribution of CO is a simplified one as we only included a longitudinal gradient. This choice was primarily due to our interest in the longitudinal propagation of the slow waves, in view of the longitudinal propagation of the peristaltic contractions that are regulated by the underlying slow wave activity. Nevertheless, it has been shown that a CO gradient also exists across the circular muscle layer of the stomach (Farrugia *et al.*, 2003) and it would be interesting to introduce this further gradient into the 3D modelling framework and make predictions regarding its physiological significance.

Integration of Equation 6.4, where the I_{ion} term takes into account complex cellular processes at each time step, is computationally demanding, especially if performed over such a large domain such as the whole stomach with a necessarily small time step. While the trade off between computational efficiency and the level of detail in the cellular model must be always taken into account, this should not hinder the inclusion of more detailed models of ion channel kinetics or relevant intracellular processes into the cell models and into the three dimensional modelling framework presented here. In this thesis, we will examine one such example where a more detailed formulation of a Na^+ channel will be discussed (Chapter 8).

The significance of the results obtained in this chapter are twofold. Firstly, this is the first three dimensional model of the stomach where detailed cel-

lular models that are able to capture the biophysics of the ion channels and intracellular dynamics are included into a realistic 3D geometry. Previous attempts made use of simplified phenomenological descriptions of the cellular behaviour (Pullan *et al.*, 2004) and could not be used to evaluate the effects of cellular abnormalities on the three dimensional propagation of the slow waves. Secondly, by implementing 3D simulations of the electrical activity, it is then possible to analyse the electrical field generated by the cellular activity in the stomach as it appears on the torso surface. This analysis will be discussed in Chapter 7.

Chapter 7

Torso Simulations: the EGG

7.1 Introduction

Electrogastrography is a clinical technique that makes use of electrodes positioned on the abdominal skin surface to record rhythmic gastric myoelectricity. The Federal Drug Administration (FDA) approved EGG as a test for patient evaluation in 2000 (Parkman *et al.*, 2003). This non-invasive technique is potentially capable of providing valuable information about frequency, amplitude and propagation of gastric slow waves. Many investigators have proposed the EGG as a useful diagnostic tool for a variety of maladies including diabetic gastropathy (Koch, 2001; Kaji *et al.*, 2007), Crohn's disease (Kohno *et al.*, 2006) and functional dyspepsia (Zhang *et al.*, 2006). The clinical ability of the EGG to discern between different GI symptoms was recently evaluated in a large cohort of patients with upper gastrointestinal diseases including reflux disease, active gastric ulcer and functional dyspepsia and symptoms of early satiety and nausea (Chen *et al.*, 2006). EGG proved to be useful in differen-

tiating between subgroups of patients with nausea or early satiety, but it was unable to differentiate between reflux disease, gastric ulcer and functional dyspepsia. Other investigators have cast doubts on the reproducibility and clinical usefullness of this technique (Abid & Lindberg, 2007). The gastric section of the American Motility Society has recently set up a Testing Task Force (TTF) with the aim of developing a consensus opinion regarding the clinical utility of the EGG. In the final report of their activity, the TTF suggests that '*EGG can be obtained: (i) to define gastric myoelectric disturbances in patients with nausea and vomiting unexplained by other diagnostic testing or associated with functional dyspepsia and (ii) to characterise gastric myoelectric disturbances associated with documented gastroparesis.'* (Parkman *et al.*, 2003).

The obstacles that EGG needs to overcome in order to gain useful insights into gastric pathophysiology are of a diverse nature. Technological hurdles linked to the weakness of the signal and the high background noise have been addressed in recent years by improving the impedance of the recording electrodes (Kasicka-Jonderko *et al.*, 2006) and by employing better signal processing techniques (Sobral Cintra *et al.*, 2004). The main challenge that this technique needs to address is, however, the identification of correlations between EGG signal variations and pathological conditions (Chang, 2005; Abid & Lindberg, 2007). Despite the work of the TTF, little is known about how to diagnose cellular abnormalities from abnormal EGG recordings. Multi-scale mathematical models have already helped in linking ECG tracings to cellular abnormalities (Pullan *et al.*, 2005). A realistic model of stomach electrophysiology is therefore possibly the only way to rapidly determine such correlations.

This chapter is devoted to describe the simulation of the electrical field generated in the stomach at cellular level on the surface of the human torso and the extrapolation of simulated EGG tracings.

7.2 Mathematical Formulation

The extrapolation of the simulated EGG signals was performed following the approach proposed by Pullan *et al.* (2004). Equation 6.3 allows the calculation of the electrical potential generated by the ICC (V_{m_ICC}) in every element in which the stomach has been discretised. Given the values of V_{m_ICC} as a function of space and time, equivalent current sources $\mathbf{J}$ that would generate the same far-field electrical activity were defined as

$$\mathbf{J} = -\sigma \nabla V_{m\_ICC} \tag{7.1}$$

where σ is the stomach tissue conductivity. A total of 128 current sources were calculated, one for each of the elements in the initial mesh. The calculation of the electrical field generated by the current sources is a classical physics problem and is described by a Poisson equation

$$\nabla \cdot (\sigma_o \nabla \phi) = \nabla \cdot \mathbf{J} \tag{7.2}$$

where σ_o is the conductivity of the passive volume conductor (torso) outside the active region (stomach). During a typical solution, at each time step, three calculations are performed. First, V_{m_ICC} is calculated from the cellular

models. Second, the equivalent current sources are calculated using Equation 7.1. Finally the potential ϕ throughout the torso is calculated by integrating Equation 7.2 over the geometry of the torso.

7.3 Torso Geometry

The geometry of the human torso has been digitised from photographic images within the Visible Human Project (Spitzer *et al.*, 1996) as illustrated in Pullan *et al.* (2004). Data points were obtained from axial slice images 5 mm apart from each other. For each slice, the data points described the contour of the torso were obtained. A computational mesh was fitted to the three dimensional data points obtained by stacking data points from each slice on top of the other. An iterative linear fitting procedure proposed by Pullan *et al.* (2004) was used to obtain 300 surface elements, delimited by 290 nodes (Figure 7.1). Equation 7.2 was integrated over such geometry by means of the boundary element method (Bradley *et al.*, 1997, 2001). The boundary element method is generally preferred to the finite element method (like the one employed in Chapter 6) when (i) the area of interest is confined to a certain surface and not to the entire volume in the domain of the problem and (ii) the domain of the problem is assumed homogeneous and isotropic. Under such conditions, the boundary element method allows, compared to the finite element method, a more efficient solution of Equation 7.2. In this chapter the primary interest is focused in evaluating the electrical field on the surface of the torso. Moreover, the volume conductor of the torso was assumed to be electrically homogeneous and isotropic and characterised by a conductivity of

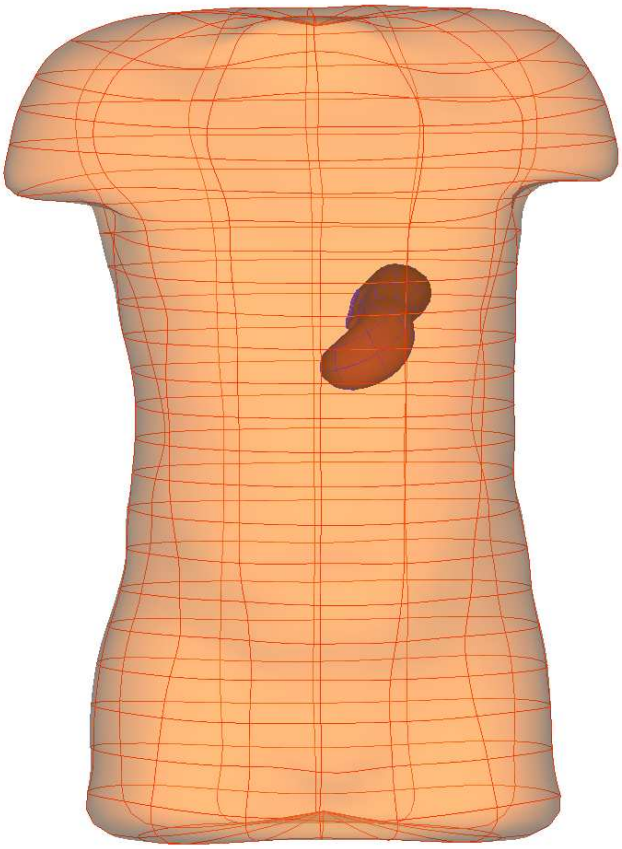

Figure 7.1: Illustration of the digitised human torso (300 boundary elements) and the position of the stomach within the torso.

50 μS/mm, a value compatible with the conductivity of the tissues separating the stomach from the skin (lungs and fat) (Hunt & de Jongh Curry, 2004). Therefore both conditions under which the use of boundary element method is preferred were satisfied and the boundary element method was adopted to solve Equation 7.2.

7.4 Simulation Results

The distribution of electrical potentials on the surface of the torso at ten different time instants is shown in Figure 7.2. This was obtained by integrating Equation 7.2 over the domain described in Section 7.3. As expected, the bulk of electrical activity occurs on the abdomen just over the stomach. The periodic slow wave activity generated by the cellular models within the gastric tissue can be recognised at skin level on the torso, showing a correspondence between internal events and simulated skin level recordings. To reinforce this observation, Figure 7.3 shows, at four different time instants, the electrical potentials on the surface of the stomach (left panel), on the torso surface (middle panel) and the simulated EGG recording obtained from a unipolar electrode in correspondence of the stomach (green spot indicated in middle panel). Three waves can be identified in the 60 seconds period between 20 and 80 seconds displayed in Figure 7.3 (right panel), in agreement with a dominant frequency of 3 cpm experimentally obtained in EGG recordings (Hamilton *et al.*, 1986).

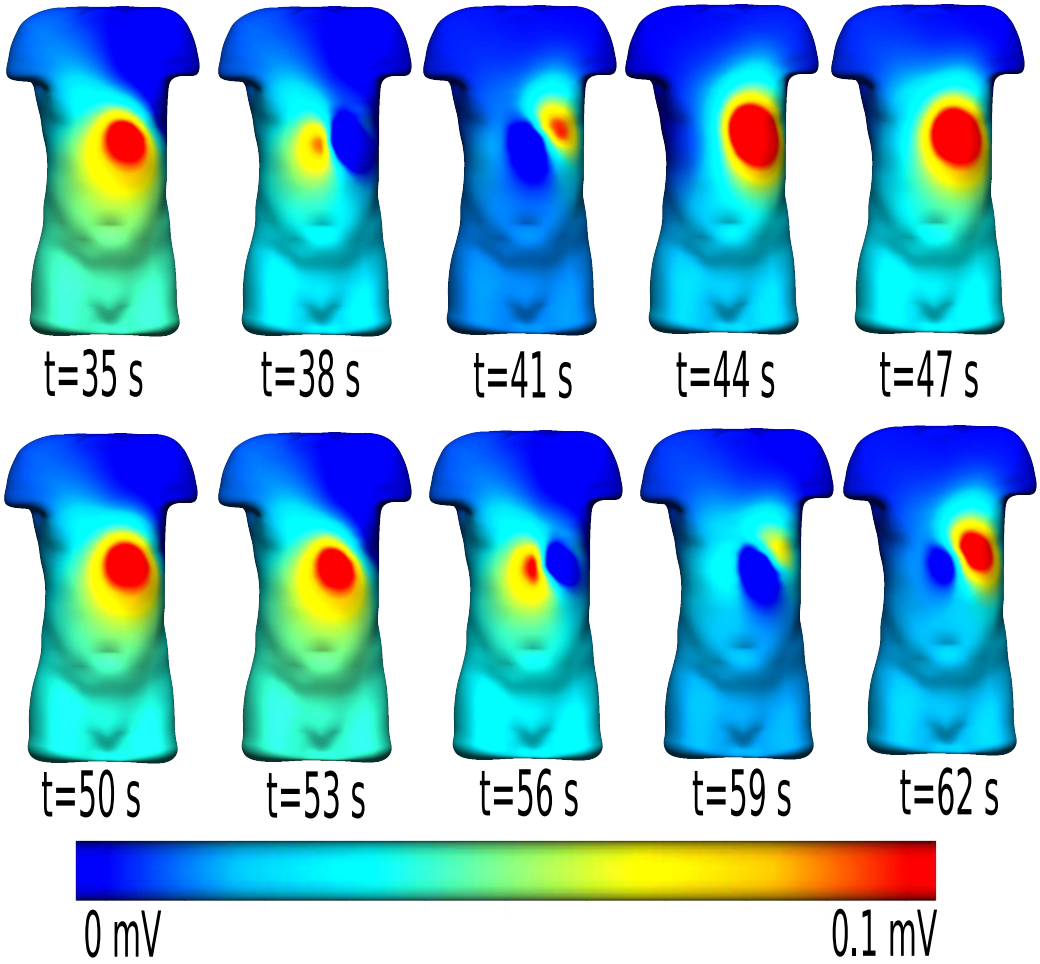

Figure 7.2: Torso potentials at ten different time instants showing periodic electrical activation at skin level originated from the cellular activity within the stomach. Scale bar applies to all traces.

7.5 Summary of Torso Simulations

In this chapter we have presented an example of the results of calculating the electrical potential field generated by the stomach on the surface of a simplified virtual human torso. The novelty of the results presented here is primarily constituted by the fact that the electrical field that is calculated on the torso is generated by the realistic biophysically based cellular models described in Chapters 3 and 4. Previous attempts at modelling EGG signals (Buist *et al.*, 2004) were based on a phenomenological description of the electrical activity generated by ICC in the stomach. We have compared our simulated EGG signals with experimental recordings in the fasting state and found good correspondence in terms of the frequency (3 cpm) (Hamilton *et al.*, 1986) and amplitude of the signals (around 0.1 mV) (Chang, 2005).

As this is the first implementation of a cell-to-body-surface link in gastric electrophysiology based on realistic cellular descriptions, significant improvements may be achieved in the future. For example, the assumption that the human torso was an electrically homogeneous volume conductor may be substituted with a more accurate description of the conductivity as a function of position within the torso that takes into account details of anatomical structures. From the computational point of view, we have calculated one equivalent current source per geometric element (for a total of 128). Nevertheless, the optimal number of sources has yet to be determined. It is possible that a realistic EGG signal might be reconstructed by a smaller number of sources thus lessening the computational burden of the simulation. On the other hand, a higher number of sources might be required for capturing finer physiological

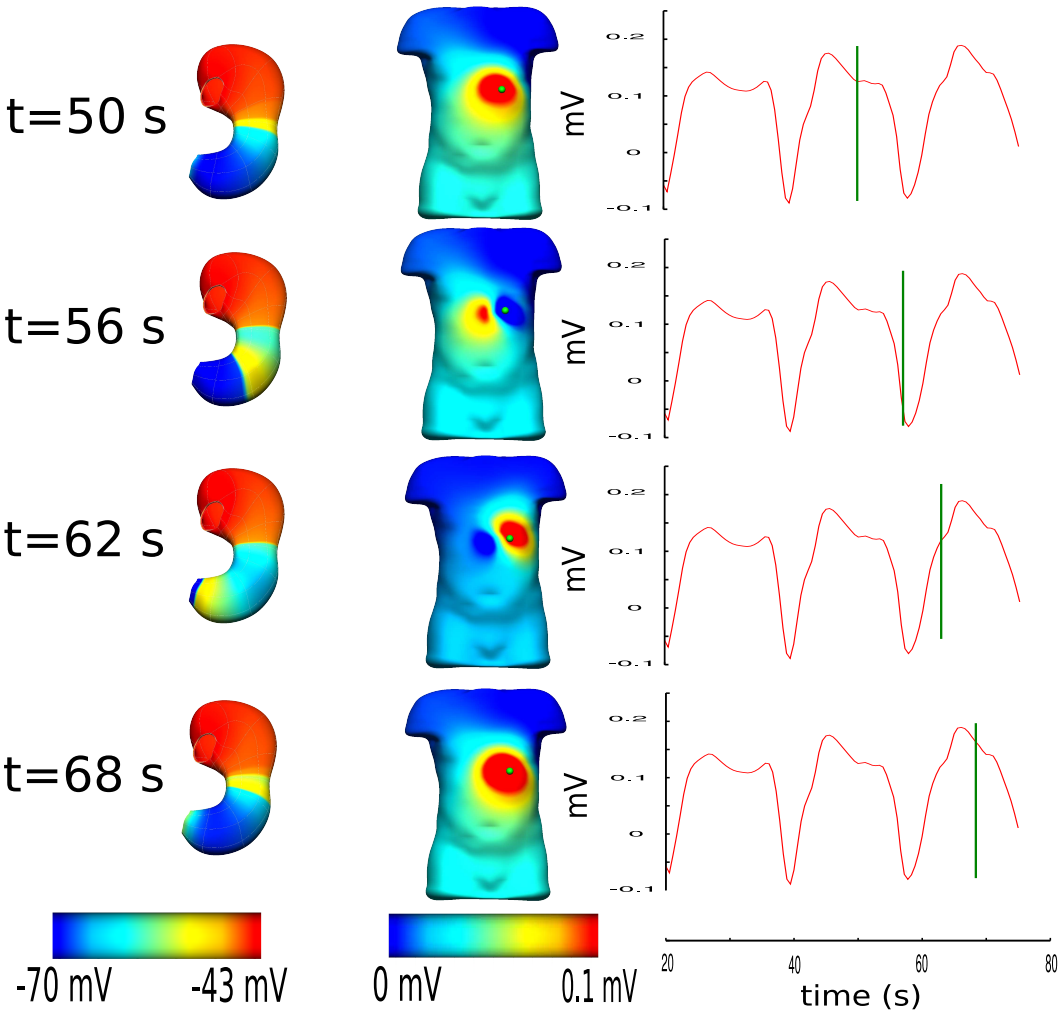

Figure 7.3: The left panel shows the SM cell membrane potential on the surface of the stomach at four different time instants. The middle panel displays the corresponding torso potentials. The right panel shows a simulated unipolar EGG recording from an electrode placed in the location indicated by the green spot on the torso. The green bar on the EGG recording in the right panel indicates the four time instants corresponding to the electrical potentials of the left and middle panels.

details allowing a more accurate diagnosis. Further investigations, possibly targeted at specific disease states, are needed to elucidate this aspect.

Moreover, a more rigorous validation of the multiscale process that leads to the simulation of an EGG from cellular activity is required. In particular, the cellular models that we used are validated against animal data: canine recordings for the SM cell model (Figure 3.5) and guinea-pig recordings for the ICC model (Figure 4.7). In this chapter, these two models are used to produce a human EGG. This discrepancy would ideally be addressed by the implementation of human cellular models but this is currently hindered by a scarcity of electrophysiological data obtained from human GI cells.

The results presented in this chapter are for a normal healthy subject. As mentioned above, one of the main challenges that EGG faces is the correlation between abnormal EGG signals and a particular disease state. Our modelling framework is suitable for capturing abnormal cellular behaviour and investigating its effect at tissue and organ level. It is therefore possible to simulate the EGG in a diseased state where the genetic origin is known. A preliminary investigation of this type is presented for the Na^+ channel-encoding SCN5A gene in Chapter 8.

Chapter 8

Linking Genotype to Phenotype: the SCN5A Gene

8.1 Introduction

This chapter presents an example application of the modelling framework developed in this thesis by implementing a multi-scale mathematical description of the effects of a genetic mutation affecting the SCN5A-encoded Na^+ channel expressed in GI SM cells and ICC.

Over 100 SCN5A mutations have been reported over the last few decades (Ackerman *et al.*, 2004; Locke *et al.*, 2006). Most of these mutations affect the cardiac SCN5A gene and some have been linked to a congenital form of long-QT (LQT) syndrome (Dumaine *et al.*, 1996) as well as to Brugada syndrome (Antzelevitch & Yan, 2000), both of which may result in life threatening cardiac arrhythmias. One of the most severe syndromes is type 3 of the long QT syndrome (LQT3), caused by a gain-of-function mutations of the Na^+ chan-

nel. Loss-of-function mutations have been associated with Brugada syndrome (Dumaine *et al.*, 1999).

A recent epidemiological study provided evidence supporting a correlation between SCN5A-encoded cardiac channelopathies and the onset of GI symptoms (Locke *et al.*, 2006). Over 65% of patients with an SCN5A-encoded cardiac channelopathy also reported one or more typical GI symptoms including abdominal pain, constipation and dyspepsia. The most frequent of these symptoms, abdominal pain, was reported by 50% of the patients compared to only 13% in the control group. In this epidemiological study, both patients with LQT3 and Brugada syndrome were included, the majority of them being affected by LQT3. The mechanisms through which these symptoms occur are rather unclear and, therefore, no targeted therapeutic approach is available. SCN5A encodes a TTX-resistant Na^+ conductance that is expressed in SM cells and ICC in the GI tract (Ou *et al.*, 2002; Strege *et al.*, 2003). Studies on its molecular structure revealed a 99% homology with its cardiac counterpart, the only difference being a single amino acid substitution (glutamine instead of histidine) (Holm *et al.*, 2002). This Na^+ conductance appears to be mechanosensitive and is expressed in humans and dogs, but not in pigs or guinea-pigs (Strege *et al.*, 2007). One of the factor that hinders further developments in therapeutic approaches for the SCN5A channelopathy is the lack of understanding of the function of Na^+ currents in the electrophysiology of ICC and SM cells. The modelling approach proposed here is therefore particularly suitable for investigating the effects of a Na^+ channel mutation on gastric physiology.

One notable SCN5A gene mutation, known as 1795insD, causes an insertion of aspartic acid at the C terminus of the Na^+ channel protein. Clinically, the 1795insD mutation was associated with both long QT syndrome and Brugada syndrome. The fact that one single mutation underlies the onset of both clinical conditions is seemingly paradoxical because long QT syndrome has been associated with Na^+ channel gain-of-function mutations while Brugada syndrome with loss-of-function mutations. The modelling work of Clancy & Rudy (2002), based on a Markovian formulation of the Na^+ channel, helped to clarify this apparent paradox by showing that the heterogeneous expression of Na^+ channels within the myocardium provided different physiological substrates upon which the 1795insD mutation caused different phenotypes. In this chapter, the effects of the 1795insD mutation on GI electrophysiology will be evaluated at different scales of investigation.

8.2 Single Channel Models

8.2.1 Hodgkin and Huxley Formulation

The cellular models of ICC and SM cell developed in Chapters 3 and 4 contain a description of the wild type Na^+ channels based on electrophysiological patch clamp experiments. The Na^+ current was described by a Hodgkin-Huxley (HH) type equation:

$$I_{Na} = G_{Na} * d_{Na} * f_{Na} * (V_m - E_{Na}) \tag{8.1}$$

where V_m and E_{Na} are the transmembrane potential and Nernst potential respectively. G_{Na} was tuned to replicate the magnitude of the currents elicited in voltage clamp experiments (see Figure 4.6). d_{Na} and f_{Na} are the voltage dependent gating variables and represent the activation and inactivation properties of the ion channels. In both the SM model and the ICC model d_{Na} and f_{Na} are described with the Hodgkin and Huxley formalism

$$\frac{d(d_{Na})}{dt} = \frac{d_{Na\infty} - d_{Na}}{\tau_{d\_Na}} \tag{8.2}$$

$$\frac{d(f_{Na})}{dt} = \frac{f_{Na\infty} - f_{Na}}{\tau_{f\_Na}} \tag{8.3}$$

where $d_{Na\infty}$ and $f_{Na\infty}$ represent the steady state values of the gating variables, and τ_{d_Na} and τ_{f_Na} are the time constants.

For the SM cell, the voltage dependence of $d_{Na\infty}$ and $f_{Na\infty}$ was measured directly in human jejunal SM cells and therefore the Boltzmann equations proposed in Holm *et al.* (2002) were adopted

$$d_{Na\infty} = \frac{1}{1 + e^{\frac{V_m - V_{half}}{k}}} \tag{8.4}$$

$$f_{Na\infty} = \frac{1}{1 + e^{\frac{V_m - V_{half}}{k}}} \tag{8.5}$$

where V_{half} was found to be -48 mV and -78 mV for $d_{Na\infty}$ and $f_{Na\infty}$ respectively and k was -4.8 mV and 3 mV respectively. Equations 8.4 and 8.5 are displayed in Figure 8.1. As mentioned in Section 3.2.2, the equation for the activation time constant τ_{d_Na} was obtained by fitting data at -60 mV and 0 mV extrapolated from time-to-peak measurements (Huang *et al.*, 1999). Its

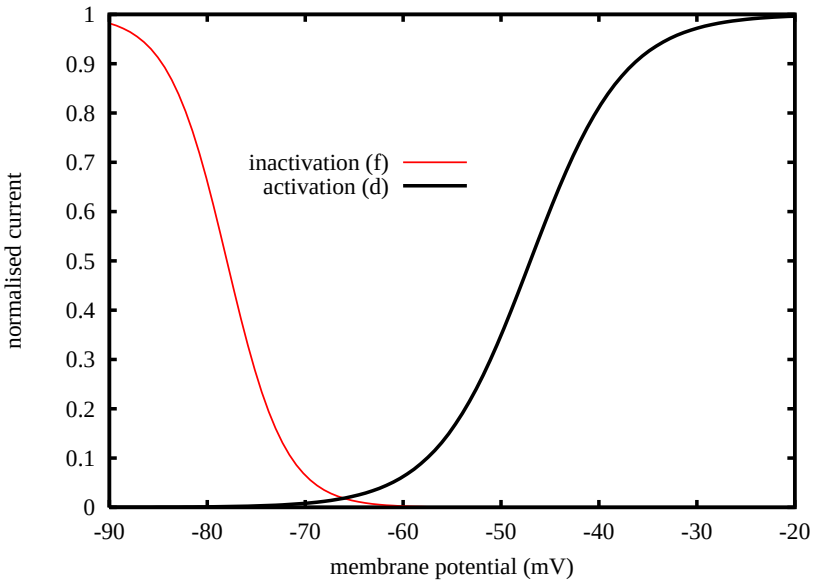

Figure 8.1: Steady-state curves for the gating variables d_{Na} and f_{Na} as measured in human jejunal SM cells (adapted from Holm *et al.* (2002)). Note the window current at potentials near the RMP.

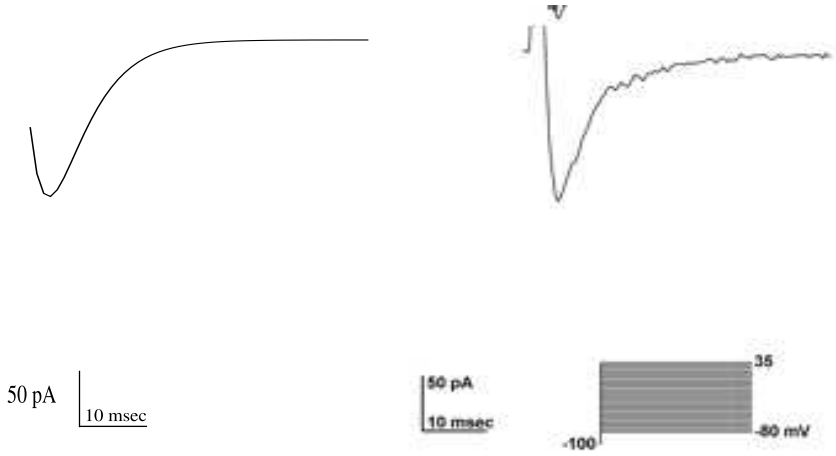

Figure 8.2: Simulated (left panel) and experimentally recorded (right panel) Na^+ current trace with the voltage clamped at -30 mV. Right panel is adapted adapted from Figure 3 of Strege *et al.* (2003).

voltage dependence was described by

$$\tau_{d\_Na} = -0.017 * V_m + 0.44 \tag{8.6}$$

Similarly, the inactivation time constant was fitted to data at -50 mV and -10 mV (Huang *et al.*, 1999) by

$$\tau_{f\_Na} = -0.25 * V_m + 5.5 \tag{8.7}$$

Time constants were adjusted to 37°C using a Q_{10} of 2.45, a value obtained by comparison of inactivation time constants at 10°C and 21°C measured in freshly dispersed cells from the rat gastric fundus (Muraki *et al.*, 1991). For the ICC, there have been no direct measurements of $d_{Na\infty}$ and $f_{Na\infty}$. Nevertheless, as mentioned in Section 4.2.3, Na^+ currents have been measured in ICC (Strege *et al.*, 2003). The parameters to characterise d_{Na} and f_{Na} have been tuned to replicate voltage clamp experiments (Strege *et al.*, 2003) as shown in Figure 4.6. In particular, V_{half} was chosen to be -48 mV and -78 mV for $d_{Na\infty}$ and $f_{Na\infty}$ respectively and k was -4.8 mV and 7 mV respectively. τ_{d_Na} and τ_{f_Na} were assumed constant and chosen to be 3 ms and 1.6 ms. With this set of parameters for the ICC Na^+ channel we were able to reproduce both experimental I-V plot of peak currents (Figure 4.6) as well as the current trace obtained with the voltage clamped at -30mV (Figure 8.2).

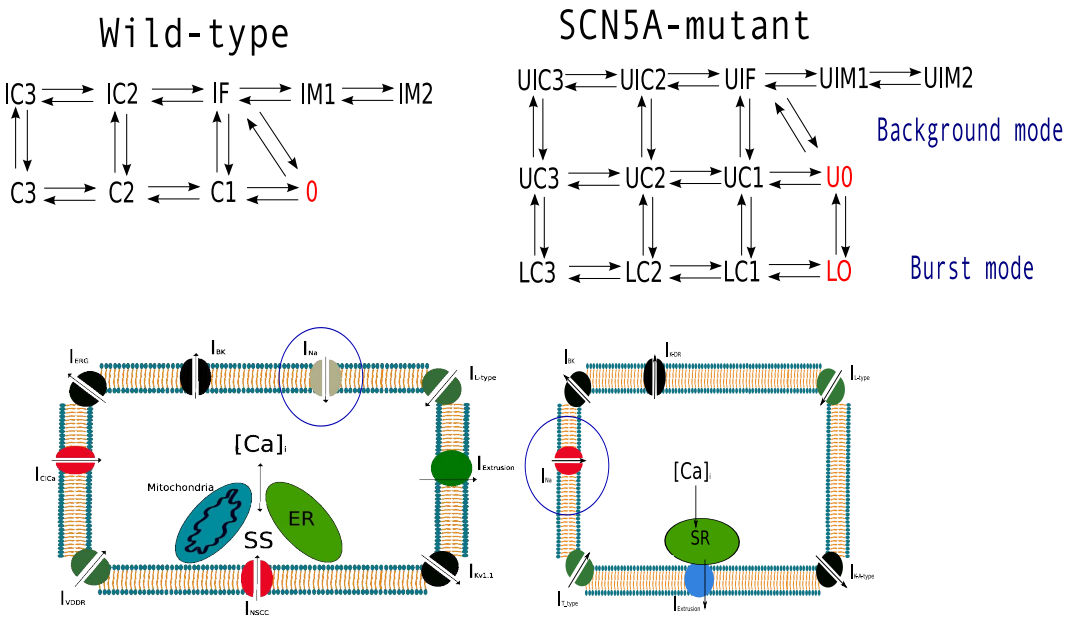

Figure 8.3: Markovian model of the mutant SCN5A-encoded Na^+ channel as proposed by Clancy & Rudy (2002) (upper panel). In the Markovian states, the letter U indicates a background mode, I denotes an inactivated state, F is for fast and S is for slow and M for intermediate. C denotes a closed state and O an open state. The lower panel shows the two cell models where the Na^+ channels are included.

8.2.2 Markovian Models

Markovian models of ion channel activity have been developed with the aim of describing the biophysical conformational states in which a given ion channel protein can be found. Typically, a Markovian model is defined by a number of physical states and the set of equations describing the transitions between the states. The one notable application of Markovian models in ion channel physiology can be found in the work of Clancy & Rudy (1999) where the effects of a three amino acid deletion (ΔKPQ mutation) in the cardiac SCN5A gene were evaluated by means of a Markovian ion channel description. Later, a similar approach was been used for the 1795insD mutation (Clancy & Rudy, 2002). For this purpose two distinct Markovian models were developed, one for the wild-type channel and one for the mutant case.

The wild type model (Figure 8.3, top left) describes three closed states (C1, C2, and C3), five inactivated states (IC3, IC2, IF, IM1 and IM2) and one open state (O). For the 1795insD mutant, the Markovian model was developed in an attempt to replicate the experimental findings of Veldkamp *et al.* (2000). The channel was assumed to be either in a background mode or in a burst mode (Figure 8.3, top right). The model comprises a total of thirteen states, seven in the background mode (UC1, UC2, UC3, UIC2, UIC3, UF, UIM1, UIM2 and the open state UO) and four in the burst mode (LC1, LC2, LC3 and the open state LO). Transitions between states were governed by rate constants whose value was tuned to replicate the experimental results. Such a formulation was capable of capturing two important characteristic properties of the macroscopic Na^+ current that had been observed experimentally on

1795insD mutant Na^+ channels. Firstly, the mutant Na^+ channel displayed a delay in the recovery from inactivation compared to the wild type case. Secondly, the peak amplitude of the macroscopic Na^+ current was reduced compared to the wild type case. The reduction appeared to be dependent on the rate of stimulation of the cell, i.e. the heart rate.

In order to evaluate the effects of the 1795insD mutation at the whole cell level, Clancy & Rudy (2002) incorporated the two Markovian formulations of the Na^+ channel described above, one for the wild type case and one for the mutant case, into an existing electrophysiological whole cell model of a cardiac myocyte, i.e. the Luo-Rudy model (Luo & Rudy, 1994a,b; Faber & Rudy, 2000).

To elucidate the mechanisms that lead from a GI Na^+ channel mutation to the onset of clinical symptoms, ideally one would include a validated, realistic description of the GI Na^+ channel affected by the 1795insD genetic mutation into the cellular models described in Chapter 3 and 4 and compare it with the wild type case. Unfortunately, to date, there exists no functional experimental characterisation of this mutation in the GI tract, nor of any other known GI Na^+ channel mutation. As a consequence, the Markovian model of the cardiac 1795insD mutation was used. The incorporation of a cardiac ion channel model into GI cellular models raises issues regarding an appropriate comparison between wild type and mutant case. In particular, it is important to establish, for the GI cells, which formulation should be considered as the wild type reference i.e., whether the cardiac Markovian model of the wild type channel or the Hodgkin and Huxley formulation of Section 8.2.1 should be

preferred. With this in mind, three models of Na^+ currents were evaluated. The first was the classic Hodgkin and Huxley type as described by Equation 8.1. The second was the Markovian wild type case, described by

$$I_{Na\_Markov\_wt} = G_{Na} * P_O * (V_m - E_{Na}) \tag{8.8}$$

where P_O is the probability of the channel being in the open state O (Figure 8.3). The third situation was the case of the 1795insD mutation described by the Markov model

$$I_{Na\_Markov\_mutant} = G_{Na} * (P_{LO} + P_{UO}) * (V_m - E_{Na}) \tag{8.9}$$

where P_{LO} and P_{UO} are the two open state probabilities of open state in the Markovian model of the mutant channel (Figure 8.3).

8.3 Single Cell Simulations

Single cell simulations were conducted using the two cellular models of ICC and SM cell described in Chapters 3 and 4 and the three formulations of I_{Na} (Equations 8.1, 8.8 and 8.9) were compared. The approach used is the same as in Chapters 3 and 4. Briefly, the membrane potential of the two cells (V_{m_ICC} and V_{m_SM}) was computed by solving the following set of equations (see Section 1.4.1 for the rationale)

$$C_{m\_ICC}\frac{dV_{m\_ICC}}{dt} = -I_{ion\_ICC} - I_{ext} \tag{8.10}$$

$$C_{m\_SM}\frac{dV_{m\_SM}}{dt} = -I_{ion\_SM} + I_{ext} \tag{8.11}$$

where the C_m terms are membrane capacitance terms. I_{ext} is the current exchanged through the gap junction channel and is given by

$$I_{ext} = G_{couple} * (V_{m\_ICC} - V_{m\_SM}) \tag{8.12}$$

where G_{couple} is the coupling conductance whose value was fixed at 1.3 nS (see Section 3.2.2). The characterisation of the SCN5A channel described by Equations 8.1, 8.8 and 8.9 was incorporated into the cell models through alterations of the I_{ion} term. The Na^+ current was expressed by a linear combination of wild type (WT) and mutant channels as follows

$$I_{ion(ICC)} = I_{L-type\_ICC} + ...(\text{other currents})... + kI_{Na\_WT} + (1-k)I_{Na\_mutant} \tag{8.13}$$

$$I_{ion(SM)} = I_{L-type\_SM} + ...(\text{other currents})... + kI_{Na\_WT} + (1-k)I_{Na\_mutant} \tag{8.14}$$

where k represents the fraction of channels affected by the genetic mutation. The case of k=1 represents a complete wild type situation while k=0 represents a situation where all the ion channels that the cell expresses are mutant. I_{Na_WT} was given by either Equation 8.1 for the HH case or Equation 8.8 for the wild type Markovian model and I_{Na_mutant} was given by Equation 8.9. Figure 8.4 shows the ICC transmembrane potential (upper panel) and corresponding whole cell I_{Na} for these three cases. In the Markovian formulation, whole cell Na^+ currents for the wild type case has a larger peak amplitude

and inactivated slightly faster than the 1795insD mutant case. Nevertheless, these differences did not have any significant impact on the slow wave profile. The reasons for this can be better understood by observing that in the Markovian formulations, whole cell Na^+ currents are nearly zero during the resting phase between slow waves (RMP), while in the HH formulation, there is a persistent window current during the resting phase of the slow wave that has a significant impact on the cell RMP. The Na^+ currents in the Markovian formulations activate only during the active phase of the slow waves (see the red and blue lines in the lower panel of Figure 8.4), where a variety of other cellular currents of bigger amplitude are also activated and offset the influence of the Na^+ current. The result is a very limited effect of the mutation on the slow wave profile in the Markovian formulations.

The discrepancy between the different behaviours of the two wild type formulations can possibly be interpreted by observing that the HH formulation (Section 8.2.1) was developed and validated according to the electrophysiological characteristics of Na^+ currents in the GI tract; in particular, the ion channel kinetics were modelled to replicate the window current that was observed experimentally at membrane potentials near the RMP (see Figure 8.1 and Strege *et al.* (2003)). On the other hand, the Markovian wild type formulation describes a cardiac cell, where, at potentials near the RMP of stomach cells, the Na^+ currents are completely inactivated, hence the shift in the RMP observed when passing from the HH to the Markovian formulation. These differences are in contrast to the similarity of the underlying amino acid structure. Interestingly, the results obtained with the Markovian formulations are

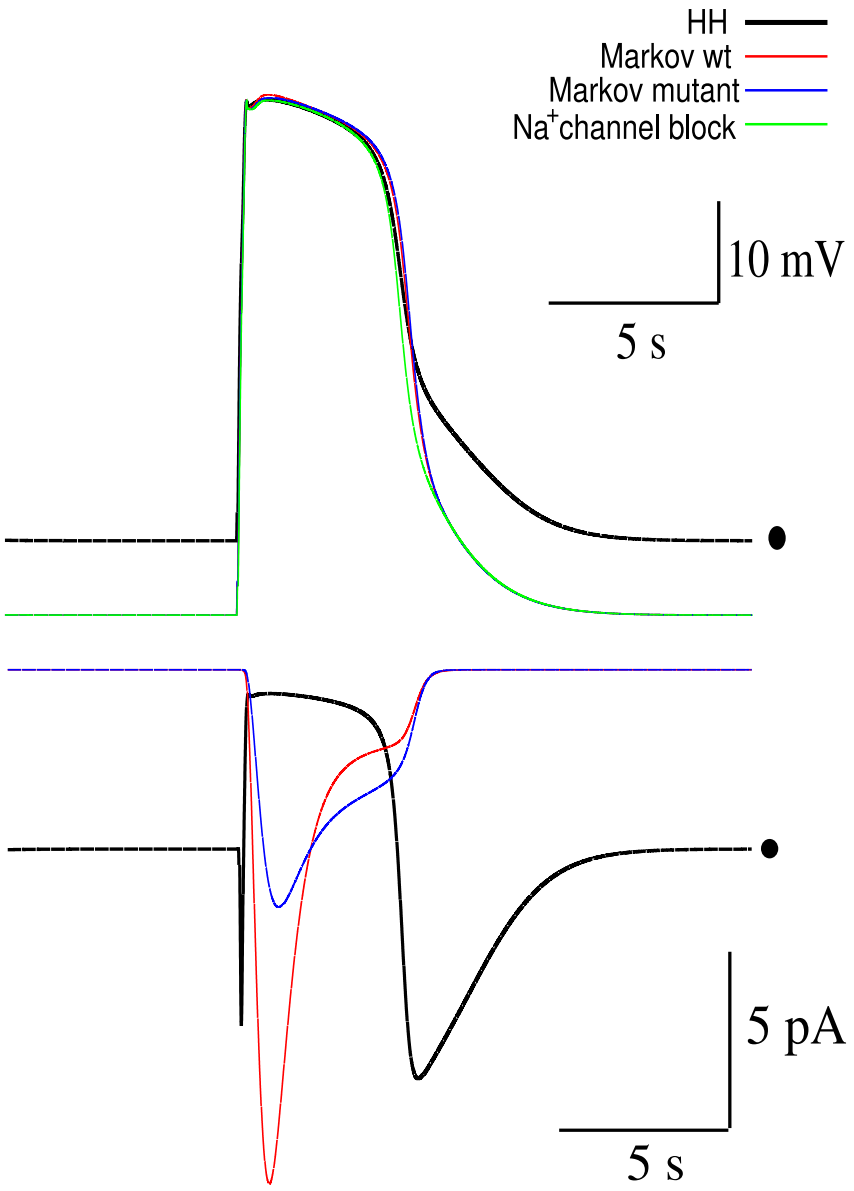

Figure 8.4: Upper panel: ICC membrane potential as a function of time in wild type conditions (black line for the HH formulation and red line for the Markov case), with a simulated SCN5A mutation affecting the Na^+ channels (blue line) and without any Na^+ currents (green line). The RMP was shifted from -67 mV in the HH formulation of the wild type (where • is located) to -75.6 mV in the wild type Markovian formulation, in the Markovian mutant formulation and in the case of block of Na^+ currents. Lower panel: whole cell Na^+ currents for the same three situations. The baseline current for the HH wild type case (where • is located) is -5.1 pA.

very similar to the case of complete blockage of the Na^+ currents (green line in Figure 8.4). Our single cell simulation results for the case where Na^+ currents are blocked are consistent with the available experimental observations. The Na^+ channel blocker QX-314 caused a membrane hyperpolarisation of 10 mV. Similar results were obtained with the less specific blocker Lidocaine which resulted in a hyperpolarisation of 4 mV (Strege *et al.*, 2003).

Due to the similarity of effects at cellular level between the Markovian formulation of the cardiac 1795insD mutation and the case of inhibition of Na^+ currents (compare blue line and green line in Figure 8.4), and in absence of a functional characterisation of the GI SCN5A mutation, in this chapter we will employ the Markovian formulation of the cardiac 1795insD to describe a loss-of-function mutation of the GI Na^+ channel. In the remainder of this chapter, each reference to the SCN5A mutation is therefore to be intended to refer to the loss-of-function mutation of the GI SCN5A-encoded Na^+ channel simulated by the Markovian model of the cardiac 1795insD mutation. The wild type channel refers to the HH formulations included in the original model descriptions.

8.3.1 Physiological Relevance of the SCN5A Mutation

The cellular models described in Chapters 3 and 4 are able to capture a variety of indirect effects caused by an alteration in one or more of the cellular components. In this case, the effects of the SCN5A mutation on the physiology of a SM cell was examined. As intracellular Ca^{2+} is one primary initiators of a contractile response in SM cells, the level of cytoplasmic Ca^{2+} from whole cell

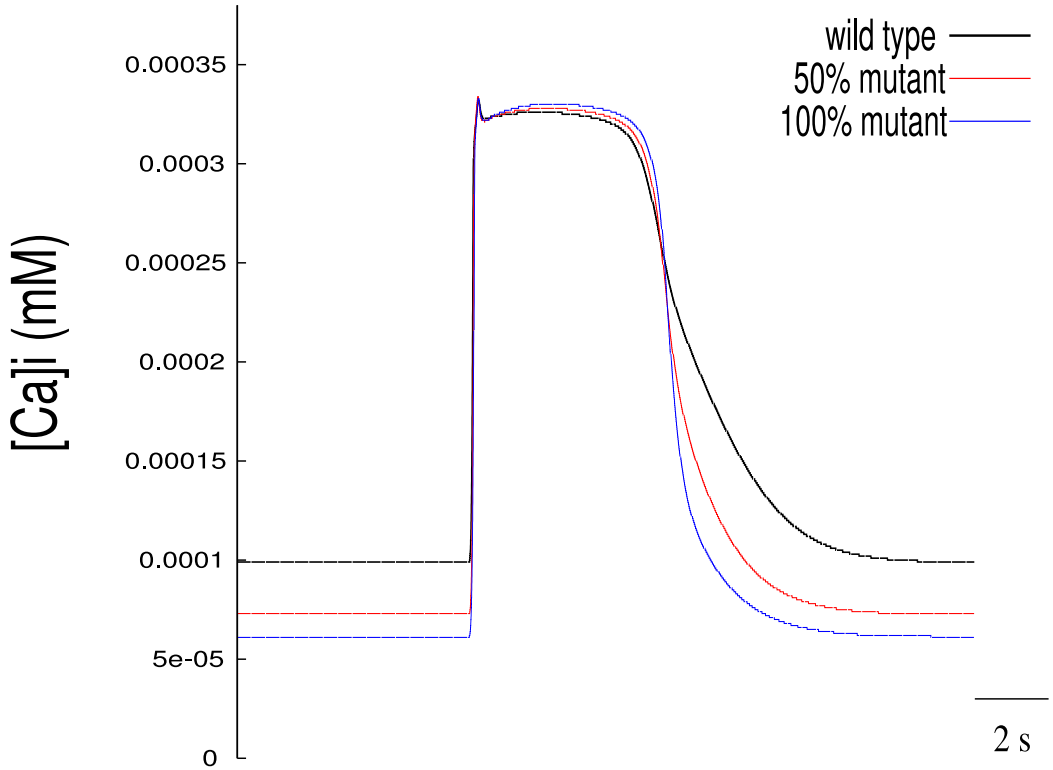

	AUC (μM*s)	variation (%)
Wild type	3.4	-
50% mutant	2.93	-15%
100% mutant	2.7	-20%

Figure 8.5: Upper Panel: Intracellular Ca^{2+} concentration in SM cells as a function of time in wild type conditions (black line) and with a simulated SCN5A mutation affecting 50% (red line) and 100% (blue line) of the Na^{+} channels. The Ca^{2+} concentration during the resting phase of the slow wave was shifted from 99 nM in wild type condition to 73 and 61 nM in the genetically modified situation (50% and 100% respectively). Lower panel: Area under the curve (AUC) of the intracellular Ca^{2+} concentration in SM cells during a single slow wave in different conditions. The AUC was calculated using the trapezoidal rule with time steps of 0.1 ms.

simulations conducted in wild type and mutated cells was examined. Figure 8.5 (upper panel) shows the intracellular Ca^{2+} concentration from a SM cell during a single simulated slow wave with wild type (black line) and mutated channels (red line with 50% mutant channels and blue line with 100% mutant channels). The lower panel of Figure 8.5 shows estimates of the area under the curve (AUC) of the intracellular Ca^{2+} concentration during a single slow wave. The AUC is often used in toxicology studies to measure cellular exposure to a given drug. Here, it is used to quantify the variation in the availability of Ca^{2+} ions duirng a single slow wave. The Na^{+} channel mutation appears to indirectly cause a 20% decrease in Ca^{2+} exposure in these simulations. This is due to the altered membrane potential during the resting phase of the slow wave which, in turn, decreases the open probability of the voltage-gated Ca^{2+} channels (I_{CaL} and I_{LVA}) thereby decreasing Ca^{2+} influx.

8.4 1-D cable simulations

In order to investigate the effects of the SCN5A genetic mutation on the chronotropicity of the slow waves, we conducted simulations in a one dimensional cable model. All of the simulation parameters used to characterise the cable are the same as those presented in Chapter 5. Briefly, we simulated a 337 mm-long cable running from the top of the fundus to the pylorus along the greater curvature of the stomach. Since all regions of the stomach have been reported to harbour ICC (Stratton *et al.*, 2007), we included ICC along the entire length of the fibre. The propagation of electrical activity between ICC was modelled following a continuum modelling approach as described by

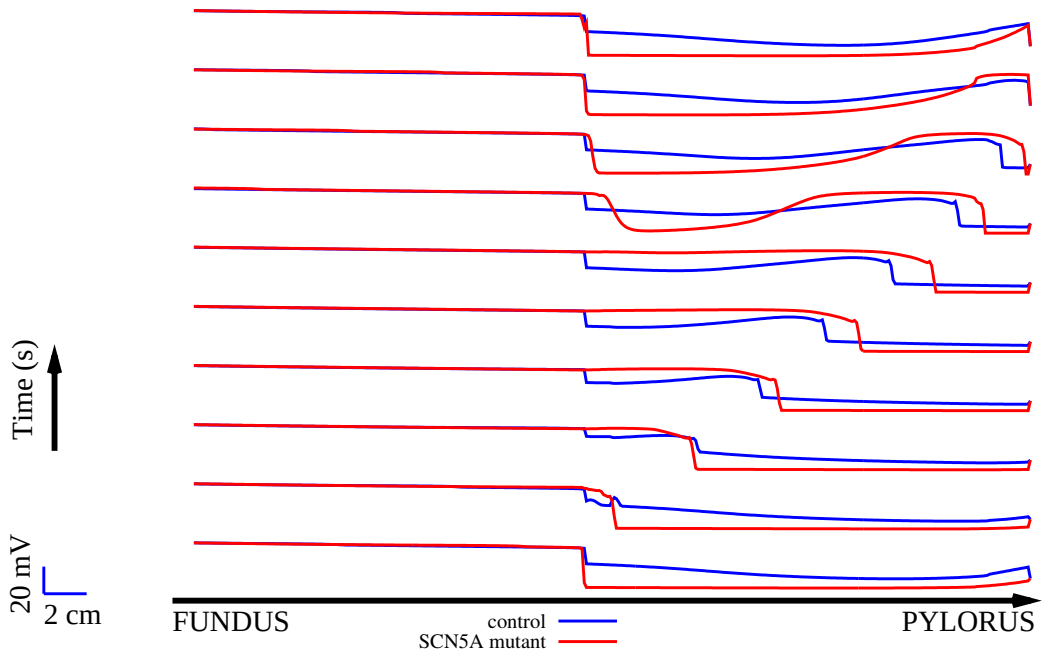

Figure 8.6: Propagation of slow waves along the fibre: SM cell transmembrane potential along the fibre at ten different time instants (one every 2 seconds) in control conditions (blue lines) and in the case where Na^+ currents are affected by a genetic mutation of the SCN5A gene (red lines). Different initial time instants between wild type (t=48.5 s) and genetically mutant case (t=51.8 s) were chosen in order to obtain two waves that started at the same time allowing a comparison of the propagation velocity. Scale bars apply to all traces.

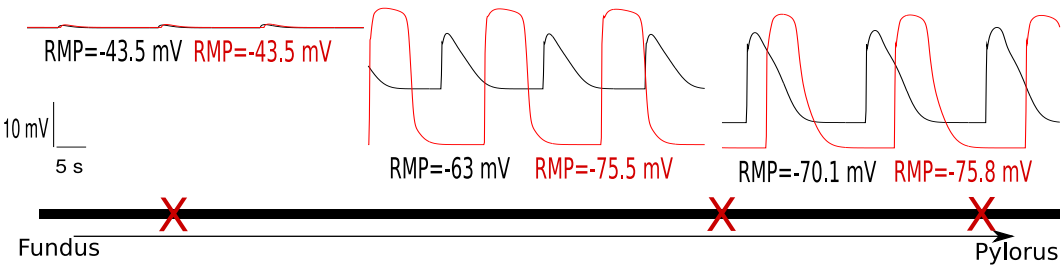

Figure 8.7: Simulated slow waves in different parts of the fibre in control conditions (black lines) and with the SCN5A-encoded Na^+ mutation (red lines and text). The traces show a period of simulated time between 75 and 130 seconds. Scale bars apply to all traces. The red crosses along the black fibre represent the three locations where the simulated traces are taken from. The distances from the top of the fundus are 42.5 mm, 210.6 mm and 294.9 mm respectively.

Equation 5.1. The cable was divided in a computational mesh of 400 elements and the finite element method was used to integrate Equation 5.1 with a time step of 0.1 ms. At each point, the transmembrane potential of the SM cell was calculated by Equation 5.3. The genetic mutation affecting the SCN5A-encoded Na^+ channel was taken into account by including different I_{ion} terms, as per Equations 8.13 and 8.14 in Equation 5.1. Figure 8.6 shows the simulated propagation of slow waves along the cable in control conditions (blue lines) and with the mutant channels (red lines). The genetic mutation affecting Na^+ currents does not have any effect on the membrane potential in the fundus. The location of the origin slow waves was also not affected by the genetic mutation. Consistent with single cell simulations, the RMP in the antrum was shifted in the hyperpolarised direction by 5 mV. The propagation velocity increased slightly in the mutant case compared to the wild type simulation. Figure 8.7 gives further insights into the slow waves in different

regions of the cable in control (black lines) and mutant (red lines) conditions. Slow waves were of longer duration when the Na^+ channels contained the genetic mutation (8.7s in control conditions and 9.2 s in the mutant case). The simulations saw a decrease in the slow wave frequency from 3 cpm in control conditions to 2.7 cpm in the mutant case. These results are consistent with both the hyperpolarised RMP predicted by single cell simulations and the decrease in slow wave frequency that have been found experimentally by blocking Na^+ currents in human intestinal ICC (Strege *et al.*, 2003). In addition, our simulations showed a significant loss of RMP gradient (Figure 8.7) that caused a loss of slow wave heterogeneity along the stomach distal to the initiation site. The difference in shape between the corporal and antral slow waves was not observed when mutation to the SCN5A gene was included.

8.5 Whole Stomach and Torso Simulations

Whole organ simulations were conducted using the stomach geometry presented in Section 6.2. The cellular components (ICC and SM cells) that characterise the tissue contained the mutant version of the Na^+ channel (Equation 8.9) or the wild type version (Equation 8.1). All other parameters were left unaltered (see Chapter 6 for a detailed description of the three dimensional stomach model). Figure 8.8 shows a comparison of the membrane potential from the SM cells on the surface of the stomach in the wild type and mutant cases. The major difference is the more hyperpolarised state of the gastric antrum when the mutation affects the kinetics of the Na^+ channels. This is consistent with experimental evidence obtained in the presence of Na^+ chan-

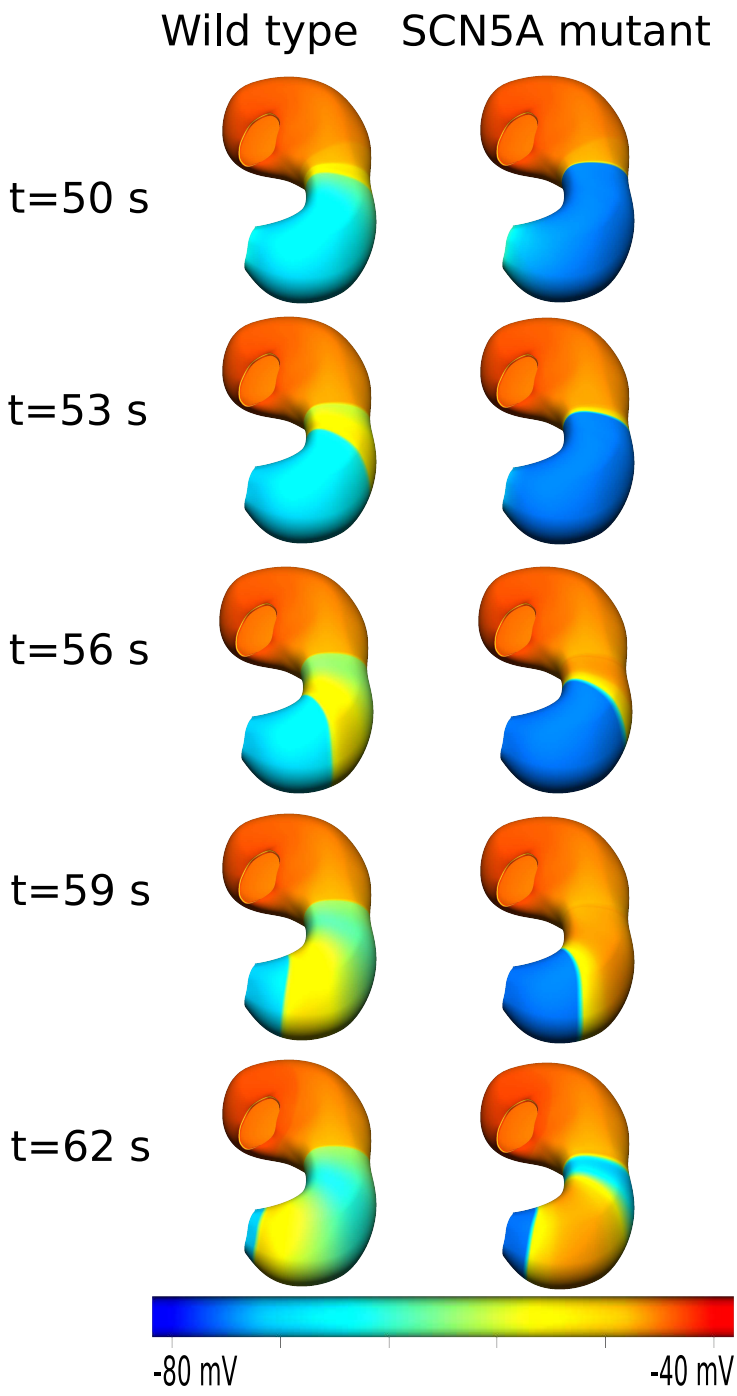

Figure 8.8: SM membrane potential on the surface of the stomach at five different time instants. Results in control conditions are shown on the left while the genetically modified (100 %) situation is shown on the right.

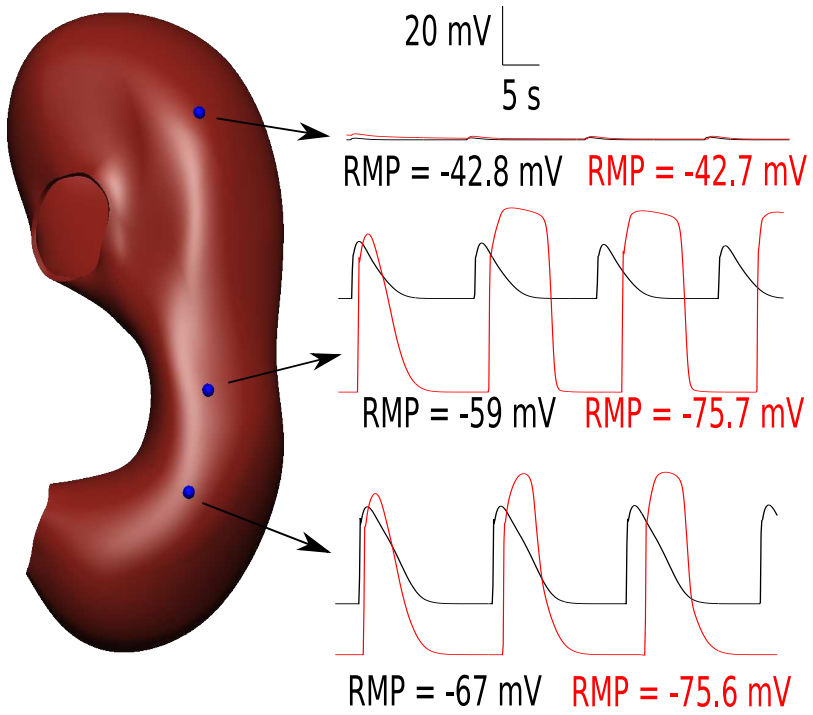

Figure 8.9: Slow waves at three different points in the stomach, one in the fundus, one in the corpus and one in the antrum. Black lines correspond to the wild type case, red lines show the slow waves in the presence of the SCN5A mutation. Scale bars apply to all traces.

nel blockers in human intestinal ICC (Strege *et al.*, 2003). The implications of this for the intracellular Ca^{2+} dynamics of the SM cells have already been discussed in Section 8.3. Another notable effect of the mutation was the increased amplitude of the wave front. This is even more apparent in Figure 8.9 where slow waves at different locations in the stomach are displayed in both wild type and mutant conditions. The effects of the genetic mutation become apparent in the corpus and antrum where the RMP is more hyperpolarised. The gradient in RMP and the slow wave heterogeneity are lost. Figure 8.9 also shows the slight decrease in frequency that the increased slow wave dura-

tion causes. Again, this is in agreement with experimental data from human intestinal ICC in presence of Na^+ channel blockers in (Strege *et al.*, 2003). It is also consistent with our 1D simulations from Section 8.4. To further investigate the effects of the SCN5A mutation, we simulated the potential on the human torso and calculated the EGG resulting from the activity of cells affected by the mutation of the SCN5A gene. Results of such simulations are shown in Figure 8.10, where the EGG in the wild type situation (black line) is compared with the mutant case (red line). The EGG trace shows a difference in amplitude, due to the larger amplitude of the mutant slow waves. The frequency is also slightly decreased as noted in the membrane traces.

8.6 Summary of Modelling the SCN5A Mutation

In this chapter an application of the multiscale modelling framework developed in this thesis was presented. The motivation was a recent epidemiological study showing that 65% of patients affected by a cardiac genetic abnormality of the SCN5A gene also presented GI symptoms (Locke *et al.*, 2006). Due to the lack of understanding of the pathophysiological mechanisms that underlie the onset of the GI clinical symptoms, no specific effective therapy is available for these patients. The cellular models of ICC and SM cell developed within this thesis (see Chapters 3 and 4) contain a detailed description of the SCN5A-encoded GI Na^+ channel and therefore appeared suitable for investigating the effects of a genetic abnormality affecting Na^+ channels.

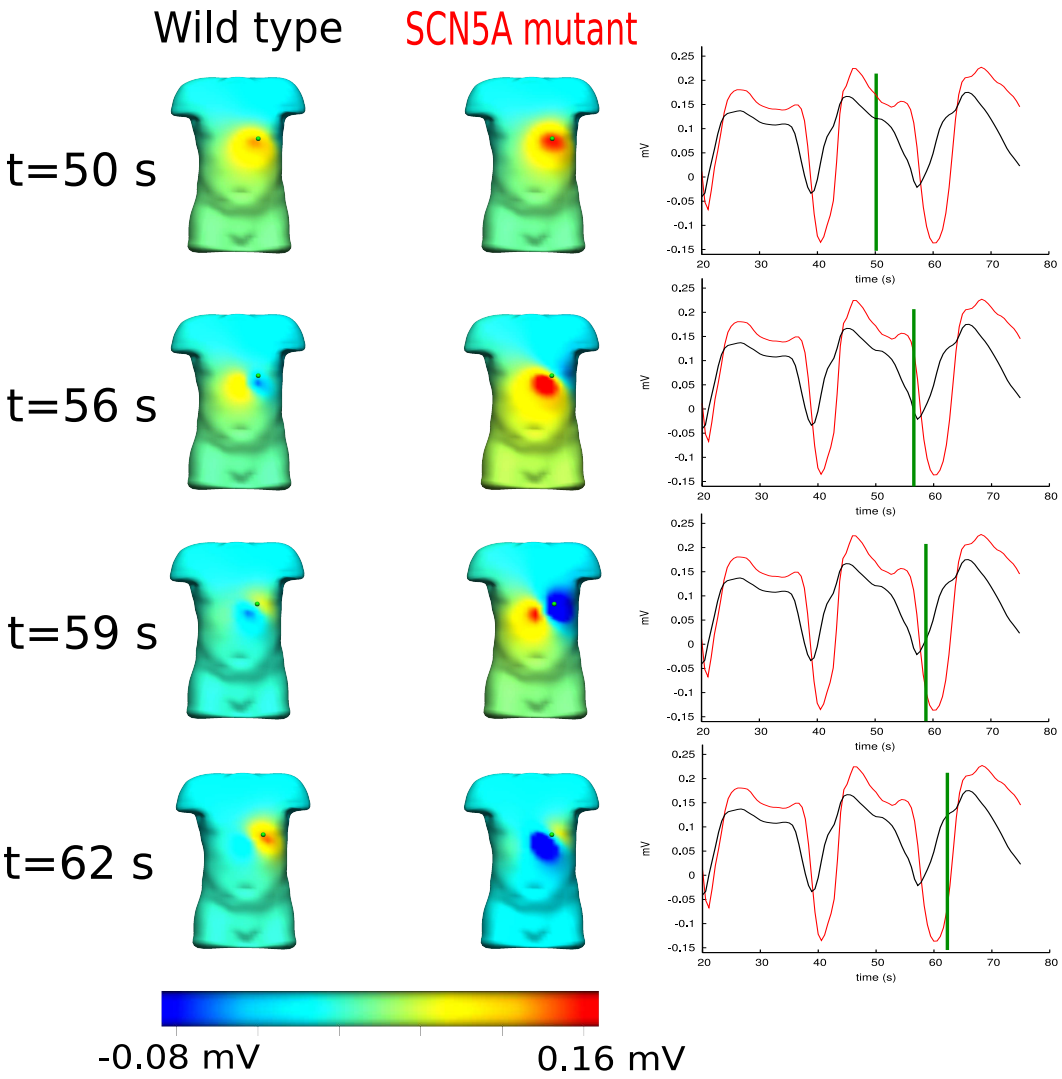

Figure 8.10: Electrical potentials across the human torso at four different time instants in the wild type case (left panel) and the mutant case (middle panel). The right panel shows the simulated EGG obtained at the location of the green dot. Black lines refer to wild type, red lines refer to the case where the cellular Na^+ currents are affected by the SCN5A mutation. The vertical green bar marks the time on the plot corresponding to the images on the left.

To compare a physiological (wild type) state with a genetically compromised one (mutant), a computational description of the activity of the Na^+ channels in both conditions was needed. For the wild type channel, experimental data from human intestinal ICC and SM cells were used to construct a suitable HH-type equation that reproduced the experimentally recorded currents under voltage clamp conditions. Modelling the mutant situation presented a variety of challenges. Firstly, the epidemiological study of Locke *et al.* (2006) did not provide the genotype of the cohort of patients who were included in the study, making it impossible to identify whether one particular mutation of the SCN5A gene, out of the multitude that have been reported, was responsible for the onset of GI symptoms. Furthermore, none of the SCN5A mutations in the GI tract has been functionally characterised. This is probably due to the relatively recent molecular identification of Na^+ channels in the GI tract (Holm *et al.*, 2002). When compared to its cardiac counterpart, the GI Na^+ channel presented a 99% homology, with only one single amino acid difference, thus making the cardiac Na^+ channel structurally similar to its GI correspondent. Because of the lack of a specific characterisation of any GI SCN5A mutation, a model of one particular cardiac SCN5A mutation, the 1795insD mutation, was chosen as a model for its GI counterpart. The reasons behind the choice of focusing on this mutation were twofold. First, as both patients affected by long QT syndrome and Brugada syndrome were included in the epidemiological survey of GI symptoms (Locke *et al.*, 2006), a mutation that has been associated with both conditions, like the 1795insD, was deemed appropriate. Second, a validated computational description of this cardiac mutation was

readily available (Clancy & Rudy, 2002)). The computational description was based on Markovian models of the biophysics of the ion channel. In particular, Clancy & Rudy (2002) developed two Markovian models, one for the wild type channel and one for the 1795insD mutant channel. When inserted into computational models of gastric ICC and SM cells, the two Markovian models generated different Na^+ current profiles. Nevertheless, these differences were found to have minimal impact on the slow wave profile. Moreover, the difference between the HH formulation and the two Markovian formulations was significant. It was noticed that the effects of including the Markovian model of the Na^+ channel into the models of the gastric ICC and SM cells were very similar to the case where Na^+ currents were blocked (Figure 8.4). The Markovian description of the cardiac SCN5A mutation was therefore adopted to simulate a loss-of-function mutation in the GI tract. Interestingly, the electrophysiological characteristics of the cardiac 1795insD mutation (slower peak amplitude and slower recovery from inactivation) were reported to act as both gain-of-function and loss-of-function mutations in the heart depending on which cellular type (endocardial, epicardial or M-cells) was examined.

The effects of the mutant channels were examined by comparison with the wild type situation at the single cell level (Section 8.3), in a one dimensional cable model (Section 8.4) and on a three dimensional stomach geometry (Section 8.5). Our simulations predicted the potentially significant effects of a SCN5A mutation on gastric slow waves which include (i) membrane hyperpolarisation during the RMP phase of the slow wave (Figure 8.4), (ii) a slight decrease in frequency due to the bigger slow wave amplitude and (iii) a loss

of slow wave heterogeneity between the corpus and the antrum (Figures 8.7 and 8.9). These effects were reflected at organ level and through alterations in the EGG traces (Section 8.5). While it is not currently possible to directly validate these predictions because of the absence of experimental recordings from tissue affected by this specific SCN5A genetic mutation, it is interesting to note that these observations are consistent with experimental findings obtained in presence of Na^+ channel blockers in human small intestine (Strege *et al.*, 2003).

As the RMP changed as a consequence of the abnormal Na^+ channel kinetics, the intracellular Ca^{2+} concentration was also affected (Figure 8.5). This was primarily due to the response of the voltage dependent gates in the Ca^{2+} channels to the new membrane potential. In SM cells, intracellular Ca^{2+} concentration is one of the primary regulators of contractile responses, and a reduced accumulation of Ca^{2+} ions may cause a decreased contractile response. However, the peak Ca^{2+} concentration observed during the slow wave was not significantly altered. Interestingly, quantitative experimental measurement of the intracellular Ca^{2+} concentration presents a variety of technical difficulties, especially if one wants to compare a normal tissue with an abnormal one. The modelling approach presented in this chapter allows a quantitative prediction of such parameters as a result of the combined activity of all the relevant cellular components.

In conclusion, in this chapter we have presented a preliminary exploration of the capabilities of the integrated multiscale modelling approach developed in this thesis. By implementing simulations at cellular and tissue levels, we

were able to predict morphological and chronotropic changes in the slow wave activity that were caused by a genetic mutation. This will potentially allow us to make predictions on possible mechanisms that lead from the genotype of a mutation to its clinical phenotype.

Chapter 9

Conclusions

The aim of this thesis was to develop a multiscale modelling framework for the study of gastric electrophysiology in health and disease. Simulations were conducted to capture fine details of ion channel physiology at the tissue and organ level in the GI tract.

First, we developed models of the two cell types responsible for gastric eletrical activity (ICC and SM cell). The first two biophysically based descriptions of such cells, these models are able to succinctly capture a large amount of experimental data obtained by many investigators with patch clamp experiments on isolated cells and tissues from the GI tract. Particular attention has been devoted to rigorously validating the cellular models. In each case, the predicted profile of the transmembrane potential has been compared with available experimental recordings and good correspondence has been found in physiological and pharmacologically altered conditions.

Second, we integrated the two single cell models into multidimensional tissue and organ simulations. This allowed us to investigate the effects of spatially

varying properties of the gastric musculature. In the presented example, the effects of different CO concentrations on the physiology of the slow waves were investigated and a novel mechanism for the regulation of the site of initiation for slow waves in the stomach was proposed.

Third, we simulated the EGG signals that can be recorded on the skin surface. We were able to simulate the EGG starting from detailed, biophysically based cellular models. Finally, we explored one potential use of this multiscale modelling framework by investigating the effects of a genetic mutation affecting the SCN5A-encoded GI Na^+ channel on the electrophysiology of the stomach.

9.1 Limitations and Future Work

During the process of developing the modelling framework presented in this thesis, a variety of desirable features were noted that could not be included or implemented due to time and/or data costraints. While some of these features have already been discussed in the relevant chapters, here we provide an overview of the limitations that we have encountered and suggest possible ways to overcome them.

All the models that were discussed in this thesis were built and validated whenever possible againts published experimental data, most of which was obtained from cells isolated from the GI tract of different mammals. It would be desirable to have a model built entirely from data from the cells of one specific animal and, ideally, that specific animal would be the human. Unfortunately, electrophysiological data from human cells in the GI tract are still very rare.

We collated data mostly of murine, guinea-pig and canine origin. Nevertheless, it was also not possible to build a model based entirely on any specific species. Thus, we had to combine data from different animal sources in order to develop comprehensive models. While in the field of cardiac electrophysiology cellular models that are entirely based on human data have already appeared in literature (ten Tusscher *et al.*, 2004), enough experimental data from the human GI tract will hopefully be available in the near future and will allow the development of models of human GI electrophysiology.

Many aspects of GI physiology are currently object of controversy as different experimental observations seem to point to different conclusions. During the development of the cell models, we often had to make specific choices in favour of one theory over another. The choice of which K^+ conductances should be included in the SM cell model and the modelling of the mechanisms of slow wave entrainment in ICC are just two examples of such aspects. The models developed in this thesis are modular in nature, i.e., each component has been validated individually before being included in the whole cell model. As a consequence, if any of the controversial aspects are eventually be resolved against the theory that was adopted here, the models will need to be adjusted only for the part regarding the theory or mechanism in question.

Chapter 8 presented a preliminary exploration of the capabilities of a multiscale modelling approach, where biophysically based cell models are integrated into large scale simulations. There exist many areas of clinical interest where the same type of investigation can be performed. Gastric electrical stimulation (GES), for example, is a relatively new therapeutic approach to

idiopathic intractable gastroparesis where an electrical stimulator is implanted on the serosa to deliver electrical stimuli with the aim of eliciting a contractile response (Csepel *et al.*, 2006; Lin *et al.*, 2003). Despite some degree of clinical success, GES still faces many challenges, primarily due to the lack of understanding of the mechanisms that lead, in certain cases, to a restoration of gastric motility. The modelling framework presented in this thesis would allow the simulation of external stimuli and an investigation of the effects of the external stimuli across multiple spatial scales. This could also lead to an optimisation of the stimulus parameters, currently an object of controversy amongst clinicians (Lin *et al.*, 2006c; Liu *et al.*, 2006). Similarly, diabetic gastroparesis, a common complication affecting up to 50% of diabetic patients, has been associated with abnormal ICC behaviour and maintainance (Vittal *et al.*, 2007). No effective pharmacological therapeutic approach exists today for these patients. As the model of a gastric ICC from Chapter 4 contains a basic description of glucose activity and its influence on the slow wave, the modelling framework developed in this thesis might be employed to elucidate the mechanisms that lead from impaired glucose handling to the onset of gastroparesis.

Gastric slow waves provide a significant part of the electrical activity required for contractile responses to occur. One of the most natural future developments would be the development of a coupled electro-mechanical modelling framework, where the electrical descriptions presented here would be coupled with contractile models of a SM cell. A similar approach has already been pursued for modelling cardiac activity (Nickerson *et al.*, 2005). In view

of this, particular attention should be placed on the dynamics of intracellular Ca^{2+}, which will constitute the interface with any biophysically based model of contraction.

In conclusion, we have integrated models from ion channels to cells to tissues, organs and through to the whole torso, bringing together a vast quantity of experimental data and packaging it succinctly. We have performed a preliminary exploration of the capabilities of the modelling framework that was developed for a known channelopathy. This thesis is intended to pave the way for the establishment of computational electrophysiology as a useful tool for investigating gastric physiology in health and disease.

9.2 Note on Computational Methods

During the development of the computational framework presented in this thesis a variety of software and methods have been used. A Linux operating system (Fedora Core 6) was used for most of the work included in this thesis. The codes for the single cell models of Chapters 3 and 4 were written in C and GCC 4.1.1 (©2006, Free Software Foundation) was used to compile them. Most of the plots were drawn using the freely available GNUPlot 4.0 software (©1986 - 1993, 1998, 2004 Thomas Williams, Colin Kelley). The integration of partial differential equations involved in the tissue simulations (Chapters 5, 6 and 7) was performed using CMISS (©Auckland UniServices Ltd) which is freely available for academic use. Visualisation of results (e.g. Figure 6.2) was obtained by using the graphical interface of CMISS, named CMGUI (©Auckland UniServices Ltd) which is available for free download

from `http://www.cmiss.org/`. Temporal plots at particular locations in the tissue (e.g. Figure 6.3) were obtained by using the freely available Unemap software (©Auckland UniServices Ltd) in combination with GNUPlot. In order to input the cell models into the CMISS software, a translation from the original C code to the CellML language (http://www.cellml.org/) was performed. These implementations are now freely available for download from `http://www.bioeng.nus.edu.sg/compbiolab/`.

9.3 Publications

The work contained in this thesis has been presented in the following journal articles and conference publications:

International peer-reviewed journals

- **Corrias A**, Nickerson DP, Buist ML "Carbon monoxide and origin of the gastric slow wave: a simulation study" *Under review, 2008.*
- **Corrias A**, Buist ML "A quantitative cellular description of gastric slow wave activity" *American Journal of Physiology, 2008.* Apr;294(4):G989-95.
- Nickerson DP, **Corrias A**, Buist ML "Reference descriptions of cellular electrophysiology models" *Bioinformatics, 2008* 24(8):112-114.
- **Corrias A**, Buist ML "A quantitative model of gastric smooth muscle cellular activation" *Annals of Biomedical Engineering, 2007* Sep;35(9): 1595-607.

International Conferences (presenter listed first)

- Buist ML, **Corrias A**. "Initiation of the gastric slow wave" Accepted at the Neurogasotroenterology & Motility Joint International Meeting. Lucerne (Switzerland), 6 Nov - 9 Nov 2008.

- Buist ML, **Corrias A**. "The origins of the gastric pacemaker" Oral Presentation at the Biomedical Engineering Society Annual Meeting. St. Louis (USA), 2 Oct - 4 Oct 2008.

- **Corrias A**, Buist ML. "Gastric slow wave heterogeneity: a model study of possible causes" Oral presentation at the 3rd Tohoku-NUS Joint Symposium. Singapore, 10 Dec - 13 Dec 2007.

- **Corrias A**, Buist, ML. "A quantitative cellular description of gastric pacemaker activity" Oral presentation at The 21st International Symposium on Neurogastroenterology and Motility, Jeju Island (South Korea) 2 Sep - 5 Sep 2007.

- Buist ML, **Corrias A**. "A model of gastric smooth muscle cellular activation" Oral Presentation at The 3rd WACBE World Congress on Bioengineering 2007, Bangkok (Thailand) 11 Jul - 13 Jul 2007.

- **Corrias A**, Buist ML. "A model of gastric smooth muscle cellular activation" Poster presentation at the Joint International Neurogastroenterology and Motility Meeting, Boston (USA), 14 Sept - 17 Sept 2006.

Local Conferences and Seminars

- **Corrias A**, Buist ML. "A quantitative cellular description of gastric pacemaker activity". Oral Presentation at the 9th GPBE Conference, Singapore. Sep, 14th, 2007. **Third prize winner for best presentation.**

- **Corrias A**, Buist ML. "A quantitative cellular description of gastric pacemaker activity". Oral Presentation at the 4th Scientific Meeting of the Biomedical Engineering Society, Singapore. May, 19th, 2007

- **Corrias A**, Buist ML. "Computational modelling of gastric electrophysiology"Invited Oral Presentation at the Graduate Students' seminars, Division of Bioengineering, NUS, Singapore. February, 14th, 2007

- **Corrias A**, Buist ML. "A model of gastric smooth muscle cellular activation"Poster Presentation at the First GPBE-NGS Bioengineering Conference, Singapore. August, 24th, 2006

- **Corrias A**, Lu S and Soong TW. "Effects of two Sodium channel point mutation found in two different species of pufferfish on the electrophysiological response to Tetrodotoxin (TTX)"Oral Presentation at the 6th GPBE Students Conference, Biopolis, Singapore. August, 4th, 2005

- **Corrias A**. "Electrophysiological models and their applications". Invited Oral Presentation at the Graduate Students' seminars, Division of Bioengineering, NUS, Singapore. April, 07th, 2005.

- **Corrias A**, Buist ML. "Looking up cardiac activation". Oral Presentation at the 5th GPBE Students' Conference, Singapore. January, 7th, 2005.

Bibliography

Abid S & Lindberg G (2007). Electrogastrography: poor correlation with antro-duodenal manometry and doubtful clinical usefulness in adults. *World J Gastroenterol* **13**(38), 5101–7.

Ackerman M. J, Splawski I, Makielski J. C, Tester D. J, Will M. L, Timothy K. W, Keating M. T, Jones G, Chadha M, Burrow C. R, Stephens J. C, Xu C, Judson R & Curran M. E (2004). Spectrum and prevalence of cardiac sodium channel variants among black, white, Asian, and Hispanic individuals: implications for arrhythmogenic susceptibility and Brugada/long QT syndrome genetic testing. *Heart Rhythm* **1**(5), 600–7.

Akbarali H. I & Giles W. R (1993). Ca2+ and Ca2+ -activated Cl- currents in rabbit oesophageal smooth muscle. *J Physiol* **460**, 117–33.

Aliev R. R, Richards W & Wikswo J. P (2000). A simple nonlinear model of electrical activity in the intestine. *J Theor Biol* **204**(1), 21–8.

Amberg G. C, Baker S. A, Koh S. D, Hatton W. J, Murray K. J, Horowitz B & Sanders K. M (2002). Characterization of the A-type potassium current in murine gastric antrum. *J Physiol* **544**(2), 417–28.

Antzelevitch C & Yan G. X (2000). Cellular and ionic mechanisms responsible for the Brugada syndrome. *J Electrocardiol* **33**(Suppl), 33–9.

Barajas-Lopez C, Berezin I, Daniel E. E & Huizinga J. D (1989). Pacemaker activity recorded in interstitial cells of Cajal of the gastrointestinal tract. *Am J Physiol* **257**(4 Pt 1), C830–5.

Barrett J. N, Magleby K. L & Pallotta B. S (1982). Properties of single calcium-activated potassium channels in cultured rat muscle. *J Physiol* **331**, 211–30.

Bayguinov O, Ward S. M, Kenyon J. L & Sanders K. M (2007). Voltage-gated Ca2+ currents are necessary for slow-wave propagation in the canine gastric antrum. *Am J Physiol Cell Physiol* **293**(5), C1645–59.

Beckett E. A, Bayguinov Y. R, Sanders K. M, Ward S. M & Hirst G. D (2004). Properties of unitary potentials generated by intramuscular interstitial cells of Cajal in the murine and guinea-pig gastric fundus. *J Physiol* **559**(1), 259–69.

Bedard C & Destexhe A (2008). A modified cable formalism for modeling neuronal membranes at high frequencies. *Biophys J* **94**(4), 1133–43.

Birchfield R. I, Menefee E. E & Bryant G. D (1957). Disease of the sinoatrial node associated with bradycardia, asystole, syncope, and paroxysmal atrial fibrillation. *Circulation* **16**(1), 20–6.

Boev K, Bonev A & Papasova M (1985). 4-aminopyridine-induced changes in the electrical and contractile activities of the gastric smooth muscle. *Gen Physiol Biophys* **4**(6), 589–95.

Bondarenko V. E & Rasmusson R. L (2007). Simulations of propagated mouse ventricular action potentials: effects of molecular heterogeneity. *Am J Physiol Heart Circ Physiol* **293**(3), H1816–32.

Bootman M. D, Collins T. J, Mackenzie L, Roderick H. L, Berridge M. J & Peppiatt C. M (2002). 2-aminoethoxydiphenyl borate (2-APB) is a reliable blocker of store-operated Ca2+ entry but an inconsistent inhibitor of InsP3-induced Ca2+ release. *FASEB J* **16**(10), 1145–50.

Bradley C. P, Pullan A. J & Hunter P. J (1997). Geometric modeling of the human torso using cubic hermite elements. *Ann Biomed Eng* **25**(1), 96–111.

Bradley C. P, Harris G. M & Pullan A. J (2001). The computational performance of a high-order coupled FEM/BEM procedure in electropotential problems. *IEEE Trans Biomed Eng* **48**(11), 1238–50.

Bradley K. N, Flynn E. R, Muir T. C & McCarron J. G (2002). Ca2+ regulation in guinea-pig colonic smooth muscle: the role of the Na+-Ca2+ exchanger and the sarcoplasmic reticulum. *J Physiol* **538**(2), 465–82.

Buist M, Sands G, Hunter P & Pullan A (2003). A deformable finite element derived finite difference method for cardiac activation problems. *Ann Biomed Eng* **31**(5), 577–88.

Buist M. L, Cheng L. K, Yassi R, Bradshaw L. A, Richards W. O & Pullan A. J (2004). An anatomical model of the gastric system for producing bioelectric and biomagnetic fields. *Physiol Meas* **25**(4), 849–61.

Cajal S (1893). Sur les ganglions et plexus nerveux de l'in-testin. *C.R. Soc Biol (Paris)* **45**, 217–223.

Carl A, Frey B. W, Ward S. M, Sanders K. M & Kenyon J. L (1993). Inhibition of slow-wave repolarization and Ca2+-activated K+ channels by quaternary ammonium ions. *Am J Physiol* **264**(3 Pt 1), C625–31.

Carl A, Lee H. K & Sanders K. M (1996). Regulation of ion channels in smooth muscles by calcium. *Am J Physiol* **271**(1 Pt 1), C9–34.

Casteels R (1981). Membrane potential in smooth muscle. In *Smooth muscle, an assessment of current knowledge*, pp. 105–126. Edward Arnold, London.

CellML repository. URL. http://www.cellml.org/models/ (2008).

Chang F. Y (2005). Electrogastrography: basic knowledge, recording, processing and its clinical applications. *J Gastroenterol Hepatol* **20**(4), 502–16.

Chen C. L, Hu C. T, Lin H. H & Yi C. H (2006). Clinical utility of electrogastrography and the water load test in patients with upper gastrointestinal symptoms. *J Smooth Muscle Res* **42**(5), 149–57.

Cheng L. K, Buist M. L & Pullan A. J (2006). Anatomically realistic torso model for studying the relative decay of gastric electrical and magnetic fields. *Conf Proc IEEE Eng Med Biol Soc* **1**, 3158–61.

Cho W. J & Daniel E. E (2005). Proteins of interstitial cells of Cajal and intestinal smooth muscle, colocalized with caveolin-1. *Am J Physiol Gastrointest Liver Physiol* **288**(3), G571–85.

Clancy C. E & Rudy Y (2002). Na+ channel mutation that causes both Brugada and long-QT syndrome phenotypes: a simulation study of mechanism. *Circulation* **105**(10), 1208–13.

Clancy C. E & Rudy Y (1999). Linking a genetic defect to its cellular phenotype in a cardiac arrhythmia. *Nature* **400**(6744), 566–9.

Corrias A & Buist M. L (2007). A quantitative model of gastric smooth muscle cellular activation. *Ann Biomed Eng* **35**(9), 1595–1607.

Corrias A & Buist M. L (2008). Quantitative cellular description of gastric slow wave activity. *Am J Physiol Gastrointest Liver Physiol* **294**(4), G989–95.

Cousins H. M, Edwards F. R, Hickey H, Hill C. E & Hirst G. D (2003). Electrical coupling between the myenteric interstitial cells of Cajal and adjacent muscle layers in the guinea-pig gastric antrum. *J Physiol* **550**(3), 829–44.

Daniel E. E (2004). Communication between interstitial cells of Cajal and gastrointestinal muscle. *Neurogastroenterol Motil* **16**(Suppl 1), 118–22.

Csepel J, Goldfarb B, Shapsis A, Goff S, Gabriel N & Eng H. M (2006). Electrical stimulation for gastroparesis. Gastric motility restored. *Surg Endosc* **20**(2), 302–6.

Sobral Cintra R. J, Tchervensky I. V, Dimitrov V. S & Mintchev M. P (2004). Optimal wavelets for electrogastrography. *Conf Proc IEEE Eng Med Biol Soc* **1**, 329–32.

Dickens E. J, Hirst G. D & Tomita T (1999). Identification of rhythmically active cells in guinea-pig stomach. *J Physiol* **514**(2), 515–31.

Dobrydneva Y & Blackmore P (2001). 2-Aminoethoxydiphenyl borate directly inhibits store-operated calcium entry channels in human platelets. *Mol Pharmacol* **60**(3), 541–52.

Dumaine R, Wang Q, Keating M. T, Hartmann H. A, Schwartz P. J, Brown A. M & Kirsch G. E (1996). Multiple mechanisms of Na+ channel–linked long-QT syndrome. *Circ Res* **78**(5), 916–24.

Dumaine R, Towbin J. A, Brugada P, Vatta M, Nesterenko D. V, Nesterenko V. V, Brugada J, Brugada R & Antzelevitch C (1999). Ionic mechanisms responsible for the electrocardiographic phenotype of the Brugada syndrome are temperature dependent. *Circ Res* **85**(9), 803–9.

Durante W, Johnson F. K & Johnson R. A (2006). Role of carbon monoxide in cardiovascular function. *J Cell Mol Med* **10**(3), 672–86.

Edwards F. R & Hirst G. D (2003). Mathematical description of regenerative potentials recorded from circular smooth muscle of guinea pig antrum. *Am J Physiol Gastrointest Liver Physiol* **285**(4), G661–70.

Edwards F. R & Hirst G. D (2005). An electrical description of the generation of slow waves in the antrum of the guinea-pig. *J Physiol* **564**(1), 213–32.

Encyclopedia Britannica. URL. http://www.britannica.com/ebc/art-68634/ (2003).

Faber G. M & Rudy Y (2000). Action potential and contractility changes in [Na+](i) overloaded cardiac myocytes: a simulation study. *Biophys J* **78** (5), 2392–404.

Fall C. P & Keizer J. E (2001). Mitochondrial modulation of intracellular Ca2+ signaling. *J Theor Biol* **210**(2), 151–65.

Farrugia G (1999). Ionic conductances in gastrointestinal smooth muscles and interstitial cells of Cajal. *Annu Rev Physiol* **61**, 45–84.

Farrugia G, Irons W. A, Rae J. L, Sarr M. G & Szurszewski J. H (1993). Activation of whole cell currents in isolated human jejunal circular smooth muscle cells by carbon monoxide. *Am J Physiol* **264**(6 Pt 1), G1184–9.

Farrugia G, Rich A, Rae J. L, Sarr M. G & Szurszewski J. H (1995). Calcium currents in human and canine jejunal circular smooth muscle cells. *Gastroenterology* **109**(3), 707–17.

Farrugia G, Miller S. M, Rich A, Liu X, Maines M. D, Rae J. L & Szurszewski J. H (1998). Distribution of heme oxygenase and effects of exogenous carbon monoxide in canine jejunum. *Am J Physiol* **274**(2 Pt 1), G350–8.

Farrugia G, Lei S, Lin X, Miller S. M, Nath K. A, Ferris C. D, Levitt M & Szurszewski J. H (2003). A major role for carbon monoxide as an endogenous hyperpolarizing factor in the gastrointestinal tract. *Proc Natl Acad Sci U S A* **100**(14), 8567–70.

Fischer G, Tilg B, Modre R, Huiskamp G. J, Fetzer J, Rucker W & Wach P (2000). A bidomain model based BEM-FEM coupling formulation for anisotropic cardiac tissue. *Ann Biomed Eng* **28**(10), 1229–43.

Fitzhugh R (1962). Computation of impulse initiation and saltatory conduction in a myelinated nerve fiber. *Biophys J* **2**, 11–21.

Forrest A. S, Ordog T & Sanders K. M (2006). Neural regulation of slow-wave frequency in the murine gastric antrum. *Am J Physiol Gastrointest Liver Physiol* **290**(3), G486–95.

Fukuta H, Kito Y & Suzuki H (2002). Spontaneous electrical activity and associated changes in calcium concentration in guinea-pig gastric smooth muscle. *J Physiol* **540**(1), 249–60.

Ganitkevich V, Shuba M. F & Smirnov S. V (1987). Calcium-dependent inactivation of potential-dependent calcium inward current in an isolated guinea-pig smooth muscle cell. *J Physiol* **392**, 431–49.

Goto K, Matsuoka S & Noma A (2004). Two types of spontaneous depolarizations in the interstitial cells freshly prepared from the murine small intestine. *J Physiol* **559**(2), 411–22.

Hagiwara S, Kusano K & Saito N (1961). Membrane changes of onchidium nerve cell in potassium-rich media. *J Physiol* **155**, 470–89.

Hamilton J. W, Bellahsene B. E, Reichelderfer M, Webster J. G & Bass P (1986). Human electrogastrograms. Comparison of surface and mucosal recordings. *Dig Dis Sci* **31**(1), 33–9.

Hashitani H, Garcia-Londono A. P, Hirst G. D & Edwards F. R (2005). Atypical slow waves generated in gastric corpus provide dominant pacemaker activity in guinea pig stomach. *J Physiol* **569**(2), 459–65.

Hatton W. J, Mason H. S, Carl A, Doherty P, Latten M. J, Kenyon J. L, Sanders K. M & Horowitz B (2001). Functional and molecular expression of a voltage-dependent K+ channel (Kv1.1) in interstitial cells of Cajal. *J Physiol* **533**(Pt 2), 315–27.

Hirst G. D & Edwards F. R (2004). Role of interstitial cells of Cajal in the control of gastric motility. *J Pharmacol Sci* **96**(1), 1–10.

Hirst G. D & Edwards F. R (2001). Generation of slow waves in the antral region of guinea-pig stomach–a stochastic process. *J Physiol* **535**(1), 165–80.

Hirst G. D & Edwards F. R (2006). Electrical events underlying organized myogenic contractions of the guinea pig stomach. *J Physiol* **576**(3), 659–65.

Hirst G. D, Bramich N. J, Teramoto N, Suzuki H & Edwards F. R (2002). Regenerative component of slow waves in the guinea-pig gastric antrum involves a delayed increase in [Ca2+]i and Cl- channels. *J Physiol* **540**(3), 907–19.

Hodgkin A. L & Huxley A. F (1952). A quantitative description of membrane current and its application to conduction and excitation in nerve. *J Physiol* **117**(4), 500–44.

Holm A. N, Rich A, Miller S. M, Strege P, Ou Y, Gibbons S, Sarr M. G, Szurszewski J. H, Rae J. L & Farrugia G (2002). Sodium current in human jejunal circular smooth muscle cells. *Gastroenterology* **122**(1), 178–87.

Huang C. L & Peachey L. D (1992). A reconstruction of charge movement during the action potential in frog skeletal muscle. *Biophys J* **61**(5), 1133–46.

Huang S, Nakayama S, Iino S & Tomita T (1999). Voltage sensitivity of slow wave frequency in isolated circular muscle strips from guinea pig gastric antrum. *Am J Physiol* **276**(2 Pt 1), G518–28.

Huh C. H, Bhutani M. S, Farfan E. B & Bolch W. E (2003). Individual variations in mucosa and total wall thickness in the stomach and rectum assessed via endoscopic ultrasound. *Physiol Meas* **24**(4), N15–22.

Huizinga J. D (2001). Physiology and pathophysiology of the interstitial cell of Cajal: from bench to bedside. II. gastric motility: lessons from mutant mice on slow waves and innervation. *Am J Physiol Gastrointest Liver Physiol* **281**(5), G1129–34.

Huizinga J. D, Zhu Y, Ye J & Molleman A (2002). High-conductance chloride channels generate pacemaker currents in interstitial cells of Cajal. *Gastroenterology* **123**(5), 1627–36.

Hunt L. C & Jongh Curry A. L (2004). Finite element computer modeling of transthoracic atrial defibrillation. *Conf Proc IEEE Eng Med Biol Soc* **6**, 3964–7.

Hurwitz L, Fitzpatrick D. F, Debbas G & Landon E. J (1973). Localization of calcium pump activity in smooth muscle. *Science* **179**(71), 384–6.

Imtiaz M. S, Smith D. W & Helden D. F (2002). A theoretical model of slow wave regulation using voltage-dependent synthesis of inositol 1,4,5-trisphosphate. *Biophys J* **83**(4), 1877–90.

Inoue R & Isenberg G (1990)a. Effect of membrane potential on acetylcholine-induced inward current in guinea-pig ileum. *J Physiol* **424**, 57–71.

Inoue R & Isenberg G (1990)b. Intracellular calcium ions modulate acetylcholine-induced inward current in guinea-pig ileum. *J Physiol* **424**, 73–92.

Isaac L, McArdle S, Miller N. M, Foster R. W & Small R. C (1996). Effects of some K+-channel inhibitors on the electrical behaviour of guinea-pig isolated trachealis and on its responses to spasmogenic drugs. *Br J Pharmacol* **117** (8), 1653–62.

Jafri M. S & Gillo B (1994). A membrane potential model with counterions for cytosolic calcium oscillations. *Cell Calcium* **16**(1), 9–19.

Kadinov B, Itzev D, Gagov H, Christova T, Bolton T. B & Duridanova D (2002). Induction of heme oxygenase in guinea-pig stomach: roles in contraction and in single muscle cell ionic currents. *Acta Physiol Scand* **175** (4), 297–313.

Kaji M, Nomura M, Tamura Y & Ito S (2007). Relationships between insulin resistance, blood glucose levels and gastric motility: an electrogastrography and external ultrasonography study. *J Med Invest* **54**(1-2), 168–76.

Kang T. M, Kim Y. C, Sim J. H, Rhee J. C, Kim S. J, Uhm D. Y, So I & Kim K. W (2001). The properties of carbachol-activated nonselective cation channels at the single channel level in guinea pig gastric myocytes. *Jpn J Pharmacol* **85**(3), 291–8.

Kasicka-Jonderko A, Jonderko K, Krusiec-Swidergol B, Obrok I & Blonska-Fajfrowska B (2006). Comparison of multichannel electrogastrograms obtained with the use of three different electrode types. *J Smooth Muscle Res* **42**(2-3), 89–101.

Kim B. J, Jun J. Y, So I & Kim K. W (2006)a. Involvement of mitochondrial Na+-Ca2+ exchange in intestinal pacemaking activity. *World J Gastroenterol* **12**(5), 796–9.

Kim B. J, So I & Kim K. W (2006)b. The relationship of TRP channels to the pacemaker activity of interstitial cells of Cajal in the gastrointestinal tract. *J Smooth Muscle Res* **42**(1), 1–7.

Kim S. J, Ahn S. C, Kim J. K, Kim Y. C, So I & Kim K. W (1997). Changes in intracellular Ca2+ concentration induced by L-type Ca2+ channel current in guinea pig gastric myocytes. *Am J Physiol* **273**(6 Pt 1), C1947–56.

Kim T. W, Koh S. D, Ordog T, Ward S. M & Sanders K. M (2003). Muscarinic regulation of pacemaker frequency in murine gastric interstitial cells of Cajal. *J Physiol* **546**(Pt 2), 415–25.

Kim Y. C, Koh S. D & Sanders K. M (2002). Voltage-dependent inward currents of interstitial cells of Cajal from murine colon and small intestine. *J Physiol* **541**(Pt 3), 797–810.

Kito Y & Suzuki H (2003). Electrophysiological properties of gastric pacemaker potentials. *J Smooth Muscle Res* **39**(5), 163–73.

Knot H, Brayden J & Nelson M (1995). Calcium channels and potassium channels. In *Biochemistry of smooth muscle contraction*, pp. 203–217. Academic Press, San Diego.

Koch K. L (2001). Electrogastrography: physiological basis and clinical application in diabetic gastropathy. *Diabetes Technol Ther* **3**(1), 51–62.

Koh S. D, Ward S. M, Dick G. M, Epperson A, Bonner H. P, Sanders K. M, Horowitz B & Kenyon J. L (1999). Contribution of delayed rectifier potassium currents to the electrical activity of murine colonic smooth muscle. *J Physiol* **515 (Pt 2)**, 475–87.

Koh S. D, Monaghan K, Ro S, Mason H. S, Kenyon J. L & Sanders K. M (2001). Novel voltage-dependent non-selective cation conductance in murine colonic myocytes. *J Physiol* **533**(Pt 2), 341–55.

Koh S. D, Jun J. Y, Kim T. W & Sanders K. M (2002). A Ca2+-inhibited non-selective cation conductance contributes to pacemaker currents in mouse interstitial cell of Cajal. *J Physiol* **540**(3), 803–14.

Kohno N, Nomura M, Okamoto H, Kaji M & Ito S (2006). The use of electrogastrography and external ultrasonography to evaluate gastric motility in Crohn's disease. *J Med Invest* **53**(3-4), 277–84.

Komuro T (2006). Structure and organization of interstitial cells of Cajal in the gastrointestinal tract. *J Physiol* **576**(3), 653–8.

Komuro T (1999). Comparative morphology of interstitial cells of Cajal: ultrastructural characterization. *Microsc Res Tech* **47**(4), 267–85.

Lammers W. J, Stephen B, Adeghate E, Ponery S & Pozzan O (1998). The slow wave does not propagate across the gastroduodenal junction in the isolated feline preparation. *Neurogastroenterol Motil* **10**(4), 339–49.

Lang R & Rattray-Wood C (1996). A simple mathematical model of the spontaneous electrical activity in a single smooth muscle myocyte. In *Smooth muscle excitation*, pp. 391–402. Academic Press, London.

Langton P, Ward S. M, Carl A, Norell M. A & Sanders K. M (1989)a. Spontaneous electrical activity of interstitial cells of Cajal isolated from canine proximal colon. *Proc Natl Acad Sci U S A* **86**(18), 7280–4.

Langton P. D, Burke E. P & Sanders K. M (1989)b. Participation of Ca currents in colonic electrical activity. *Am J Physiol* **257**(3 Pt 1), C451–60.

Lee H. T, Hennig G. W, Fleming N. W, Keef K. D, Spencer N. J, Ward S. M, Sanders K. M & Smith T. K (2007)a. The mechanism and spread of pacemaker activity through myenteric interstitial cells of Cajal in human small intestine. *Gastroenterology* **132**(5), 1852–65.

Lee H. T, Hennig G. W, Fleming N. W, Keef K. D, Spencer N. J, Ward S. M, Sanders K. M & Smith T. K (2007)b. Septal interstitial cells of Cajal

conduct pacemaker activity to excite muscle bundles in human jejunum. *Gastroenterology* **133**(3), 907–17.

Lin A. S, Buist M. L, Cheng L. K, Smith N. P & Pullan A. J (2006)a. Computational simulations of the human magneto- and electroenterogram. *Ann Biomed Eng* **34**(8), 1322–31.

Lin A. S, Buist M. L, Smith N. P & Pullan A. J (2006)b. Modelling slow wave activity in the small intestine. *J Theor Biol* **242**(2), 356–62.

Lin Z, Forster J, Sarosiek I & McCallum R. W (2003). Treatment of gastroparesis with electrical stimulation. *Dig Dis Sci* **48**(5), 837–48.

Lin Z, Sarosiek I, Forster J & McCallum R. W (2006)c. Symptom responses, long-term outcomes and adverse events beyond 3 years of high-frequency gastric electrical stimulation for gastroparesis. *Neurogastroenterol Motil* **18** (1), 18–27.

Liu J, Qiao X & Chen J. D (2006). Therapeutic potentials of a novel method of dual-pulse gastric electrical stimulation for gastric dysrhythmia and symptoms of nausea and vomiting. *Am J Surg* **191**(2), 255–61.

Locke G. R, Ackerman M. J, Zinsmeister A. R, Thapa P & Farrugia G (2006). Gastrointestinal symptoms in families of patients with an SCN5A-encoded cardiac channelopathy: evidence of an intestinal channelopathy. *Am J Gastroenterol* **101**(6), 1299–304.

Luo C. H & Rudy Y (1994)a. A dynamic model of the cardiac ventricular action potential. I. Simulations of ionic currents and concentration changes. *Circ Res* **74**(6), 1071–96.

Luo C. H & Rudy Y (1994)b. A dynamic model of the cardiac ventricular action potential. II. Afterdepolarizations, triggered activity, and potentiation. *Circ Res* **74**(6), 1097–113.

Magnus G & Keizer J (1997). Minimal model of beta-cell mitochondrial Ca2+ handling. *Am J Physiol* **273**(2 Pt 1), C717–33.

Magnus G & Keizer J (1998)a. Model of beta-cell mitochondrial calcium handling and electrical activity. I. Cytoplasmic variables. *Am J Physiol* **274**(4 Pt 1), C1158–73.

Magnus G & Keizer J (1998)b. Model of beta-cell mitochondrial calcium handling and electrical activity. II. Mitochondrial variables. *Am J Physiol* **274**(4 Pt 1), C1174–84.

Malmivuo J & Plonsey R (1994). Bidomain model of multicellular volume conductor. In *Bioelectromagnetism: principles and applications of bioelectric and biomagnetic fields*, pp. 159–168. Oxford University Press.

Malysz J, Donnelly G & Huizinga J. D (2001). Regulation of slow wave frequency by IP(3)-sensitive calcium release in the murine small intestine. *Am J Physiol Gastrointest Liver Physiol* **280**(3), G439–48.

Marhl M, Haberichter T, Brumen M & Heinrich R (2000). Complex calcium oscillations and the role of mitochondria and cytosolic proteins. *Biosystems* **57**(2), 75–86.

Marieb E. *Human Anatomy and Physiology*. Pearson (2004).

Marvin Schuster Center. URL. http://www.hopkinsbayview.org/motil/ (2008).

McKay C. M, Ye J & Huizinga J. D (2006). Characterization of depolarization-evoked ERG K currents in interstitial cells of Cajal. *Neurogastroenterol Motil* **18**(4), 324–33.

Miftakhov R. N & Abdusheva G. R (1996). Numerical simulation of excitation-contraction coupling in a locus of the small bowel. *Biol Cybern* **74**(5), 455–67.

Miftakhov R. N & Wingate D. L (1996). Electrical activity of the sensory afferent pathway in the enteric nervous system. *Biol Cybern* **75**(6), 471–83.

Miftakhov R. N, Abdusheva G. R & Christensen J (1999)a. Numerical simulation of motility patterns of the small bowel. I. formulation of a mathematical model. *J Theor Biol* **197**(1), 89–112.

Miftakhov R. N, Abdusheva G. R & Christensen J (1999)b. Numerical simulation of motility patterns of the small bowel. II. Comparative pharmacological validation of a mathematical model. *J Theor Biol* **200**(3), 261–90.

Molleman J (1995). Ion Channels involved in gastrointestinal action potential generation. In *Pacemaker activity and intracellular communication*, pp. 223–235. CRC Press.

Monteith G. R, Kable E. P, Chen S & Roufogalis B. D (1996). Plasma membrane calcium pump-mediated calcium efflux and bulk cytosolic free calcium in cultured aortic smooth muscle cells from spontaneously hypertensive and wistar-kyoto normotensives rats. *J Hypertens* **14**(4), 435–42.

Moore E. D, Etter E. F, Philipson K. D, Carrington W. A, Fogarty K. E, Lifshitz L. M & Fay F. S (1993). Coupling of the Na+/Ca2+ exchanger, Na+/K+ pump and sarcoplasmic reticulum in smooth muscle. *Nature* **365** (6447), 657–60.

Muraki K, Imaizumi Y & Watanabe M (1991). Sodium currents in smooth muscle cells freshly isolated from stomach fundus of the rat and ureter of the guinea-pig. *J Physiol* **442**, 351–75.

Nelsen T. S & Becker J. C (1968). Simulation of the electrical and mechanical gradient of the small intestine. *Am J Physiol* **214**(4), 749–57.

Nickerson D, Smith N & Hunter P (2005). New developments in a strongly coupled cardiac electromechanical model. *Europace* **7**(s2), 118–27.

NIDDK. URL. http://digestive.niddk.nih.gov/statistics/statistics.htm (2006).

Noack T, Deitmer P & Lammel E (1992). Characterization of membrane currents in single smooth muscle cells from the guinea-pig gastric antrum. *J Physiol* **451**, 387–417.

Ou Y, Gibbons S. J, Miller S. M, Strege P. R, Rich A, Distad M. A, Ackerman M. J, Rae J. L, Szurszewski J. H & Farrugia G (2002). SCN5A is expressed in human jejunal circular smooth muscle cells. *Neurogastroenterol Motil* **14**(5), 477–86.

Parkman H. P, Hasler W. L, Barnett J. L & Eaker E. Y (2003). Electrogastrography: a document prepared by the gastric section of the American Motility Society Clinical GI Motility Testing Task Force. *Neurogastroenterol Motil* **15**(2), 89–102.

Porras D, Rogers J. M, Smith W. M & Pollard A. E (2000). Distributed computing for membrane-based modeling of action potential propagation. *IEEE Trans Biomed Eng* **47**(8), 1051–7.

Potse M, Dube B, Vinet A & Cardinal R (2006). A comparison of monodomain and bidomain propagation models for the human heart. *Conf Proc IEEE Eng Med Biol Soc* **1**, 3895–8.

Publicover N. G & Sanders K. M (1989). Are relaxation oscillators an appropriate model of gastrointestinal electrical activity? *Am J Physiol* **256**(2 Pt 1), G265–74.

Pullan A, Cheng L, Yassi R & Buist M (2004). Modelling gastrointestinal bioelectric activity. *Prog Biophys Mol Biol* **85**(2-3), 523–50.

Pullan A, Buist M & Cheng LK. *Mathematically modelling the electrical activity of the heart: From cell to body surface and back again.* World Scientific Singapore (2005).

Roberge F. A (1969). Simulation of the phenomenon of concealed conduction. *Comput Biomed Res* **2**(4), 362–72.

Roth B. J & Wikswo J. P (1986). A bidomain model for the extracellular potential and magnetic field of cardiac tissue. *IEEE Trans Biomed Eng* **33** (4), 467–9.

Roux E, Noble P. J, Noble D & Marhl M (2006). Modelling of calcium handling in airway myocytes. *Prog Biophys Mol Biol* **90**(1-3), 64–87.

Sanders K. M (2001). Invited review: mechanisms of calcium handling in smooth muscles. *J Appl Physiol* **91**(3), 1438–49.

Sanders K. M (1996). A case for interstitial cells of Cajal as pacemakers and mediators of neurotransmission in the gastrointestinal tract. *Gastroenterology* **111**(2), 492–515.

Sanders K. M & Publicover N (1995). Electrophysiology of the gastric musculature. In *Handbook of physiology*, pp. 187–216. Academic Press.

Sanders K. M, Koh S. D & Ward S. M (2006)a. Interstitial cells of cajal as pacemakers in the gastrointestinal tract. *Annu Rev Physiol* **68**, 307–43.

Sanders K, Koh S & Ward,S (2006)b. Organization and electrophysiology of interstitial cells of Cajal and smooth muscle cells in the gastrointestinal tract. In *Handbook of Physiology*, pp. 533–576. Academic Press.

Sarna S. K, Daniel E. E & Kingma Y. J (1971). Simulation of slow-wave electrical activity of small intestine. *Am J Physiol* **221**(1), 166–75.

Sarna S. K, Daniel E. E & Kingma Y. J (1972)a. Effects of partial cuts on gastric electrical control activity and its computer model. *Am J Physiol* **223**(2), 332–40.

Sarna S. K, Daniel E. E & Kingma Y. J (1972)b. Premature control potentials in the dog stomach and in the gastric computer model. *Am J Physiol* **222** (6), 1518–23.

Schuster S, Marhl M & Hofer T (2002). Modelling of simple and complex calcium oscillations. From single-cell responses to intercellular signalling. *Eur J Biochem* **269**(5), 1333–55.

Seki K, Zhou D. S & Komuro T (1998). Immunohistochemical study of the c-kit expressing cells and connexin 43 in the guinea-pig digestive tract. *J Auton Nerv Syst* **68**(3), 182–7.

Sims S. M (1992)a. Calcium and potassium currents in canine gastric smooth muscle cells. *Am J Physiol* **262**(5 Pt 1), G859–67.

Sims S. M (1992)b. Cholinergic activation of a non-selective cation current in canine gastric smooth muscle is associated with contraction. *J Physiol* **449**, 377–98.

Skinner F. K, Ward C. A & Bardakjian B. L (1993). Pump and exchanger mechanisms in a model of smooth muscle. *Biophys Chem* **45**(3), 253–72.

Smirnov S. V, Zholos A. V & Shuba M. F (1992). A potential-dependent fast outward current in single smooth muscle cells isolated from the newborn rat ileum. *J Physiol* **454**, 573–89.

Sperelakis N & Daniel E. E (2004). Activation of intestinal smooth muscle cells by interstitial cells of Cajal in simulation studies. *Am J Physiol Gastrointest Liver Physiol* **286**(2), G234–43.

Spitzer V, Ackerman M. J, Scherzinger A. L & Whitlock D (1996). The visible human male: a technical report. *J Am Med Inform Assoc* **3**(2), 118–30.

Splawski I, Timothy K. W, Sharpe L. M, Decher N, Kumar P, Bloise R, Napolitano C, Schwartz P. J, Joseph R. M, Condouris K, Tager-Flusberg H, Priori S. G, Sanguinetti M. C & Keating M. T (2004). Cav1.2 calcium channel dysfunction causes a multisystem disorder including arrhythmia and autism. *Cell* **119**(1), 19–31.

Stratton C. J, Ward S. M, Horiguchi K & Sanders K. M (2007). Immunocytochemical identification of interstitial cells of Cajal in the murine fundus using a live-labelling technique. *Neurogastroenterol Motil* **19**(2), 152–9.

Strege P. R, Ou Y, Sha L, Rich A, Gibbons S. J, Szurszewski J. H, Sarr M. G & Farrugia G (2003). Sodium current in human intestinal interstitial cells of Cajal. *Am J Physiol Gastrointest Liver Physiol* **285**(6), G1111–21.

Strege P. R, Mazzone A, Kraichely R. E, Sha L, Holm A. N, Ou Y, Lim I, Gibbons S. J, Sarr M. G & Farrugia G (2007). Species dependent expression

of intestinal smooth muscle mechanosensitive sodium channels. *Neurogastroenterol Motil* **19**(2), 135–43.

Streutker C. J, Huizinga J. D, Driman D. K & Riddell R. H (2007). Interstitial cells of Cajal in health and disease. Part I: normal ICC structure and function with associated motility disorders. *Histopathology* **50**(2), 176–89.

Suzuki H (2000). Cellular mechanisms of myogenic activity in gastric smooth muscle. *Jpn J Physiol* **50**(3), 289–301.

Szurszeswski JH (1987). Electrical Basis for Gastrointestinal Motility. In *Physiology of the Gastrointestinal Tract*, pp. 383–422. Raven Press.

Szurszewski J. H & Farrugia G (2004). Carbon monoxide is an endogenous hyperpolarizing factor in the gastrointestinal tract. *Neurogastroenterol Motil* **16**(s1), 81–5.

Takaki M (2003). Gut pacemaker cells: the interstitial cells of Cajal (ICC). *J Smooth Muscle Res* **39**(5), 137–61.

ten Tusscher K. H, Noble D, Noble P. J & Panfilov A. V (2004). A model for human ventricular tissue. *Am J Physiol Heart Circ Physiol* **286**(4), H1573–89.

Thornbury K. D, Ward S. M & Sanders K. M (1992). Participation of fast-activating, voltage-dependent k currents in electrical slow waves of colonic circular muscle. *Am J Physiol* **263**(1 Pt 1), C226–36.

Tiwari J. K & Sikdar S. K (1999). Temperature-dependent conformational changes in a voltage-gated potassium channel. *Eur Biophys J* **28**(4), 338–45.

Tokutomi N, Maeda H, Tokutomi Y, Sato D, Sugita M, Nishikawa S, Nishikawa S, Nakao J, Imamura T & Nishi K (1995). Rhythmic Cl- current and physiological roles of the intestinal c-kit-positive cells. *Pflugers Arch* **431**(2), 169–77.

Veldkamp M. W, Viswanathan P. C, Bezzina C, Baartscheer A, Wilde A. A & Balser J. R (2000). Two distinct congenital arrhythmias evoked by a multidysfunctional Na+ channel. *Circ Res* **86**(9), E91–7.

Vittal H, Farrugia G, Gomez G & Pasricha P. J (2007). Mechanisms of disease: the pathological basis of gastroparesis–a review of experimental and clinical studies. *Nat Clin Pract Gastroenterol Hepatol* **4**(6), 336–46.

Vivaudou M. B, Clapp L. H, J. V. J. W & Singer J. J (1988). Regulation of one type of Ca2+ current in smooth muscle cells by diacylglycerol and acetylcholine. *Faseb J* **2**(9), 2497–504.

Vogalis F & Sanders K. M (1990). Cholinergic stimulation activates a non-selective cation current in canine pyloric circular muscle cells. *J Physiol* **429**, 223–36.

Vogalis F, Publicover N. G, Hume J. R & Sanders K. M (1991). Relationship between calcium current and cytosolic calcium in canine gastric smooth muscle cells. *Am J Physiol* **260**(5 Pt 1), C1012–8.

Vogalis F, Publicover N. G & Sanders K. M (1992). Regulation of calcium current by voltage and cytoplasmic calcium in canine gastric smooth muscle. *Am J Physiol* **262**(3 Pt 1), C691–700.

Vogel R & Weingart R (2002). The electrophysiology of gap junctions and gap junction channels and their mathematical modelling. *Biol Cell* **94**(7-8), 501–10.

Wang R & Wu L (1997). The chemical modification of KCa channels by carbon monoxide in vascular smooth muscle cells. *J Biol Chem* **272**(13), 8222–6.

Ward S. M & Sanders K. M (2006). Involvement of intramuscular interstitial cells of Cajal in neuroeffector transmission in the gastrointestinal tract. *J Physiol* **576**(3), 675–82.

Ward S. M, Ordog T, Koh S. D, Baker S. A, Jun J. Y, Amberg G, Monaghan K & Sanders K. M (2000). Pacemaking in interstitial cells of Cajal depends upon calcium handling by endoplasmic reticulum and mitochondria. *J Physiol* **525**(2), 355–61.

Ward S. M, Dixon R. E, Faoite A & Sanders K. M (2004). Voltage-dependent calcium entry underlies propagation of slow waves in canine gastric antrum. *J Physiol* **561**(Pt 3), 793–810.

Weiss D. L, Keller D. U, Seemann G & Dossel O (2007). The influence of fibre orientation, extracted from different segments of the human left ventricle, on the activation and repolarization sequence: a simulation study. *Europace* **9**(s6), 96–104.

White C & McGeown J. G (2000). Regulation of basal intracellular calcium concentration by the sarcoplasmic reticulum in myocytes from the rat gastric antrum. *J Physiol* **529**(2), 395–404.

Wu C & Fry C. H (2001). Na+/Ca2+ exchange and its role in intracellular ca(2+) regulation in guinea pig detrusor smooth muscle. *Am J Physiol Cell Physiol* **280**(5), C1090–6.

Xi Q, Tcheranova D, Parfenova H, Horowitz B, Leffler C. W & Jaggar J. H (2004). Carbon monoxide activates KCa channels in newborn arteriole smooth muscle cells by increasing apparent Ca2+ sensitivity of alpha-subunits. *Am J Physiol Heart Circ Physiol* **286**(2), H610–8.

Xiong Z, Sperelakis N, Noffsinger A & Fenoglio-Preiser C (1995). Ca2+ currents in human colonic smooth muscle cells. *Am J Physiol* **269**(3 Pt 1), G378–85.

Yamamoto Y, Hu S. L & Kao C. Y (1989). Inward current in single smooth muscle cells of the guinea pig taenia coli. *J Gen Physiol* **93**(3), 521–50.

Yoshino M, Someya T, Nishio A & Yabu H (1988). Whole-cell and unitary Ca channel currents in mammalian intestinal smooth muscle cells: evidence for the existence of two types of Ca channels. *Pflugers Arch* **411**(2), 229–31.

Youm J. B, Kim N, Han J, Kim E, Joo H, Leem C. H, Goto G, Noma A & Earm Y. E (2006). A mathematical model of pacemaker activity recorded from mouse small intestine. *Philos Transact A Math Phys Eng Sci* **364** (1842), 1135–54.

Yunker A. M & McEnery M. W (2003). Low-voltage-activated ("T-type") calcium channels in review. *J Bioenerg Biomembr* **35**(6), 533–75.

Zhang H, Xu X, Wang Z, Li C & Ke M (2006). Correlation between gastric myoelectrical activity recorded by multi-channel electrogastrography and gastric emptying in patients with functional dyspepsia. *Scand J Gastroenterol* **41**(7), 797–804.

Zhu Y, Golden C. M, Ye J, Wang X. Y, Akbarali H. I & Huizinga J. D (2003). ERG K+ currents regulate pacemaker activity in ICC. *Am J Physiol Gastrointest Liver Physiol* **285**(6), G1249–58.

Zhu Y, Mucci A & Huizinga J. D (2005). Inwardly rectifying chloride channel activity in intestinal pacemaker cells. *Am J Physiol Gastrointest Liver Physiol* **288**(4), G809–21.